Controlling Devices to Achieve Stability Guarantees on Electric Distribution Grids

Jaimie Swartz

Electrical Engineering and Computer Sciences
University of California, Berkeley

Technical Report No. UCB/EECS-2022-263
http://www2.eecs.berkeley.edu/Pubs/TechRpts/2022/EECS-2022-263.html

December 14, 2022

Controlling Devices to Achieve Stability Guarantees on Electric Distribution Grids

by

Jaimie Swartz

A dissertation submitted in partial satisfaction of the

requirements for the degree of

Doctor of Philosophy

in

Electrical Engineering and Computer Science

in the

Graduate Division

of the

University of California, Berkeley

Committee in charge:

Alexandra von Meier, Co-chair
Professor Seth Sanders, Co-chair
Professor Duncan Callaway
Professor Claire Tomlin

Fall 2022

Controlling Devices to Achieve Stability Guarantees on Electric Distribution Grids

Abstract

Controlling Devices to Achieve Stability Guarantees on Electric Distribution Grids

by

Jaimie Swartz

Doctor of Philosophy in Electrical Engineering and Computer Science

University of California, Berkeley

Alexandra von Meier, Co-chair

Professor Seth Sanders, Co-chair

Due to the massive increase in renewable energy deployment around the world, the distribution level of electric power grids has more active devices than ever before. Many distributed energy resources (DERs) were installed to output the maximum amount of power available without consideration of the grid's status or the presence of other devices. As a result, grid operators can encounter power quality issues, especially voltage volatility, which can stall the adoption of more renewable energy devices. Traditional grid devices that are intended to maintain distribution grid power quality may be insufficient to address today's challenges. While academic literature has proposed many types of approaches to device control, it can favor approaches that are optimization-based at the expense of being impractical for deployment on real distribution grids.

This thesis argues for the analysis of simple, flexible device controls to improve power quality and power delivery. We take a dynamical systems perspective, which provides transparency into the underlying device interactions. This perspective allows us to develop intuition for device interactions and develop safety guarantees that prevent dangerous behavior. For the important problem of computing DER power injections, we take a holistic approach to controller design, where control parameters and DER siting are analyzed to achieve improved voltage stability. Furthermore, this design is achieved without imposing restrictions on the DER communication network. Next, we consider device design under two important modeling scenarios. First we consider the case of abnormal voltage events, in which there is a strict time limit during which DERs must recover the voltage before devices must disconnect. Then we model the interaction between inverter-based DERs and load-tap changer devices, to determine parameter relationships that guarantee against voltage oscillations. We conclude with a discussion of future work and as synthesize important principles for device control in power systems.

To my parents - providers of the sturdiest safety net you can imagine.

Contents

List of Figures

List of Tables

Acknowledgments

Journey before destination is an ongoing theme in Brandon Sanderson's epic fantasy novel series The Stormlight Archive. Here, the *destination* is succinctly captured by a printed degree certificate, a lollipop (courtesy of Berkeley graduate division), and an optional graduation ceremony (which, granted, was a blast). The *journey* captures the experience itself of doing a PhD. From that experience, I remember most the projects (especially the diagrams!) and the people. This section seeks to characterize the people.

My sincerest thanks to my PhD adviser, Sascha von Meier. She is my greatest advocate, always doing everything in her power to help me succeed while providing me the freedom to take risks and explore my interests. During our ENERGISE calls with 20 attendees, she navigated deftly between our agenda items, using her excellent intuition to make connections and build buy-in that propelled the project forward. I was so delighted to be her teaching assistant for power systems 137B, where we got to geek out together on the latest technologies with engaged students whom I know are going to change the world.

Next, I extend my thanks to Professor Elizabeth Ratnam. I think of her fondly as my second adviser. She has taught me to fish so that I may feed myself (with research) for a lifetime. Despite having an 11-hour timezone difference, and having given birth 9 months ago, Liz finds time to discuss high-level narratives all the way down to the details with me. Together, I believe we have elevated my work to achieve the rigor and clarity that will make a true impact on the power systems field.

My dear grad student lab-mates — Keith Moffat, Kyle Brady, Mohini Bariya, Miles Rusch, Gabriel E. Colón Reyes, and Guillaume Goujard — truly enriched my PhD experience. On my very first day at the lab we had a two-hour ENERGISE kickoff meeting, where we discussed ideas, wrote on the whiteboard, and felt that collaborative energy. I'm so thankful that the lab has continued fostering that energy throughout the Covid pandemic. Outside the lab, I was fortunate to find collaborators who would write out the math equations, debate about why the coupling was so significant, and reason about why the polytope is misshapen. Thank you collaborators Daniel Arnold, Federico Celi, Maxime Baudette, Abhishek Bhardwaj, Guna Bharati, Jasper Pakshong, Brittany Wais, and Jiasheng Qin for getting down to the nitty-gritty with me.

I greatly appreciated getting to to discuss my work with professors in optimization and control who excel in not only research, but also in teaching. I attribute learning so many concepts and techniques in my graduate classes to the truly excellent Professors who taught them: Professor Murat Arcak, Francesco Borelli, Andy Packard, Masayoshi Tomizuka, and Duncan Callaway. In particular, thank you very much to Claire Tomlin. It was a pure joy to take her classes in linear systems, nonlinear systems, and hybrid systems, as well as a special honor to help her teach linear systems. I also thank my qualifying exam and dissertation committee - Professor Robert Pilawa, Duncan Callaway, Seth Sanders, Claire Tomlin, and Sascha von Meier for excellent engagement and (welcomed) scrutiny of my work. Additionally, I extend a big thank you to our department administrator, Shirley Solanio, for going above and beyond in advocating for and aiding me in the progression of my PhD.

The transition from undergrad to grad school was quite a challenge to me, but I learned that the 57 ways to *not* screw up grad school lay in the minds of some truly wonderful upperclassmen. Thank you to the following for helping me build the confidence, know-how, and advice to succeed as a grad researcher: Sylvia Herbert, Robert Matthew, David Fridovich-Keil, Laura Hallock, Kristina Monakhova, and Caroline Lemieux. I also appreciate Roel Dobbe, Jose Daniel Lara, Rodrigo Henriquez Auba, Ciaran Roberts, Patricia Hidalgo-Gonzalez, and Isa Ferrall, who helped me connect the math I learned about in class to challenging, meaningful problems in power systems. I also gained a broader familarity of the energy industry through the Berkeley Energy and Resource collaborative. Together we hosted the Energy Summit, a year-long endeavor with an obscene number of moving parts that culminated in three days of jam-packed fun. Thank you to Lucas Spangher, Marie Thompson, Caroline, Danny Broberg, Anna Brockway, and Wojciech Osowiecki for teaching me how to lead with professionalism and compassion while also having a darn good time.

I next want to shout-out to some amazing grad students who have inspired me and introduced me to different perspectives: Laurel Dunn, Eve Fleisig, Kevin Zheng, Nicholas Spooner, and Jackie King. Thank you as well to Utkarsha Agwan, Sara Fridovich-Keil, Kristen Cotner, David McPherson, and Victoria Tuck for keeping me accountable and motivated during the covid pandemic. Finally, I cannot forget the fun-times posse — Cara He, Marie Pelagie Una Elimbi Moudio, and Shafeeq Ibraheem led by Sam Ibraheem. Sam and I have shared so many nights laughing together, analyzing TV shows minute-by-minute, and discussing the fundamental truths of race, dating, and morality. He has helped me understand such nuance and complexity about society at a time when that kind of dialogue is becoming ever more difficult to find. Margaret Chapman has help me build resilience to the deep challenges met in research and life. I would stop by the Canadian Flag room and we would celebrate small wins, then keep each other company while working into the evening. Her words of wisdom continue to echo in my mind reminding me to be kind to myself, to have patience when planting seeds, and to strike that balance between academic rigor and picking your battles. Finally, I formally recognize Sir Alex Devonport, Lord of Coffee, as his trustee loyal page. The DOP center kitchen and Alex's office have a special place in my heart, reminding me of the many fun Fridays spent together.

I grew up in New Jersey, and from the time that I told my parents that I wanted to move 3000 miles away to go to grad school in California, they have actively supported me every step of the way. Every month I get a little box with a heart on it containing toiletries, sauce packets, and dish gloves. Every week I get tech support on the latest computer hardware malfunction and received free on-demand code advice. Aside from the practical things, my parents are always checking to see if I am safe, keeping a balanced life, and am emotionally ok. They have weaved the sturdiest safety net you can imagine. Having such resilient and unconditional support is invaluable in a PhD environment, where experiments often fail, then kind of work, then fail again. So I want to remind them that I love them and that I am so grateful for all that they have done to help me get this PHD. This thesis is dedicated to them.

Chapter 1

Introduction

1.1 Device Control in Distribution Grids

Over the last decade, there has been unprecedented growth in the number of renewable energy resources connected to the electric power grid in locations around the world [3, 4]. These newly connected resources promote the reduction of greenhouse gas emissions by deferring the construction or incentivising the retirement of traditional fossil fuel generators [5]. Many of these resources are connected to the distribution-level part of power grids and arranged in a distributed manner. Distributed energy resources (DERs) can be supply-side resources such as solar photovoltaics (PV), demand-side resources such as flexible loads, or energy storage technologies such as batteries that operate as generators or loads. To accompany the rapid installation of these active devices on distribution grids, sensors with increasing sampling frequency and accuracy have been deployed by grid operators to better monitor the increasingly complex distribution grids. See Fig. 1.1 for a diagram of the United States power grid.

Many existing DER installation programs allow customers to independently control their DERs without visibility of the impact of the devices on power quality across the grid. For example, rooftop solar PV installations are typically operated to output the maximum amount of real power available [6], regardless of the grid's voltages. Allowing distributed generation to output power in an unchecked manner, especially at the end of a feeder, can be dangerous in two ways: power flows may no longer flow from the distribution substation to customers, and voltages may no longer gradually decrease along the length of the circuit. When there is reverse power flow due to solar PV output, further solar PV installations can be halted because substation transformers may not be designed to accommodate reverse power flow [7]. These power flow irregularities are increasingly harder to predict and can result in protection issues, such as desensitization and unintended islanding [8]. To further emphasize the variability of solar PV power, cloud cover events can cause ramps in solar PV generation on the order of 15% per second at a particular location [9]. These ramps in generation have caused electrical equipment such as inverters to trip offline due to the spikes in grid voltages [10].

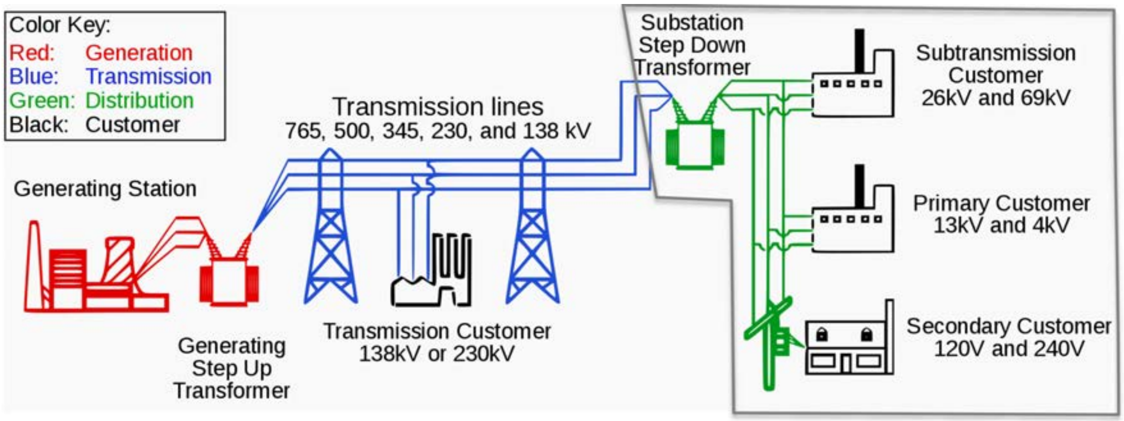

Figure 1.1: Diagram of the electric power grid, with voltage levels that are standard for the United States. The distribution-level of the power grid is outlined in grey.

In extreme circumstances, over-voltage can cause a substation transformer to overload and catch fire. These power quality dangers threaten the safety and efficiency of power delivery and can compromise the integration of higher penetrations of renewable energy.

Currently, grid operators may only use smart meters and legacy voltage regulation devices to monitor and regulate distribution circuit voltages. These devices, namely load-tap changers (LTCs), line voltage regulators, and capacitor banks, were installed to maintain distribution grid voltages within the ANSI standard [11], but they were not designed to accommodate the fluctuations in voltage observed today [12–14]. If the devices do not respond often enough to effectively regulate highly variable voltages, electrical equipment can become damaged or could trip offline. However, operating these expensive devices more often reduces their operating lifespan due to accelerated wear [15, 16]. As a result, legacy voltage regulation devices alone may not be sufficient for effectively mitigating voltages on grids with high renewable energy penetration.

Due to recent advances in power electronic technologies in the last few decades, inverter-based DERs (DERs that interface with the grid through an inverter device) now can provide a fast and flexible response to voltage issues. Distribution grid power lines typically exhibit a high resistance-to-reactance ratio, so real and reactive power flows both have significant impacts on voltage magnitudes [17]. Until recently, industry policies only allowed inverters to set their reactive power output to regulate voltage magnitude (called volt-var control), since real power was highly prioritized for power delivery. Yet with the 2018 revision of the IEEE 1547 inverter standard [6], DERs are now required to have the capability of modulating real power for voltage regulation. In light of these new control capabilities, several works have proposed control approaches to actuate real and reactive power simultaneously to achieve power quality objectives [18–20]. Another new DER control capability is the ability to measure, and then by extension regulate, the voltage phase angle at key locations on distribution grids, allowing grid operators to enforce an optimal state of the grid that ensures all voltages are in the ANSI range. The framework for regulating the full voltage phasor, called Phasor-Based Control (PBC), is detailed later in this thesis.

While new DER control capabilities provide an opportunity for achieving better power quality, a major challenge with control design for power systems is the continued prevalence of parameterized control laws. Specifically, to track a reference signal device actions are computed as a parameterized function of measurements or device states. In a parameterized function, the relationship between the function inputs and outputs is characterized by a set of parameters, which may be set externally. The American electric power grid was built largely in the 20th century when there were very limited measurement and computational capabilities. As a result, simple, tuneable control logic in the form of parameterized functions was deployed and standardized in devices to handle different power problems. For example, commercial power grid software, such as PSLF, encodes dozens of parameters for each layer of synchronous generator control. Furthermore, LTCs are designed to have mechanical taps where the tap parameter determines a shift in distribution grid voltages. Manufacturing grid devices to have parameterized control laws allows standardization of the control logic while keeping the rest of the model — i.e. the parameters — private to the grid operator. The history and benefits of parameterized control laws are major factors in why new devices being deployed continue to have parameterized control laws, such as the droop volt-var function from the IEEE 1547 inverter standard [6]. The challenge is that parameterized control laws constrain the control logic to fit a certain form, which can limit control performance especially at a time where distribution grids are becoming more active and variable in terms of power flows.

Perhaps because there has historically been minimal monitoring and computation capability at points below the distribution grid substation, many academic approaches to device coordination on distribution grids involve solving a large optimization problem on a substation computer. Computing power dispatch for groups of DERs is often cast as an optimal power flow problem [21]. Parameter selection for devices (such as LTCs and inverters) is either selected from rules of thumb [22, Chapter 9.3], or formulated into a mixed-integer optimization problem [23, 24]. Finally, the placement of DERs has been often formulated as a mixed integer unit commitment problem [25, 26]. However, optimization is not always the only or most practical tool for solving these problems. First, grid operators may not have the computational resources or communications necessary to solve an optimization problem, especially if the computation must be done in real-time and for large distribution grid networks which could have thousands of network nodes. Moreover, optimization problems provide optimal solutions, but it is important to know *why* the solution is what it is. Grid operators highly value an understanding of underlying relationships between system components, especially when the problem has many constraints and objective terms. Some literature in optimization for power systems applications suffers from a focus on the complexity of solving an optimization problem, rather than discussing in what way the optimal solution makes sense or reveals important trends.

For this thesis, we advocate for a set of approaches that are different from yet complementary to optimization. Specifically, we address the aforementioned power systems problems through the perspective of dynamical systems analysis. A dynamical system is a model of physical phenomena where differential or difference equations are used to represent the evolution of a system over time. Dynamical system modeling allows control designers to analyze how the underlying physics of device interactions impact the solutions to problems. Essentially, it provides transparency into how a system works. By focusing on dynamic relationships, for example between design parameters and stability, guarantees that eliminate dangerous behavior can be derived and incorporated into industry manufacturing standards. Furthermore, designing real-time control with feedback dynamical systems naturally provides disturbance rejection and reliable set-point tracking. Having highly responsive automatic controls without the need for extensive communication or computation can be highly valuable, considering the rapid increase in the number of interacting devices on distribution grids.

Much of this thesis focuses on key aspects of the DER power set-point control problem because of its particular prominence in industry recently. Inverter-based DERs have the technical capabilities to operate at whatever power set-point that is assigned within their resource limits. This leaves the choice of power set-point, especially for coordinating groups of DERs, as a critical decision. Many utilities are highly interested in building DER management systems, where power set-points for commercial and industrial-scale DERs owned by the utilities are computed to reduce net loads and maintain power quality. Furthermore, virtual power plant companies are rapidly increasing the installation of smaller-scale DERs to build large aggregations of coordinated devices. By strategically computing the DER power set-points, they can direct DER aggregations to provide power quality services and generate economic value in wholesale energy markets. Such power quality services ensure that renewable energy, such as solar PV, continues to be connected without compromising the grid's safety and efficiency.

1.2 Thesis Overview and Summary of Contributions

This thesis explores the modeling, analysis and design of inverter-based DERs and voltage regulation devices on distribution grids. The goal is to effectively coordinate these devices to achieve voltage regulation and power flow objectives, thereby enabling more integration of renewable energy. We adopt a dynamical systems modeling approach, allowing us to guarantee against dangerous scenarios and establish relationships between design choices and control performance. By considering the control design in a holistic manner, we leverage more tools to meet the practical limitations in communication and computation present on many distribution grids.

We begin with Chapter 2, which describes relevant background information. The power flow equations for radial networks and their relationship to power-voltage sensitivities are reviewed. Then, some foundational observations about sensitivities are made that provide the groundwork for the DER siting proofs of Chapter 3. We also review common assumptions about modeling the dynamical systems considered in this thesis and provide an overview of the PBC framework.

In Chapter 3 a detailed analysis on the control of Inverter-based DERs on distribution grids is performed. We develop a model for PBC that accommodates an externally defined communication infrastructure. Then, the model is reduced and is shown to have the same stability properties as the original model. The Gershgorin Disc theorem is then employed to formulate necessary but not sufficient conditions for system stability. The conditions are then used to prove relationships between the arrangement of DERs and system stability. Finally, we propose and validate two methods of selecting control parameters: an analytic method using a conservative stability region, and a heuristic algorithm for sampling candidate controller parameters.

While in Chapter 3 we consider normal grid operation where external disturbances are assumed negligible, in Chapter 4 we focus on the abnormal operation case, where DERs are tasked with recovering from a large-signal voltage disturbance within a standardized time limit. To model disturbances, a polytope is defined whose bounds are given by fitting measurements from a real distribution phasor measurement unit data set. Then, a reachability analysis is performed that determines the set of abnormal voltage disturbances that the DER control is guaranteed to can recover from.

Chapter 3 and 4 considers systems of only DER devices acting on distribution grids, so in Chapter 5 we focus on the interaction of DER devices with load-tap changer devices. We model this interaction in a novel way as a switched affine hybrid system. When the inverters are regulating as intended, we show that all responses to voltage deviations eventually settle to the safe voltage deadband. Then a scenario in which a cyber-attack causes the inverter response to be negated is considered. In that case, we determine conditions on device parameters that guarantee against dangerous, undamped voltage oscillations.

We conclude with Chapter 6, where future research directions and important principles synthesized from this work are described.

1.3 Notation

Mathematical notation adopted throughout this thesis is provided below.

1. The symbol $\forall$ denotes *for all.* The symbol $\in$ denotes *is an element of.*

2. Let $\mathbb{R}^n$ be the n-dimensional vector of real numbers, $\mathbb{C}^n$ be the n-dimensional vector of complex numbers, and $\mathbb{R}^{n\times n}$ the matrix of real numbers.

3. Bold-faced letters are used for vectors and matrices, with the exception that $\mathbf{j} = \sqrt{-1}$ indicates the imaginary part of complex numbers.

4. For a vector $\boldsymbol{x} \in \mathbb{R}^n$, let $\boldsymbol{x}[k]$ be its value at time index $k \in \mathbb{R}$, and $\boldsymbol{x}_i[k]$ be the value of the i-th element of $\boldsymbol{x}$ at time index k.

5. For a matrix $\boldsymbol{A} \in \mathbb{R}^{p \times n}$, $\boldsymbol{A}_{ij}$ refers to the (i, j)th entry. Further, the transpose of the matrix is denoted by $\boldsymbol{A}^\top$, and its pseudoinverse is denoted by $\boldsymbol{A}^\dagger$.

6. Let $\boldsymbol{I}_n$ and $\mathbf{0}_{m \times n}$ stand for the identity n-by-n matrix and zero m-by-n matrix, respectively. The subscript on $\boldsymbol{I}_n$ and $\mathbf{0}_{m \times n}$ are omitted when their dimensions can be inferred from context.

7. The symbol $\subseteq$ denotes *is a subset of*. The symbols $\cup$ and $\cap$ denote the set union and set intersection, respectively.

8. For two sets S and Q, we define $S \setminus Q$ as the subset of S not in set Q.

9. The operator $|.|$ applied to a complex scalar denotes the magnitude operator, and when applied to a set denotes the cardinality of the set.

Chapter 2

Background

This chapter outlines background that will be used in this thesis. It acts as a primer for those less familiar with power systems and certain topics in distribution grid management. This chapter can be skipped without loss of continuity. Later chapters refer to this chapter for more details on certain ideas.

2.1 Power Flow on Radial Networks

2.1.1 Properties of Distribution Grids

Electric power distribution grids differ from transmission grids in two major ways: they are operated with radial topology, and their three-phase loads are often unbalanced.

While distribution grids are often constructed with a meshed topology, they are typically operated in a radial topology. A major reason for operating them radially is so that protection systems can be designed in a hierarchical manner, where the immediate upstream protection device responds to a fault first. Moreover, protection devices can be sized according to the worst-case current only their own network branch. In this thesis, the radial structure of distribution grids will be leveraged for coordination of legacy voltage regulation equipment and inverter-based DERs.

Academic control literature sometimes models distribution grids for simplicity, but the majority of real distribution grids are three-phase and unbalanced. A three-phase unbalanced grid is one in which the load values are unequal across the phases. The imbalance could be due to power lines branching off into one or two phases, or the loads being uneven across the three phases. The unbalanced loads can cause the voltages and currents to differ significantly on each phase. Therefore, designing device controls using single-phase representations alone may not capture the effectiveness of control on each separate phase, nor capture the interactions between phases due to magnetic induction. In this thesis, we use single-phase models to convey our control approach, but we extend our modeling to three-phase unbalanced feeders for use in our simulations.

2.1.2 Graph Network Notation

We begin by considering a single-phase radial distribution network. Because the substation of a distribution grid interfaces with the transmission grid, the substation has a large source impedance, resulting in it being effectively a voltage source modeled with constant voltage magnitude and phase angle. The remaining n nodes are modeled as loads with a constant real and reactive power injection at each time step. If power is generated at a node, the generation is subtracted from the power consumption to yield the net load.

A radial distribution network is typically modeled as a tree graph. It consists of a set of nodes $\mathcal{N}_0 = \{0, 1, ..., n\}$ where node 0 is the root of the tree graph. Node 0 represents the distribution grid substation, and The set of graph edges $\mathcal{L}$ is denoted by $\mathcal{L} \subset \mathcal{N}_0 \times \mathcal{N}_0$, where edge $(i, j) \in \mathcal{L}$ represents a line segment from node i to node j. The distribution network can then be represented by the graph $\mathcal{G} = (\mathcal{N}_0, \mathcal{L})$. Each node has a unique path to node 0 because of the tree topology of the network. For each node $i \in \mathcal{N}_0$, denote by $\mathcal{L}_i \subset \mathcal{L}$ the set of lines on the unique path from node 0 to node i. A node j is *upstream* from node i if $\mathcal{L}_j \subset \mathcal{L}_i$. Conversely, a node j is *downstream* from node i if $\mathcal{L}_j \supset \mathcal{L}_i$. We often refer to the set of nodes downstream of node 0, denoted by $\mathcal{N} = \mathcal{N}_0 \setminus \{0\}$.

2.1.3 Power Flow Linearization

For each node $i \in \mathcal{N}$, the voltage magnitude, voltage phase angle, net real power generation and net reactive power generation are denoted by V_i, δ_i, p_i, and q_i, respectively. The voltage phase angle δ_i is defined with respect to a reference phase angle, typically chosen to be at the substation node. The sign of p_i and q_i is consistent with the positive generation convention. Line segments can represent either a low-voltage or a medium-voltage network. For each line segment $(i, j) \in \mathcal{L}$, the impedance of the line z_{ij} is represented by the line resistance and reactance in complex form $z_{ij} = r_{ij} + \mathbf{j}x_{ij} \in \mathbb{C}$. Additionally, the real (reactive) power flow of the line segment from i to j is P_{ij} (Q_{ij}).

We first consider the linearized branch flow model (LinDistFlow equations) developed in [27] for radial distribution networks. The LinDistFlow equations linearize around a flat voltage profile at 1 per unit and approximate the line current as zero. As such, the authors assume negligible power losses in line segments, yet are able to model distribution-level power networks with satisfactory accuracy as reported in [1, 12, 28]. A single-phase representation of the LinDistFlow equations is expressed by

$$P_{ij} = \sum_{k:(j,k)\in\mathcal{L}} P_{jk} - p_j, \quad \forall j \in \mathcal{N}, \tag{2.1a}$$

$$Q_{ij} = \sum_{k:(j,k)\in\mathcal{L}} Q_{jk} - q_j, \quad \forall j \in \mathcal{N}, \tag{2.1b}$$

$$(V_i)^2 = (V_j)^2 + 2(x_{ij}Q_{ij} + r_{ij}P_{ij}) \quad \forall (i,j) \in \mathcal{L} \tag{2.1c}$$

Next, we consider an extension of the LinDistFlow equations that captures the voltage phase angle difference between two nodes [17,29,30]. The relationship between nodal voltage phase angles δ_i, δ_j and power flow on a single-phase radial network is described by

$$\sin(\delta_i - \delta_j) = \frac{x_{ij}P_{ij} - r_{ij}Q_{ij}}{V_iV_j} \qquad \forall(i,j) \in \mathcal{L} \tag{2.2}$$

To linearize the equation, we make the small-angle approximation $\sin\delta \approx \delta$ and assume $V_i \approx V_j \approx 1p.u.$, retaining the dependence of P_{ij} and Q_{ij} on $(\delta_i - \delta_j)$.

$$\delta_i - \delta_j \approx \frac{x_{ij}P_{ij} - r_{ij}Q_{ij}}{V_iV_j}, \tag{2.3}$$

Note that δ in (2.2) and (2.3) can be measured by a distribution-level PMU by comparing the voltage waveform at node i, $v_i(t) = V_i^{max}\cos(\omega t + \delta_i)$, to that of a reference node $v_{ref}(t) = V^{max}\cos(\omega t)$ which is typically chosen as the distribution substation. The angular frequency ω is the assumed to be constant and equal to $2\pi 50$ or $2\pi 60$ radians per second.

Assumption 1. *(linearization holds) A given system operates near the voltage linearization point of* $1p.u.$. *Specifically, the negligible power line loss assumption and small-angle approximations made to produce the linearized power flow equations* (2.1) *and* (2.3) *hold.*

2.1.4 Sensitivities

to consider the power flow equations in a grid-wise context, we define some vector notation. We define the squared voltage magnitude as $v_i := (V_i)^2$. Then,

$$\boldsymbol{v} = [v_1, v_2, ..., v_n]^\top, \tag{2.4a}$$
$$\boldsymbol{\delta} = [\delta_1, \delta_2, ..., \delta_n]^\top, \tag{2.4b}$$
$$\boldsymbol{p} = [p_1, p_2, ..., p_n]^\top, \tag{2.4c}$$
$$\boldsymbol{q} = [q_1, q_2, ..., q_n]^\top, \tag{2.4d}$$
$$\boldsymbol{v}_0 = [v_0, v_0, ..., v_0]^\top, \tag{2.4e}$$
$$\boldsymbol{\delta}_0 = [\delta_0, \delta_0, ..., \delta_0]^\top. \tag{2.4f}$$

For a grid network with only PQ nodes and one slack node, the power flow Jacobian is defined in [31, Chapter 6.4.3] as

$$\begin{bmatrix}\Delta\mathbf{q}\\ \Delta\mathbf{p}\end{bmatrix} = \boldsymbol{J}\begin{bmatrix}\Delta\mathbf{v}\\ \Delta\boldsymbol{\delta}\end{bmatrix}, \quad \boldsymbol{J} = \begin{bmatrix}\frac{\partial\mathbf{q}}{\partial\mathbf{v}} & \frac{\partial\mathbf{q}}{\partial\delta}\\ \frac{\partial\mathbf{p}}{\partial\mathbf{v}} & \frac{\partial\mathbf{p}}{\partial\boldsymbol{\delta}}\end{bmatrix} \tag{2.5}$$

where $\Delta\boldsymbol{p}$ and $\Delta\boldsymbol{q}$ are vectors of real and reactive power injections at all PQ nodes, respectively. We consider a power injection any change in real or reactive power, whether it be an increase in generation or increase in consumption. The Jacobian represents the small-signal mapping of voltage phasors to real and reactive power flows near the linearization point. In transmission systems, where inductive reactance is generally much greater than resistance, reactive power varies mainly with the voltage magnitude, while real power varies mainly with voltage phase angle. That is, a decoupling assumption of $\frac{\partial \mathbf{q}}{\partial \boldsymbol{\delta}} \approx 0$ and $\frac{\partial \mathbf{p}}{\partial \mathbf{v}} \approx 0$ is often adopted. However, distribution feeders tend to have significant resistive components, and consequently real and reactive power is coupled with both voltage magnitude and phase angle. Moreover, for designing controllers that inject power to regulate voltage on distribution grids, works such as [32] consider all four blocks of the inverse mapping matrix H, which is often referred to as a sensitivity matrix.

$$\begin{bmatrix} \Delta \mathbf{v} \\ \Delta \boldsymbol{\delta} \end{bmatrix} = H \begin{bmatrix} \Delta \mathbf{q} \\ \Delta \mathbf{p} \end{bmatrix}, \quad H = \begin{bmatrix} \frac{\partial \mathbf{v}}{\partial \mathbf{q}} & \frac{\partial \mathbf{v}}{\partial \mathbf{p}} \\ \frac{\partial \boldsymbol{\delta}}{\partial \mathbf{q}} & \frac{\partial \boldsymbol{\delta}}{\partial \mathbf{p}} \end{bmatrix} \tag{2.6}$$

To determine $\boldsymbol{H}$, one could use grid impedance information. However, because distribution grid impedance models are often incomplete or inaccurate, some works that explore model-less methods for computing $\boldsymbol{H}$ through measurements of different types and configurations of sensors [33, 34]. In what follows, we show a measurement-based method based on power injection step responses that was validated in simulation [35] and could be implemented on real power grids to estimate impedances. Further, it demonstrates that under Assumption 1, power-voltage sensitivity is exactly given by impedances.

For a two-bus system, a nodal power injection at the PQ bus $p + \mathbf{j}q$ is equal to the line power flow. We consider these equations at an initial time k and the next steady state time $k+1$, with a power injection that occurs between these times. We assume the injection is small enough for the linearization Assumption 1 to hold. Then, with the slack bus having $v_j[k+1] = v_j[k] = 1$, equations (2.1) and (2.3) become

$$v_i[k] - v_j[k] = 2rp[k] + 2xq[k] \tag{2.7}$$

$$\delta_i[k] - \delta_j[k] = xp[k] - rq[k] \tag{2.8}$$

$$v_i[k+1] - v_j[k+1] = 2rp[k+1] + 2xq[k+1] \tag{2.9}$$

$$\delta_i[k+1] - \delta_j[k+1] = xp[k+1] - rq[k+1] \tag{2.10}$$

Subtracting equation (2.7) from (2.9) and rearranging gives

$$(v_i[k+1] - v_i[k]) - (v_j[k+1] - v_j[k]) = 2r(p[k+1] - p[k]) + 2x(q[k+1] - q[k])$$

$$\frac{v_i[k+1] - v_i[k]}{q[k+1] - q[k]} - \frac{v_j[k+1] - v_j[k]}{q[k+1] - q[k]} = \frac{2r(p[k+1] - p[k])}{q[k+1] - q[k]} + 2x$$

If a small step change in reactive power is injected at node 2 between k and $k+1$ and there is no change in real power ($p[k+1] - p[k] = 0$), we have

$$\left.\frac{\partial v}{\partial q}\right|_{\text{lzn point}} \approx \frac{v_i[k+1] - v_i[k]}{q[k+1] - q[k]} = 2x \tag{2.11}$$

If instead a step change in only real power is applied, we have

$$\frac{\partial v}{\partial p}\bigg|_{\text{lzn point}} \approx \frac{v_i[k+1]-v_i[k]}{p[k+1]-p[k]} = 2r \tag{2.12}$$

Subtracting equation (2.8) from (2.10) and rearranging gives

$$(\delta_i[k+1]-\delta_i[k]) - (\delta_j[k+1]-\delta_j[k]) = x(p[k+1]-p[k]) - r(q[k+1]-q[k])$$

$$\frac{(\delta_i[k+1]-\delta_i[k])}{p[k+1]-p[k]} - \frac{(\delta_j[k+1])^2-(\delta_j[k])^2}{p[k+1]-p[k]} = -\frac{r(q[k+1]-q[k])}{p[k+1]-p[k]} + x$$

If a step change in reactive power is injected at node 2 between k and $k+1$ we have

$$\frac{\partial \delta}{\partial p}\bigg|_{\text{lzn point}} \approx \frac{\delta_j[k+1]-\delta_j[k]}{p[k+1]-p[k]} = x \tag{2.13}$$

If instead a step change in only reactive power is applied, we have

$$\frac{\partial \delta}{\partial p}\bigg|_{\text{lzn point}} \approx \frac{\delta_j[k+1]-\delta_j[k]}{q[k+1]-q[k]} = r \tag{2.14}$$

When a network has more than two nodes, by choosing V_0 as the slack bus, the impedances obtained from the relationships four relationships eqs. (2.11) to (2.14) is the effective impedance between the node of interest and the slack bus. Using these relationships, we can create use measurements from step changes in power that are near the linearization point to approximate impedance values. This method can help improve distribution models and provides model information for inverter control design.

2.1.5 Impedance Matrices for Radial Networks

In this section we familiarize the reader with applying the graph network topology to implications about power voltage sensitivities. The ideas are synthesized from discussions with Rayan El Helou (author of [1]).

Using the vector notation (2.4), the voltage magnitude branch flow equation (2.1) and phase angle equation (2.3) are arranged into the following form:

$$\boldsymbol{v} = \boldsymbol{X}^0\boldsymbol{q} + \boldsymbol{R}^0\boldsymbol{p} + \boldsymbol{v}_0 \tag{2.15a}$$

$$\boldsymbol{\delta} = -\frac{1}{2}\boldsymbol{R}^0\boldsymbol{q} + \frac{1}{2}\boldsymbol{X}^0\boldsymbol{p} + \boldsymbol{\delta}_0. \tag{2.15b}$$

The (i,j)th element of impedance matrices $\boldsymbol{R}^0 \in \mathbb{R}^{n\times n}$ and $\boldsymbol{X}^0 \in \mathbb{R}^{n\times n}$ are constructed by

$$\boldsymbol{R}^0_{ij} = 2\sum_{(w,t)\in\mathcal{L}_i\cap\mathcal{L}_j} r_{wt} \tag{2.16a}$$

$$\boldsymbol{X}^0_{ij} = 2\sum_{(w,t)\in\mathcal{L}_i\cap\mathcal{L}_j} x_{wt}, \tag{2.16b}$$

where the set of nodes that are upstream of both i and j is $\mathcal{L}_i \cap \mathcal{L}_j$. The construction (2.16) is consistent with [1,12,13,16,18]. To extend this modeling to three-phase unbalanced networks, we replace each element of $\boldsymbol{R}^0$ and $\boldsymbol{X}^0$ by a 3×3 matrix that represents impedances across phase A, B, and C, and all system states and inputs increase in dimension by threefold. With this extension, the off-diagonal elements of $\boldsymbol{R}^0$ and $\boldsymbol{X}^0$ capture cross-phase interactions (see [29] for details).

Assumption 2. *Grid network impedances $\boldsymbol{X}^0$ and $\boldsymbol{R}^0$ are known.*

See section 2.1.4 for a discussion on estimating X and R in real distribution grids.

The (i, j)th *power-voltage sensitivity* is the static mapping of a change in power at node i to the change in voltage at node j on a circuit. Under the assumptions of linearized power flow, (2.15) indicates that the power-voltage sensitivities are the impedance matrices $\boldsymbol{R}^0$ and $\boldsymbol{X}^0$ [12,19,32,36]. We then define the complex impedance matrix $\boldsymbol{Z} \coloneqq \boldsymbol{R}^0 + j\boldsymbol{X}^0$. As such, we refer to the *common-node impedance* as $|\boldsymbol{Z}_{ij}| = \sqrt{(\boldsymbol{X}^0_{ij})^2 + (\boldsymbol{R}^0_{ij})^2}$. It is a measure of electrical distance between any pair of nodes (i, j) on a radial network [37].

Assumption 3. *There is some nonzero impedance between the root node of the tree network and the first node that has branches.*

This assumption is reasonable for most radial grids because the tree graph root is considered the distribution grid substation (see section 2.1.2) and the substation typically has a transformer and a conductor extending from the substation before the circuit branches out.

Assumption 4. *Given a radial distribution circuit, all line resistances and reactances are positive.*

This assumption is reasonable for most grids because resistance is always positive and the inductive component of line impedances usually dominates the capacitance. By Assumption 4, $\boldsymbol{X}^0$ and $\boldsymbol{R}^0$ are positive definite, which was proven in [28] and has been used in volt-var literature to prove convergence of voltage control systems [12,28,38]. Additionally, applying this assumption to equation (2.15a) confirms the intuition that an increase in nodal real or reactive power increases voltage magnitude.

We now make some conceptual observations about power-voltage sensitivities using the diagram of a toy network in Fig 2.1:

1. A single power injection at any node changes the voltage magnitude by some amount at every node of the network. This can be seen with the power flow equation (2.15a) and from $\boldsymbol{Z}_{ij} > 0 \; \forall \; i \in \mathcal{N}$ and $j \in \mathcal{N}$ due to Assumption 3.

2. The change in voltage magnitude by single power injection is determined by only common-node impedance between the power injection and voltage measurement locations. For intuition on why, consider a power injection made at node i in Fig. 2.1.

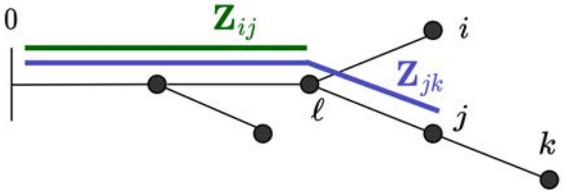

Figure 2.1: The impedance matrix $\boldsymbol{Z}$ is comprised of the common-node impedances between pairs of network nodes. The distribution grid includes two example common-node impedance paths $\boldsymbol{Z}_{ij}$ and $\boldsymbol{Z}_{jk}$ marked in green and purple, respectively.

The only current that changes in the network is the current from node i to the substation, because the power injection is matched by an opposite-direction power injection at the substation, while loads on the other path $\mathcal{L}_k$ continues to demand the same current. Therefore, the voltage drop across the common-node path $\mathcal{L}_\ell$ changes, while the voltage drop across paths in other branches does not.

3. The power injection at node i in Fig. 2.1 causes all voltages on the other branch, namely v_ℓ, v_j, v_k, change by the same amount. Therefore, it can be difficult to regulate v_j, v_k independently using only power injections along path $\mathcal{L}_i$.

4. Item (2) implies that a power injection occurring deep in a circuit will change the distribution level voltage more than if it occurs in a shallow location. This implies that DERs designed to regulate voltages can be especially effective toward the ends of circuits, but likewise explains why non-voltage regulating DERs, such as solar PV in [39]), cause more severe voltage problems at the ends of circuits.

These conceptual points provide a primer to the intuition behind the location-stability theorems in Chapter 3.3.2. A fun way to summarize these concepts is with Rayan Helou's hiking analogy applied to the network diagram in Fig 2.1: suppose you live at node i, your friend lives at node j, and you want to hike together up to node 0. You meet at node ℓ then hike together to node 0, then back to node ℓ, then you each go back home. The forward and return trip helps explain the '2' in the construction of the $\boldsymbol{R}^0$ and $\boldsymbol{X}^0$ matrices (2.16). Finally, the total distance you spend together, measured by the common-node impedance, determines the voltage drop at i due to a power injection at node j (or vice versa).

2.2 Grid Simulations and Assumptions

The electric power grid is a highly nonlinear, time-varying system with many categories of active devices and grid phenomena. A central problem in designing and operating the power grid is determining the appropriate level of modeling detail for both grid devices and the grid components, since what is appropriate depends on the problem of interest. This challenge is exacerbated by the introduction of a new suite of power electronic devices to the grid. In this section, we draw distinctions between two categories of power systems control, where we describe the dynamic phenomena, assumptions, and simulation setup for each.

2.2.1 Fast Dynamics

The first category is fast dynamics, where we consider grid phenomena and control loops with a time constant of less than one second. The main grid equipment categories — power lines, loads, synchronous generators, power converters circuit breakers — can be modeled with differential equations that evolve at the sub-second level. In the last decade, there has been great focus on modeling the fast dynamics of inverters (DC to AC converters), including modeling of the power electronic circuitry and the internal voltage and current control loops. When modeling groups of inverters operating on a power grid, the states tend to be the current and voltage waveforms in the time domain, and loads are often modeled as having constant resistance and/or being an induction motor. If a single dynamic device is of interest, such as a synchronous machine or converter, one may model a dynamical system comprised of differential or difference equations, sometimes using electromagnetic transient software. In contrast, incorporating the power grid network into the model may require adding the algebraic power flow equations (see linearized version in (2.1)), which results in a Differential-Algebraic Equation (DAE) system. DAEs include both differential equations $\dot{x} = f(x, y)$ and algebraic equations $0 = g(x, y)$. MATLAB's ODE45 function can be used to solve DAE equations. When simulating DAE models, the simulation is propagated forward by numerical integration between short timesteps, typically between 1 millisecond and 1 second for power systems applications. For example, when a synchronous generator is connected with a line to an infinite bus, one could set up a DAE simulation that integrates the generator's power-frequency dynamics with the power flow along the line. DAE simulations have also become popular for assessing small-signal stability and dynamic interactions in low-inertia grids, as done in [40–43].

2.2.2 Slow Dynamics

The second category is slow dynamics, where we consider grid phenomena and control loops with a time constant of greater than one second. To isolate and analyze slow dynamics, the fast dynamics are assumed to be stable.

Assumption 5. *we assume the sub-second dynamics from inverters, lines, and loads are stable, and that those dynamics reach steady state between time steps.*

Under this assumption, the voltage and current waveforms are smooth and measurable with constant grid frequency. As a result, the system states are often voltage magnitude, current magnitude, energy storage levels, or power levels. Some low-inertia grid literature is investigating the validity of this assumption for different levels of inverter penetration on the grid [3]. In the meantime, authors in load tap changing voltage regulation, volt-var control [1,12,38,44], DER coordination, and economic dispatch academic spaces often adopt this assumption.

One common way to simulate models with slow dynamics is with Quasi-static-time series (QSTS) simulations. The key distinction between QSTS and dynamic (or DAE) simulations is that QSTS simulations do not involve solving differential equations. Rather, each time step of QSTS simulations, which are typically between one second and one hour, represents the steady state of the system. In the power systems field, the steady state may be computed by solving the algebraic power flow equations at each time step, and the inputs to each power flow computation are determined by discrete events. We note that models may incorporate memory or not. Without memory, each time step of the simulation can be computed independently without any knowledge of variables in other time steps. These simulations may be sufficient if the grid operation is predictable and has low variability in voltages and power flows. More recently, however, the discrete events contain memory to enable faster reaction to grid issues. The simplest model for discrete events with memory is a first-order autonomous difference equation

$$\boldsymbol{x}[k+1] = a\boldsymbol{x}k].$$

Because this equation has the same form as a recursive optimization iteration, some works refer to the system as having iterative updates rather than evolving as a discrete-time dynamical system. The memory is important because the choice of a determines whether the system state converges or diverges. When authors wish to analyze this convergence behavior, they may characterize the system as quasi steady-state dynamical system [12,13,38,45,46], so that traditional dynamical system analysis techniques, such as eigenvalue analysis, can be applied. The work in this thesis characterizes models in this way.

Common software used for slow dynamics on distribution grids include GridLab-D, OpenDSS, and MATLAB/Simulink. GridLab-D is typically used for QSTS simulations, but also includes an option to run part of a simulation with a faster timestep in *deltamode*. Simulink's Simscape component blocks can be used to set up QSTS or dynamic simulations. Finally, Opal-RT's power flow solver ePHASORSIM has a Simulink interface for running QSTS simulations as well as quasi-steady state dynamical systems.

2.3 Phasor-Based Control

In this section we provide context, motivation, and some hierarchical details about Phasor-Based Control (PBC). The other chapters of the dissertation employ PBC but do not return to this higher-level discussion.

2.3.1 Phasor-measurement Units (PMUs)

Sophisticated approaches for controlling DERs require advanced sensing capabilities. Phasor-measurement units (PMUs) are devices that have been successfully used to measure the voltage magnitude and phase angle of the electricity grid using GPS synchronization. As a result, the number of installments of PMUs on transmission grids has grown dramatically in recent years [47]. However, there is a lack of distribution level sensors that can measure voltages at a rate faster than the typical fifteen minutes of a smart meter. One promising technology is Distribution PMUs (D-PMUs), which provide ultra-precise, synchronized measurements of voltage magnitudes and phase angles on distribution grids [48]. These instruments sample at 120Hz and can reliably discern angle differences as small as ten millidegrees, or about half a microsecond [49].

Measurement of the full voltage phasor using D-PMUs along with the voltage phasor power flow equation (2.2) motivates PBC, which is a framework where voltage phasors are regulated to achieve an optimal grid state while providing an immediate corrective response to disturbances.

2.3.2 Overview

The PBC framework is designed to facilitate the integration of heterogeneous and intermittent distributed energy resources (DER) on the electric grid. PBC presents a unified approach that is agnostic to optimization criteria and the particular characteristics of participating resources. Further, it can be deployed across transmission and distribution level grids. At its core, PBC frames the control of DERs around tracking voltage phasor targets, instead of tracking targets for real and/or reactive power set-points. By designing controllers around the physical grid quantity of voltage, there are opportunities to improve the power quality and stability of the grid.

Phasor-based control employs a multi-layer control hierarchy that decouples high-level long-term optimal objectives from short-term power quality objectives [17]. A centralized controller (called the S-PBC layer) solves an optimal power flow (OPF) problem periodically to determine optimal voltage phasor targets. The phasor targets computed by the S-PBC are them broadcast across a network to one or more feedback controllers (called the L-PBC layer). Each feedback controller regularly computes a set of real and reactive power setpoint commands for one or more controllable resources to impact the grid voltage phasor. When the controller drives the voltage phasors to their targets, the grid operates at an optimal state. If before convergence a voltage disturbance on order of $1Hz$ or slower occurs, the feedback controllers compute an immediate power injection response that rejects the disturbance while the S-PBC computes updated optimal phasor targets.

The PBC system is agnostic to the optimization formulation, the characteristics of participating resources, and the structure of the grid. PBC frames the contributions of generators and loads in terms of their physical effect on the network, by explicitly referring to the electrical state variables — voltage magnitude and voltage phase angle — that constitute the voltage *phasor* at any given network node, not only nodes with a DER connected. The use of the phasor as a network state variable enables an immediate corrective response to disturbances without communication between resources and without compromising privacy.

2.3.3 Important Features

The S-PBC requires a grid network model, desired DER locations, DER capacities, and a load and generation forecast. OPF objectives can be specified by a utility or other external operator, such as a DER aggregator. Some objectives can be very effectively expressed in terms of voltage phasor targets at specific nodes, including reducing voltage volatility, balancing three phases, preventing reverse power flow on distribution circuits, and matching voltage phasors across an open switch to facilitate microgrid islanding. The constraints can align with traditional OPF formulations, including the enforcing of voltage limits at all network nodes and enforcing of resource constraints (such as capacity and solar power availability) at DER nodes. When the OPF problem is feasible, there exists a set of nodal power injections with corresponding voltage phasors that satisfies all OPF constraints, including the DER capacity limits. Therefore, S-PBC may not converge if there are not enough DERs, there is not enough capacity per DER, or the DERs are placed in locations that prohibit them from satisfying the OPF constraints. However, if the OPF is feasible, the forecast leverages knowledge of the load and generation at non-measured nodes, ensuring that tracking a subset of network nodes achieves objectives across all nodes.

The output of S-PBC is phasor targets for all network nodes, but only a subset needs to be tracked by the specified set of DERs. Even if the grid state associated with the OPF solution is feasible, designing a set of feedback controllers to drive the grid's state to that state is challenging. Feedback controllers may have limited access to the full set of grid measurements, and limited or no communication between DERs. Further, the number and location of nodes being tracked may affect the ability of the controllers to achieve the optimal grid state. Finally, when a subset of the network nodes are being tracked (commonly the case), there exist multiple combinations of controller power injections that achieve the same voltage phasor targets. Therefore, the design of the L-PBC layer is a challenging task that includes questions about appropriate controller gains, DER locations, sensor locations, and requirements for controller convergence.

Chapter 3

Stability of Groups of Inverter-Based DERs

This chapter is based on the papers [50–52], written in collaboration with Elizabeth Ratnam, Abhishek Bhardwaj, Brittany Wais, and Alexandra von Meier.

In this chapter, we explore power set-point control of Inverter-based DERs. We develop a dynamical system model for DERs operating under PBC using linearized power flow equations and discrete time feedback controllers. To incorporate limitation in available communication infrastructure on many distribution grids, the model accommodates any externally defined communication infrastructure. Because typically not all grid network nodes can be measured, we use the Kalman Decomposition to reduce the model. We then apply the Gershgorin Disc theorem to create necessary but not sufficient conditions for system stability. Stability of the dynamical system ensures that all network voltages are driven to the 5% ANSI range, and that the power flow state of the grids is optimal. Using these stability conditions, we consider a more holistic set of design considerations. Specifically, we prove relationships between DER and sensor location and system stability, which inform strategic placement of this control equipment. Additionally, we develop an analytic approximation of the region of stabilizing controllers, which enables the computation of flexible operating parameter ranges for each DER. As an alternative to parameter ranges, we also propose a heuristic sampling algorithm that computes control parameters in a less conservative manner. Finally, stabilizing controllers are designed and implemented in several realistic scenarios of the 123-node unbalanced grid network. Through the experiments, we demonstrate that for any externally given communication requirements, our modeling and analysis determines strategic placement and flexible parameters for the DER set-point controllers, resulting in highly effective regulation of voltages and power flows.

3.1 Introduction

The recent literature on ways to regulate distribution grid voltages using inverter-based DERs can be categorized by the underpinning communication infrastructure.

On one end of the spectrum, DER power set-points are computed using voltages measured at their own terminals and without any communication between DERs (so called *local voltage control*). The standard voltage control function for DERs is droop volt-var control (DVVC) as proposed by IEEE 1547. Unfortunately, various works have demonstrated how oscillations can arise from DVVC [46,53]. In response, authors in [28,38] derive conditions on slope parameters to prevents these oscillations. The authors in [20,54] solve a centralized optimization problem to determine optimal droop parameters, while authors in [18,19] solve a local optimization problem over a daily horizon to adjust droop volt-var and volt-watt parameters. Finally, authors in [12,44] propose incremental volt-var to achieve better voltage regulation and accompany their approach with conditions for preventing oscillations.

The other end of the spectrum, set-points are computed with communication betwen neighboring DERs to solve an OPF problem in a distributed manner. For example, the authors in [55,56] require a communication channel between neighboring DERs in the proposed distributed optimal power flow (OPF) problem, where reactive power-setpoints are assigned to DERs across a subset of the distribution network nodes. The authors in [57, 58] also use a communication channel between neighboring DERs in the proposed distributed OPF problem, where both real and reactive power setpoints are assigned to grid-connected DERs. Unfortunately, the aforementioned works require a bi-directional communication channel to transmit measurement and actuation signals from each DER to the respective neighboring DERs, which may be impractical or expensive to implement in distribution grids [59].

The PBC framework that has been proposed and demonstrated in prior works (see Chapter 2 section 2.3) leverages the benefits at both ends of the aforementioned spectrum using a two-layer hierarchical setup. However, we emphasize that the communication requirements of real power grids are likely to fall anywhere on this spectrum depending on the resources available and concerns around privacy and ownership. Therefore, we note that existing literature has not yet adopted a communication agnostic approach to DER control, where the communication structure can be specified externally by the DER owner and operator.

We also note that the aforementioned literature often implements their proposed control approaches with a narrow focus on selecting fixed control parameters. Yet there is a more holistic set of design considerations that each play an important role in achieving effective regulation of power flows and voltages. For example, an important yet rarely explored design consideration is DER siting. This is of importance when there are a limited number of DERs but several locations at which to regulate voltages. [60] places a single DER at the end of the 30-bus single phase feeder to improve voltages along the length of the feeder. Authors in [12,13] cite incremental volt-var controllers on five evenly spaced edge nodes of the single phase 42 and 56-bus network respectively. Authors in [56] cites at 2 particular nodes on the IEEE 123-node feeder. None of these aforementioned works provide guidance on how to site the DERs, specifically they do not examine the relationship between DER siting and the convergence of the voltage to appropriate values. One exception is the work in [44]. After siting incremental volt-var DERs at all nodes of the network, the authors derive a stability region to show that siting DERs at the ends of feeders reduces the stability region where voltages converge.

Another design consideration would be an allowance of operating parameter flexibility, since grid operators and customers often have differing control objectives. Stability regions can provide this flexibility of parameter selection by showing the impact of operating parameters on stability [1,61]. Authors in [1] compute a stability region in the space of parameters for incremental volt-var controllers. Then they propose the idea of allowing customers to modulate the parameters in the range but the authors do not assess the conservative-ness of the ranges as the DER system scales. Authors in [61] develop a computationally efficient way of computing ranges of operating parameters for large groups of DERs. However, they do so by exploiting the properties of their DER voltage source converter model, which have different modeling assumptions than our focus on power set-point DER control literature. We are motivated by [1] and [61] to explore the economic value of allowing customers to operate within a computed range of stable operating parameters.

The rest of this chapter organized as follows. In Sec. 3.2, we derive a state space model for DERs operating under PBC. In Sec. 3.3, we establish conditions for system stability and relationships between DER siting and stability. In Sec. 3.4, we formalize the problem of finding a set of stabilizing controller gains for our developed model. We then propose a an analytic approximation of the region of stabilizing controllers in Sec. 3.5, and a heuristic algorithm for sampling candidate controllers in Sec. 3.6. Sec. Sec. 3.5 and 3.6 both include experimental case studies of the controller design applied to the IEEE 123-node test feeder.

3.2 Dynamical System Model for Phasor-Based Control

3.2.1 Siting of DERs and Sensors

On many power grids there is not sufficient infrastructure for DERs to inject power at *every* node, nor sensors that deliver voltage measurements to controllers at *every* node. Often the sensors used for control are those that are internal to the inverter device, resulting in an arrangement of DERs and sensors where the set of DER nodes is equal to the set of sensor nodes. However, basic voltage magnitude sensors and distribution-level voltage phasor sensors (such as μPMUs) can be installed at voltage-violation prone locations without needing to be co-located with an inverter device. Hence, we model the set of DER nodes and set of sensor nodes as separate sets. Specifically, we construct ordered sets $\mathcal{D}_1$ and $\mathcal{S}_1$

as the subset of the nodes that have DERs and sensors respectively:

$$\begin{aligned}
\mathcal{S}_1 &= \{p \mid p \in \mathcal{N} \text{ has a sensor}\} && \text{(3.1a)}\\
\mathcal{S}_2 &= \{p+n \mid p \in \mathcal{N} \text{ has a sensor}\} && \text{(3.1b)}\\
\mathcal{S} &\coloneqq \{\mathcal{S}_1, \mathcal{S}_2\} && \text{(3.1c)}\\
\mathcal{D}_1 &= \{p \mid p \in \mathcal{N} \text{ has a DER}\} && \text{(3.1d)}\\
\mathcal{D}_2 &= \{p+n \mid p \in \mathcal{N} \text{ has a DER}\} && \text{(3.1e)}\\
\mathcal{D} &\coloneqq \{\mathcal{D}_1, \mathcal{D}_2\} && \text{(3.1f)}
\end{aligned}$$

In constructing $\mathcal{S}$ in (3.1), we include the nodes that have a sensor twice because we are interested in tracking voltage magnitude *and* phase angle. Similarly, for $\mathcal{D}$ we include the nodes that have a DER twice because each DER actuates reactive power *and* real power. We label the dimension of these sets with $s \coloneqq |\mathcal{S}| \leq 2n$ and $d \coloneqq |\mathcal{D}| \leq 2n$. We also define complements $\overline{\mathcal{S}} \coloneqq \{1, ..., 2n\} \setminus \mathcal{S}$ and $\overline{\mathcal{D}} \coloneqq \{1, ..., 2n\} \setminus \mathcal{D}$.

Next we define a function Γ that generates row and column selector matrices. For an ordered set $\Omega = \{i_1, \ldots, i_g\} \subset \mathbb{N}$, we define

$$\Gamma_k(\Omega) = \begin{bmatrix} e_{i_i} & \ldots & e_{i_g} \end{bmatrix} \in \mathbb{R}^{k \times g}, \tag{3.2}$$

where e_i is the i-th standard basis vector of $\mathbb{R}^k$.

DER Coordination Problem

In Fig. 3.1, we present a conceptual diagram for a medium voltage distribution circuit with DERs, sensors and controllers. Each DER controller receive measurements of voltage magnitude and phase angle from one or more nodes as indicated by the dotted arrows. Then each controller computes real and reactive power setpoints for the DER. Though in this Chapter we model DERs operating under PBC, the approaches therein can be applied to any computation of DER power setpoints using voltage measurements. We consider each *load* as an industrial or commercial customer, or a collection of low-voltage residential or commercial customers, potentially seeking to install behind-the-meter DERs.

To describe the control system illustrated in Fig 3.1 acting over time, we introduce notation for defining time steps. For each controller, we denote the set of time indices $\mathcal{K} = \{1, ..., k, ..., K\}$. We denote by Δ the length of one time interval (i.e., $[(k-1)\Delta, k\Delta]$), and we define a time horizon $\tau = K\Delta$, so that $\mathcal{T} = [0,\ \tau]$. Consistent with volt-var control literature [1,12,38,44], we assume the sub-second dynamics from inverters, lines, and loads are stable, and that those dynamics reach steady state between time steps such that $\Delta = 5$ seconds is sufficiently large. Moreover, we assume that the grid's voltage and current waveforms are approximately sinusoidal, so that measurement and tracking of specific voltage phasor quantities is possible. Finally, we assume all DERs are synchronized to a common clock signal.

In what follows, we consider a scenario in which the capacity of a distribution network can be expanded to host DERs of capacity C across all nodes $n \in \mathcal{N}$. To be strategic

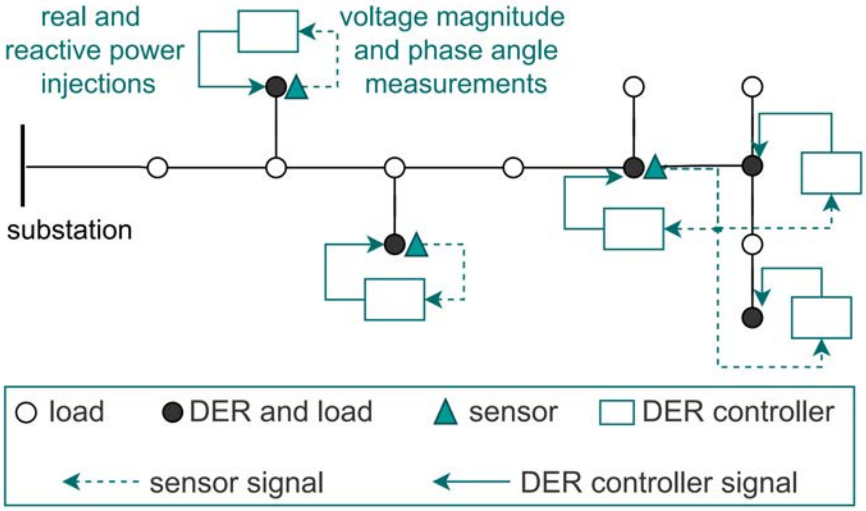

Figure 3.1: Toy diagram of DER system operating on a radial distribution network. Controllers in each DER device take measurements from one or more sensor nodes to compute power values that are injected at DER nodes.

about the expansion, we seek to determine the subset of nodes $n \in \mathcal{N}$ where siting DERs of capacity C ensures voltages and thermal constraints are within grid operating limits.

3.2.2 Introduction to Gershgorin Theorem

As will be shown in section 3.2.4 , the system described in Fig. 3.1 can be modeled as a linear, time-invariant system whose small-signal stability is determined by a single matrix. Because the matrix size grows with the number of DERs and sensors on the grid network, expressing its eigenvalues in terms of the DER controller gains and network impedances is not tractable for large DER systems. Instead, in section 3.2.6 we use the Gershgorin disc theorem, which bounds the eigenavlues of any matrix in terms of its elements.

The Gershgorin disc theorem is as follows. For any square matrix $\boldsymbol{A}$, there exists $\boldsymbol{A} = \boldsymbol{D} + \boldsymbol{P}$, where $\boldsymbol{D} = diag(\boldsymbol{A}_{11}, ..., \boldsymbol{A}_{nn})$, and $\boldsymbol{P} = \boldsymbol{A} - \boldsymbol{D}$ has a zero main diagonal. If $\boldsymbol{P} = \boldsymbol{0}_{n\times n}$, the eigenvalues of $\boldsymbol{A}$ are just along the diagonal of $\boldsymbol{D}$. We denote the deleted absolute row sums of $\boldsymbol{A}$ as

$$\gamma_i(\boldsymbol{A}) = \sum_{j\neq i} |\boldsymbol{A}_{ij}|, \quad i = 1, ..., n.$$

and denote the diagonal elements of A as

$$\phi_i(\boldsymbol{A}) = \boldsymbol{A}_{ii}$$

Theorem 1. ***([62, Theorem 6.1.1]):*** *(Gersgorin) The eigenvalues of any matrix $A \in \mathbb{R}^{n \times n}$ are in the union of its Gersgorin discs defined by*
$\mathcal{G}_i(\boldsymbol{A}) = \{w \in \mathbb{C} : |w - \phi_i(\boldsymbol{A})| \leq \gamma_i(\boldsymbol{A})\} \quad i = 1, ..., n$

Each Gershgorin disc center ϕ_i and radii γ_i can be easily computed from the diagonal elements and row sums of the matrix. The Gershgorin discs are faster to compute than the eigenvalues themselves, and can be used to define stability regions.

3.2.3 Model Derivation

In this section we derive a state space model for DERs operating under the PBC framework. The model derivation has similarities in procedure with incremental volt-var control literature such as [1, 12, 44], but notably incorporates the voltage phase angle as a state, and incorporates the change in real power setpoint as an input. It is also formulated to accommodate and externally defined arrangement and communication infrastructure between DERs and sensors.

We begin by considering a single-phase radial distribution network. Because the substation of a distribution grid interfaces with the transmission grid, the substation has a large source impedance, resulting in it being effectively a voltage source modeled with constant voltage magnitude and phase angle. The remaining n nodes are modeled as loads with a constant real and reactive power injection at each time step. If power is generated at a node, the generation is subtracted from the power consumption to yield the net load.

A radial distribution network is typically modeled as a tree graph. It consists of a set of nodes $\mathcal{N}_0 = \{0, 1, ..., n\}$ where node 0 is the root of the tree graph. Node 0 represents the distribution grid substation, and The set of graph edges $\mathcal{L}$ is denoted by $\mathcal{L} \subset \mathcal{N}_0 \times \mathcal{N}_0$, where edge $(i, j) \in \mathcal{L}$ represents a line segment from node i to node j. The distribution network can then be represented by the graph $\mathcal{G} = (\mathcal{N}_0, \mathcal{L})$. Each node has a unique path to node 0 because of the tree topology of the network. For each node $i \in \mathcal{N}_0$, denote by $\mathcal{L}_i \subset \mathcal{L}$ the set of lines on the unique path from node 0 to node i. A node j is *upstream* from node i if $\mathcal{L}_j \subset \mathcal{L}_i$. Conversely, a node j is *downstream* from node i if $\mathcal{L}_j \supset \mathcal{L}_i$. We often refer to the set of nodes downstream of node 0, denoted by $\mathcal{N} = \mathcal{N}_0 \setminus \{0\}$.

Power Flow Linearization

For each node $i \in \mathcal{N}$, the voltage magnitude, voltage phase angle, net real power generation and net reactive power generation are denoted by V_i, δ_i, p_i, and q_i, respectively. The voltage phase angle δ_i is defined with respect to a reference phase angle, typically chosen to be at the substation node. The sign of p_i and q_i is consistent with the positive generation convention. Line segments can represent either a low-voltage or a medium-voltage network. For each line segment $(i, j) \in \mathcal{L}$, the impedance of the line z_{ij} is represented by the line resistance and reactance in complex form $z_{ij} = r_{ij} + \mathbf{j}x_{ij} \in \mathbb{C}$. Additionally, the real (reactive) power flow of the line segment from i to j is P_{ij} (Q_{ij}).

We first consider the linearized branch flow model (LinDistFlow equations) developed in [27] for radial distribution networks. The LinDistFlow equations linearize around a flat voltage profile at 1 per unit and approximate the line current as zero. As such, the authors assume negligible power losses in line segments, yet are able to model distribution-level power networks with satisfactory accuracy as reported in [1, 12, 28]. A single-phase representation of the LinDistFlow equations is expressed by

$$P_{ij} = \sum_{k:(j,k)\in\mathcal{L}} P_{jk} - p_j, \quad \forall j \in \mathcal{N}, \tag{3.3a}$$

$$Q_{ij} = \sum_{k:(j,k)\in\mathcal{L}} Q_{jk} - q_j, \quad \forall j \in \mathcal{N}, \tag{3.3b}$$

$$(V_i)^2 = (V_j)^2 + 2(x_{ij}Q_{ij} + r_{ij}P_{ij}) \quad \forall (i,j) \in \mathcal{L}. \tag{3.3c}$$

Next, we consider an extension of the LinDistFlow equations that captures the voltage phase angle difference between two nodes [17, 29, 30]. We do so because modeling voltage phase angle differences is central to PBC. The phase angle equation is linearized by assuming the small-angle approximation $\sin\delta \approx \delta$ and that $V_i \approx V_j \approx 1 p.u.$. It is expressed by

$$\delta_i - \delta_j = -r_{ij}Q_{ij} + x_{ij}P_{ij} \; \forall (i,j) \in \mathcal{L}. \tag{3.4}$$

Using the vector notation (2.4), the voltage magnitude branch flow equation (3.3) and phase angle equation (3.4) are arranged into the following form:

$$\boldsymbol{v} = \boldsymbol{X}^0\boldsymbol{q} + \boldsymbol{R}^0\boldsymbol{p} + \boldsymbol{v}_0 \tag{3.5a}$$

$$\boldsymbol{\delta} = -\frac{1}{2}\boldsymbol{R}^0\boldsymbol{q} + \frac{1}{2}\boldsymbol{X}^0\boldsymbol{p} + \boldsymbol{\delta}_0. \tag{3.5b}$$

The (i,j)th element of impedance matrices $\boldsymbol{R}^0 \in \mathbb{R}^{n\times n}$ and $\boldsymbol{X}^0 \in \mathbb{R}^{n\times n}$ are constructed by

$$\boldsymbol{R}^0_{ij} = 2 \sum_{(w,t)\in\mathcal{L}_i\cap\mathcal{L}_j} r_{wt} \tag{3.6a}$$

$$\boldsymbol{X}^0_{ij} = 2 \sum_{(w,t)\in\mathcal{L}_i\cap\mathcal{L}_j} x_{wt}, \tag{3.6b}$$

where the set of nodes that are upstream of both i and j is $\mathcal{L}_i \cap \mathcal{L}_j$. The construction (3.6) is consistent with [1, 12, 13, 16, 18].

The (i,j)th *power-voltage sensitivity* is the static mapping of a power injection at node i to the voltage at node j on a circuit. Under the assumptions of linearized power flow, (3.5) indicates that the power-voltage sensitivities are the impedance matrices $\boldsymbol{R}^0$ and $\boldsymbol{X}^0$ [12, 19, 32, 36]. We then define the complex impedance matrix $\boldsymbol{Z} := \boldsymbol{R}^0 + j\boldsymbol{X}^0$. We note that the representations of the grid with single-phase impedances can be extended to three-phase impedances by simple replacement of each element of $\boldsymbol{R}^0$ and $\boldsymbol{X}^0$ by a 3×3 matrix that represents phase A, B, and C [29,38]. In section 3.5 and 3.6 we simulate this model on three-phase unbalanced grids. In the meantime, we continue with single-phase representations to focus on graph network properties and the model derivation. As such, we refer to the 'common-node impedance' as

As such, we refer to the *common-node impedance* as

$$|\boldsymbol{Z}_{ij}| = \sqrt{\boldsymbol{X}_{ij}^2 + \boldsymbol{R}_{ij}^2}. \tag{3.7}$$

It is a measure of electrical distance between any pair of nodes (i, j) on a radial network [37]. In Fig. 3.2, for different pairs of nodes i and j we compare $|\boldsymbol{Z}_{ij}|$ by observing the set of common upstream nodes. This figure highlights the fact that actuation of real or reactive power at node i has a higher impact on the voltage at node j if they share more common upstream nodes than if they share less.

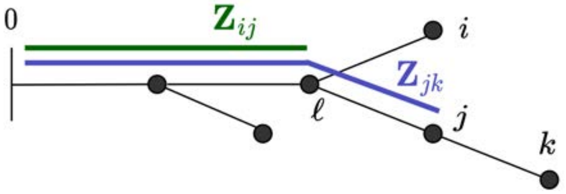

Figure 3.2: Network graph representation of a radial distribution grid. The path of the common-node impedances $\boldsymbol{Z}_{ij}$ and $\boldsymbol{Z}_{ij}$ are marked in green and purple respectively.

In the next two sections, we use (3.5a) and (3.5b) to derive the state space equations for PBC.

Voltage Magnitude Dynamics

We first split the nodal power injection vector into components

$$\boldsymbol{p} = \boldsymbol{p}^{inv,0} + \boldsymbol{p}^{other}, \quad \boldsymbol{q} = \boldsymbol{q}^{inv,0} + \boldsymbol{q}^{other}. \tag{3.8}$$

Power injections by devices under our control are $(\boldsymbol{q}^{inv,0}, \boldsymbol{p}^{inv,0})$, and those not under our control are $(\boldsymbol{q}^{other}, \boldsymbol{p}^{other})$. Next, using the Γ function (3.2), we define

$$\boldsymbol{T}^d := \Gamma_n(\mathcal{D}_1) \in \mathbb{R}^{n \times d/2}. \tag{3.9}$$

Note that $p^{inv,0}$ and $q^{inv,0}$ have the property where $p_i^{inv,0} = 0$ and $q_i^{inv,0} = 0$ for $i \in \overline{\mathcal{D}}_1$. We capture this zero pattern with

$$\boldsymbol{T}^d(\boldsymbol{T}^d)^\dagger p^{inv,0} = p^{inv,0}, \quad \boldsymbol{T}^d(\boldsymbol{T}^d)^\dagger q^{inv,0} = q^{inv,0}. \tag{3.10}$$

Then we define

$$\boldsymbol{R} \coloneqq \boldsymbol{R}^0\boldsymbol{T}^d, \quad \boldsymbol{X} \coloneqq \boldsymbol{X}^0\boldsymbol{T}^d. \tag{3.11}$$

Next we define

$$\boldsymbol{p}^{inv} \coloneqq (\boldsymbol{T}^d)^\dagger \boldsymbol{p}^{inv,0}, \quad \boldsymbol{q}^{inv} \coloneqq (\boldsymbol{T}^d)^\dagger \boldsymbol{q}^{inv,0}. \tag{3.12}$$

By construction, $\boldsymbol{p}^{inv} \in \mathbb{R}^{d/2}$ and $\boldsymbol{q}^{inv} \in \mathbb{R}^{d/2}$ are the power injections of only the nodes with a DER. Finally, we pre-multiply both sides of (3.12) by $\boldsymbol{R}^0$ then substitute in (3.10) and (3.11), resulting in

$$\boldsymbol{R}^0\boldsymbol{p}^{inv,0} = \boldsymbol{R}^0\boldsymbol{T}^d(\boldsymbol{T}^d)^\dagger\boldsymbol{p}^{inv,0} = \boldsymbol{R}^0\boldsymbol{T}^d\boldsymbol{p}^{inv} = \boldsymbol{R}\boldsymbol{p}^{inv}, \tag{3.13a}$$

$$\boldsymbol{X}^0\boldsymbol{q}^{inv,0} = \boldsymbol{R}^0\boldsymbol{T}^d(\boldsymbol{T}^d)^\dagger\boldsymbol{q}^{inv,0} = \boldsymbol{X}^0\boldsymbol{T}^d\boldsymbol{q}^{inv} = \boldsymbol{X}\boldsymbol{q}^{inv}. \tag{3.13b}$$

The lefthand side of (3.13a) and (3.13b) considers impedances and power injections at all nodes, while the righthand side considers those quantities coming from only the nodes with a DER.

Then we substitute (3.8) into the voltage equation (3.5a). By defining $\tilde{\boldsymbol{v}} \coloneqq \boldsymbol{R}^0\boldsymbol{p}^{other} + \boldsymbol{X}^0\boldsymbol{q}^{other} + \boldsymbol{v}_0$, we have $\boldsymbol{v} = \boldsymbol{R}^0\boldsymbol{p}^{inv,0} + \boldsymbol{X}\boldsymbol{q}^{inv,0} + \tilde{\boldsymbol{v}}$. Then substituting (3.13a) and (3.13b) into this result, we have

$$\boldsymbol{v} = \boldsymbol{R}\boldsymbol{p}^{inv} + \boldsymbol{X}\boldsymbol{q}^{inv} + \tilde{\boldsymbol{v}}. \tag{3.14}$$

We consider equation (3.14) at time index k and $k+1$, and subtract them from each other, giving

$$\begin{aligned}\boldsymbol{v}[k+1] = \boldsymbol{v}[k] + \boldsymbol{R}(\boldsymbol{p}^{inv}[k+1] - \boldsymbol{p}^{inv}[k]) + \boldsymbol{X}(\boldsymbol{q}^{inv}[k+1]& \\ - \boldsymbol{q}^{inv}[k]) + (\tilde{\boldsymbol{v}}[k+1] - \tilde{\boldsymbol{v}}[k]).&\end{aligned} \tag{3.15}$$

We define $\boldsymbol{u}^p[k] \coloneqq \boldsymbol{p}^{inv}[k+1] - \boldsymbol{p}^{inv}[k]$, $\boldsymbol{u}^q[k] \coloneqq \boldsymbol{q}^{inv}[k+1] - \boldsymbol{q}^{inv}[k]$, and $\boldsymbol{d}^v[k] \coloneqq \tilde{\boldsymbol{v}}^1[k+1] - \tilde{\boldsymbol{v}}^1[k]$. Suppose the voltage magnitude *squared* reference and voltage phase angle reference ($\boldsymbol{v}^{ref}$,$\boldsymbol{\delta}^{ref}$) are known. Subtracting $\boldsymbol{v}^{ref}$ from both sides gives

$$\begin{aligned}\boldsymbol{v}[k+1] - \boldsymbol{v}^{ref}[k+1] = (\boldsymbol{v}[k] - \boldsymbol{v}^{ref}[k]) + (\boldsymbol{v}^{ref}[k]& \\ - \boldsymbol{v}^{ref}[k+1]) + \boldsymbol{R}\boldsymbol{u}^p[k] + \boldsymbol{X}\boldsymbol{u}^q[k] + \boldsymbol{d}^v[k].&\end{aligned} \tag{3.16}$$

Finally, with defining $\boldsymbol{e}^v[k] \coloneqq \boldsymbol{v}[k] - \boldsymbol{v}^{ref}$ and $\boldsymbol{\xi}^v[k] \coloneqq \boldsymbol{v}^{ref}[k] - \boldsymbol{v}^{ref}[k+1]$, the upper half of our state space model is

$$\boldsymbol{e}^v[k+1] = \boldsymbol{e}^v[k] + \boldsymbol{R}\boldsymbol{u}^p[k] + \boldsymbol{X}\boldsymbol{u}^q[k] + \boldsymbol{\xi}^v[k] + \boldsymbol{d}^v[k]. \tag{3.17}$$

Voltage Phase Angle Dynamics

We follow a similar procedure to the previous section, but work with the phase angle equation (3.5b). Substituting (3.8) into (3.5b) and defining $\tilde{\boldsymbol{\delta}} := -\frac{1}{2}\boldsymbol{R}^0\boldsymbol{p}^{other} + \frac{1}{2}\boldsymbol{X}^0\boldsymbol{q}^{other} + \boldsymbol{\delta}_0$ gives $\boldsymbol{\delta} = -\frac{1}{2}\boldsymbol{R}^0\boldsymbol{p}^{inv,0} + \frac{1}{2}\boldsymbol{X}^0\boldsymbol{q}^{inv,0} + \tilde{\boldsymbol{\delta}}$. Then substituting (3.13a) and (3.13b) to this result, we have

$$\boldsymbol{\delta} = -\frac{1}{2}\boldsymbol{R}\boldsymbol{p}^{inv} + \frac{1}{2}\boldsymbol{X}\boldsymbol{q}^{inv} + \tilde{\boldsymbol{\delta}}. \tag{3.18}$$

We consider (3.18) at time index k and $k+1$, and subtract them from each other, giving

$$\boldsymbol{\delta}[k+1] = \boldsymbol{\delta}[k] - \frac{1}{2}\boldsymbol{R}(\boldsymbol{p}^{inv}[k+1] - \boldsymbol{p}^{inv}[k]) + \frac{1}{2}\boldsymbol{X}(\boldsymbol{q}^{inv}[k+1] - \boldsymbol{q}^{inv}[k]) + (\tilde{\boldsymbol{\delta}}[k+1] - \tilde{\boldsymbol{\delta}}[k]). \tag{3.19}$$

Subtracting $\boldsymbol{\delta}^{ref}$ from both sides gives

$$\boldsymbol{\delta}[k+1] - \boldsymbol{\delta}^{ref}[k+1] = (\boldsymbol{\delta}[k] - \boldsymbol{\delta}^{ref}[k]) + (\boldsymbol{\delta}^{ref}[k] - \boldsymbol{\delta}^{ref}[k+1]) - \frac{1}{2}\boldsymbol{R}\boldsymbol{u}^p[k] + \frac{1}{2}\boldsymbol{X}\boldsymbol{u}^q[k] + \boldsymbol{d}^\delta[k]. \tag{3.20}$$

Finally, with defining $\boldsymbol{e}^\delta := \boldsymbol{\delta} - \boldsymbol{\delta}^{ref}$ and $\boldsymbol{\xi}^\delta := \boldsymbol{\delta}^{ref}[k] - \boldsymbol{\delta}^{ref}[k+1]$, the lower half of our state space model is:

$$\boldsymbol{e}^\delta[k+1] = \boldsymbol{e}^\delta[k] - \frac{1}{2}\boldsymbol{R}\boldsymbol{u}^p[k] + \frac{1}{2}\boldsymbol{X}\boldsymbol{u}^q[k] + \boldsymbol{\xi}^\delta[k] + d^\delta[k]. \tag{3.21}$$

3.2.4 Model Definition

The state vector of the PBC state space model, $\boldsymbol{e}$, is the squared voltage magnitude tracking error $\boldsymbol{e}^v$ stacked with the phase angle tracking error $\boldsymbol{e}^\delta$ at all nodes. The input vector, $\boldsymbol{u}$, is the *change* in inverter reactive power setpoint $\boldsymbol{u}^q[k]$ stacked with the *change* in inverter real power setpoints $\boldsymbol{u}^p[k]$ at the DER nodes. Finally, we consider the output read-out map of the state space model. Using the Γ function (3.2), we define

$$\boldsymbol{T}^s := \Gamma(\mathcal{N}_s) \in \mathbb{R}^{s \times 2n} \tag{3.22}$$

to capture how we can only measure voltage phasors at nodes of the network that have a sensor. Therefore, the output read-out map is $y[k] = \boldsymbol{T}^s e[k]$. Then, the PBC open-loop model is

$$\text{sys } \Sigma^1 :$$

$$\begin{bmatrix} \boldsymbol{e}^v[k+1] \\ \boldsymbol{e}^\delta[k+1] \end{bmatrix} = \boldsymbol{A} \begin{bmatrix} \boldsymbol{e}^v[k] \\ \boldsymbol{e}^\delta[k] \end{bmatrix} + \boldsymbol{B} \begin{bmatrix} \boldsymbol{u}^q[k] \\ \boldsymbol{u}^p[k] \end{bmatrix} + \begin{bmatrix} \boldsymbol{\xi}^v[k] \\ \boldsymbol{\xi}^\delta[k] \end{bmatrix} + \begin{bmatrix} \boldsymbol{d}^v[k] \\ \boldsymbol{d}^\delta[k] \end{bmatrix}, \tag{3.23a}$$

$$\boldsymbol{y}[k] = \boldsymbol{C} \begin{bmatrix} \boldsymbol{e}^v[k] \\ \boldsymbol{e}^\delta[k] \end{bmatrix}, \tag{3.23b}$$

$$\boldsymbol{A} = I_{2n}, \quad \boldsymbol{B} = \begin{bmatrix} \boldsymbol{X} & \boldsymbol{R} \\ -\frac{1}{2}\boldsymbol{R} & \frac{1}{2}\boldsymbol{X} \end{bmatrix}, \quad \boldsymbol{C} = \boldsymbol{T}^s \tag{3.23c}$$

Equation (3.23) represents a quasi-steady-state dynamical system describing the evolution of voltage phasors as nodal power injections are updated over time on a radial network. Note that $\boldsymbol{e}$, $\boldsymbol{u}$, and $\boldsymbol{y}$ have dimension $2n$, d, and s, respectively. Also, B and C have dimensions $2n \times d$ and $s \times 2n$ respectively.

We use an output feedback control law for updating the power setpoint:

$$\boldsymbol{u}[k] = -\boldsymbol{F}\boldsymbol{y}[k], \tag{3.24}$$

where $\boldsymbol{F} \in \mathbb{R}^{d \times s}$. Note that we map the voltage phasor tracking error $\boldsymbol{y}$ to the *change* in inverter power output $\boldsymbol{u}$, so that inverter power injections increment while voltage phasor tracking errors persist. The incremental control law (3.24), which can be viewed as a discrete-time integrator, is of the same form as those proposed in [1,12,13,44]. However, those works assume $\boldsymbol{F}$ to be diagonal, which corresponds to a CI in which DERs are co-located with their sensors. We allow for $\boldsymbol{F}$ to have any sparsity structure, in order to allow for an arbitrarily given communication infrastructure (CI). For example, DERs at two nodes could track a phasor at a third node, as illustrated by the dotted arrows at the end of the circuit in Fig. 3.1.

By substituting the output feedback control law (3.24) and output read-out map (3.23b) into open-loop model (3.23a), the closed-loop system becomes

$$\boldsymbol{e}[k+1] = (\boldsymbol{A} - \boldsymbol{B}\boldsymbol{F}\boldsymbol{C})\boldsymbol{e}[k] + \boldsymbol{\xi}[k] + \boldsymbol{d}[k], . \tag{3.25}$$

Power disturbances from uncontrolled sources such as load changes, cloud cover events, and solar PV fluctuations can cause voltage spikes resulting in unintended device tripping. We will model these disturbances with time-series profiles as done in [1, 44]. We assume the profiles do not bring the system operating point far from the linearization equilibrium of 1V p.u. Modelled this way, the stability of the closed loop system is determined solely by the eigenvalues of $(\mathbf{A} - \mathbf{BFC})$; which are independent of $\boldsymbol{\xi}[k]$ and $\boldsymbol{d}[k]$, and so we set $\boldsymbol{\xi}[k] = \boldsymbol{d}[k] = \mathbf{0}$. The resulting closed-loop system of Σ^1 becomes

$$\boldsymbol{e}[k+1] = (I - \boldsymbol{B}\boldsymbol{F}\boldsymbol{C})\boldsymbol{e}[k], \tag{3.26}$$

since $A = I_{2n}$. Equation (3.26) defines a linear time-invariant system with dynamic elements arising from discrete-time integral control action.

3.2.5 Model Reduction

In this section we reduce the state space model of (system Σ^1) to a state space minimal realization (system Σ^2) via the Kalman Decomposition. To motivate the need for model reduction, we make some observations about it:

Lemma 1. *Consider a DER system* Σ^1 *defined in* (3.23). $\boldsymbol{T}^s$ *defined in* (3.22) *spans the observable subspace of* Σ^1, *and* $\Gamma_{2n}(\mathcal{D})$ *spans the controllable subspace of* Σ^1.

As described in section 3.2.1, it is common for $s < 2n$ and $d < 2n$ for real power grids. By Lemma 1, we construct the permutation matrix $\boldsymbol{T}$ by considering the spans of all combinations of observable and controllable subspaces. That is,

$$\boldsymbol{T} \coloneqq [\boldsymbol{\Gamma}_{2n}(\mathcal{S} \cap \mathcal{D}),\ \boldsymbol{\Gamma}_{2n}\left(\mathcal{S} \cap \overline{\mathcal{D}}\right),\ \boldsymbol{\Gamma}_{2n}\left(\overline{\mathcal{S}} \cap \mathcal{D}\right),\ \boldsymbol{\Gamma}_{2n}\left(\overline{\mathcal{S}} \cap \overline{\mathcal{D}}\right)]. \tag{3.27}$$

We obtain the Kalman Decomposition representation [63, Chapter 6.4] as $(\tilde{\boldsymbol{A}}, \tilde{\boldsymbol{B}}, \tilde{\boldsymbol{C}})$ where $\tilde{\boldsymbol{A}} = \boldsymbol{T}^{-1}\boldsymbol{A}\boldsymbol{T}$, $\tilde{\boldsymbol{B}} = \boldsymbol{T}^{-1}\boldsymbol{B}$, and $\tilde{\boldsymbol{C}} = \boldsymbol{C}\boldsymbol{T}$. Since $\boldsymbol{A} = \boldsymbol{I}_{2n}$, $\tilde{\boldsymbol{A}} = \boldsymbol{A} = \boldsymbol{I}_{2n}$. We start by extracting the the observable subsystem by defining define a selector matrix $\boldsymbol{G} \coloneqq \boldsymbol{\Gamma}(\{1...s\}) \in \mathbb{R}^{2n\times s}$. When $\boldsymbol{G}$ is post-multiplied it selects the first s columns. When when $\boldsymbol{G}^\top$ is pre-multiplied it selects the first s rows. The observable subsystem $(\bar{\boldsymbol{A}}, \bar{\boldsymbol{B}}, \bar{\boldsymbol{C}})$ is then $\bar{\boldsymbol{A}} = \boldsymbol{G}^\top \tilde{\boldsymbol{A}} \boldsymbol{G} = \boldsymbol{I}_s$, $\bar{\boldsymbol{B}} = \boldsymbol{G}^\top \tilde{\boldsymbol{B}} \in \mathbb{R}^{s\times d}$, and $\bar{\boldsymbol{C}} = \tilde{\boldsymbol{C}}\boldsymbol{G} \in \mathbb{R}^{s\times s}$.

Lemma 2. *The reduced system state vector contains only the sensor nodes of the network, i.e.* $\bar{e} = T^s e$

The reduced DER system, called Σ^2, is

$$\text{sys } \Sigma^2: \quad \bar{\boldsymbol{e}}[k+1] = \bar{\boldsymbol{A}}\bar{\boldsymbol{e}}[k] + \bar{\boldsymbol{B}}\boldsymbol{u}[k], \tag{3.28a}$$

$$\boldsymbol{y}[k] = \bar{\boldsymbol{C}}\bar{\boldsymbol{e}}[k]. \tag{3.28b}$$

By Lemma 1, $\boldsymbol{T}^s$ spans the observable subspace of Σ^1, so

System Σ^2 captures how changes in power setpoints at DER nodes affect the phasor tracking error at sensor nodes. Notice that due to the tree graph topology of the grid network, a DER could have the same common-node impedance $|\boldsymbol{Z}_{ij}|$ with respect to two sensors, which would prevent independently tracking each sensor. Thus we introduce the following assumption about the DER and sensor siting:

Assumption 6. *Consider a DER system* Σ^1 *with communication network defined in* (3.1). *We assume that for every node with a sensor, there is also an actuator at that node. That is,* $\mathcal{S} \subseteq \mathcal{D}$.

In general, applying $\boldsymbol{G}$ to the Kalman Decomposition extracts the observable subsystem matrices, which includes controllable and uncontrollable modes. However, by Assumption 6, $\mathcal{S} \subseteq \mathcal{D} \leftrightarrow \mathcal{S} \cap \bar{\mathcal{D}} = \emptyset$, so applying $\boldsymbol{G}$ extracts exactly the minimal realization. That is, under Assumption 6, system Σ^2 is both observable and controllable. Due to system Σ^2 being completely controllable, there exists a stabilizing state feedback gain matrix, $\bar{\boldsymbol{F}} \in \mathbb{R}^{d\times s}$, that satisfies

$$\boldsymbol{u}[k] = -\bar{\boldsymbol{F}}\bar{\boldsymbol{e}}[k], \tag{3.29}$$

Substituting (3.29) into (3.28) gives a closed-loop system of

$$\bar{\boldsymbol{e}}[k+1] = (\bar{\boldsymbol{A}} - \bar{\boldsymbol{B}}\bar{\boldsymbol{F}})\bar{\boldsymbol{e}}[k] = (I - \bar{\boldsymbol{B}}\bar{\boldsymbol{F}})\bar{\boldsymbol{e}}[k], \tag{3.30}$$

since $\bar{\boldsymbol{A}} = I_s$. Notably, the closed-loop dynamics matrix $(\boldsymbol{I} - \bar{\boldsymbol{B}}\bar{\boldsymbol{F}})$ is $s \times s$ dimension. The reduced state vector $\bar{\boldsymbol{e}}$ is only of dimension $s \leq 2n$, which captures the voltage phasors only at the nodes where there are sensors.

3.2.6 Stability Guarantees

In this section, we prove that the stability margin of the closed-loop of the reduced system is equal to that of the original system. We then apply the Gershgorin disc theorem to the reduced system to define closed-form analytical expressions for the stability region of the system.

We define a 2-dimensional open ball in the complex space $\mathcal{B}(c, r) = \{x \in \mathbb{C} \mid |x - c| \leq r\}$ with center $c \in \mathbb{C}$ and radius $r \in \mathbb{R}$. If $(\boldsymbol{I} - \boldsymbol{BFC}) \in \mathcal{B}(0, 1)$, the system (3.26) is asymptotically stable [63, Chapter 5.3]. Thus, from (3.26) and (3.30), $(\boldsymbol{I} - \boldsymbol{BFC})$ determines the stability of system Σ^1 and $(\boldsymbol{I} - \bar{\boldsymbol{B}}\bar{\boldsymbol{F}})$ determines the stability of system Σ^2.

We label

$$\boldsymbol{H} \coloneqq \boldsymbol{BFC} \in \mathbb{R}^{2n \times 2n} \tag{3.31}$$

$$\bar{\boldsymbol{H}} \coloneqq \bar{\boldsymbol{B}}\bar{\boldsymbol{F}} \in \mathbb{R}^{s \times s} \tag{3.32}$$

Due to the spectral mapping theorem, the eigenvalues of $(\boldsymbol{I} - \boldsymbol{H})$ are equal to one minus the eigenvalues of $\boldsymbol{H}$. Therefore, in the proofs that follow we relate the eigenvalues of $\boldsymbol{H}$ and $\bar{\boldsymbol{H}}$ to the ball $\mathcal{B}(1 + 0j, 1)$.

Lemma 3. *Consider $\boldsymbol{H}$ and $\bar{\boldsymbol{H}}$ defined in (3.31) and (3.32). We have $\bar{\boldsymbol{F}} = \boldsymbol{F}\bar{\boldsymbol{C}}$, and $\bar{\boldsymbol{H}} = \boldsymbol{G}^\top \boldsymbol{T}^{-1} \boldsymbol{H} \boldsymbol{T} \boldsymbol{G}$.*

Corollary 1. *The eigenvalues of $\boldsymbol{H}$ are the eigenvalues of $\bar{\boldsymbol{H}}$, and zero with algebraic multiplicity of $2n - s$.*

We can thus reason about how DER siting and operating parameters affect a submatrix of $\boldsymbol{H}$, rather than all elements of $\boldsymbol{H}$. The number of elements of $\boldsymbol{H} \in \mathbb{R}^{2n \times 2n}$ scales with network size, while $\bar{\boldsymbol{H}} \in \mathbb{R}^{s \times s}$ only scales with the number of nodes being tracked.

Theorem 2. *(stability assessment) Consider a DER system Σ^1 (3.26) and the reduced system Σ^2 (3.30). If for Σ^2 the eigenvalues of $\bar{\boldsymbol{H}}$ (3.32) lie strictly inside $\mathcal{B}(1+0j, 1)$, then (i) $\bar{\boldsymbol{e}}$ converges to zero exponentially, (ii) system Σ^1 is stable in the sense of Lyapunov (SISL), and (iii) e_p converges to zero exponentially $\forall p \in \mathcal{S}$.*

If DER-sensor locations and gains are known (i.e. $\boldsymbol{H}$ is known), we can use Theorem 2 to determine whether one particular instance of ($\mathcal{S}$, $\mathcal{D}$, and $\bar{\boldsymbol{F}}$) yields a stable system, i.e. a system where the phasors converge to their references. However, in practice, it is desirable to know the *region* of system parameters where stable operation is guaranteed.

Applying Theorem 2 to perform a point-by-point direct numerical assessment would require prohibitively many assessments for large systems, leading to only an approximate a stability region. Thus, we leverage the Gershgorin disc theorem to create a set of closed-form analytic inequalities that ensure convergence to the voltage references. The Gershgorin disc theorem defines Gershgorin discs whose union contains the eigenvalues of $\bar{\boldsymbol{H}}$. The system is stable if each of those Gershgorin discs are contained in $\mathcal{B}(1+0j,1)$. See the diagram in Fig. 3.3.

Theorem 3. *(closed-form analytic stability region) Consider a DER system* Σ^1*. If the following Gershgorin disc conditions on* $\bar{\boldsymbol{H}}$ (3.32) *are met,*

$$\phi_i(\bar{\boldsymbol{H}}) + \gamma_i(\bar{\boldsymbol{H}}) < 2 \tag{3.33}$$
$$\phi_i(\bar{\boldsymbol{H}}) - \gamma_i(\bar{\boldsymbol{H}}) > 0 \quad \forall\, i = 1...s \tag{3.34}$$

then, e_p *converges to zero exponentially for all* $p \in \mathcal{S}$*.*

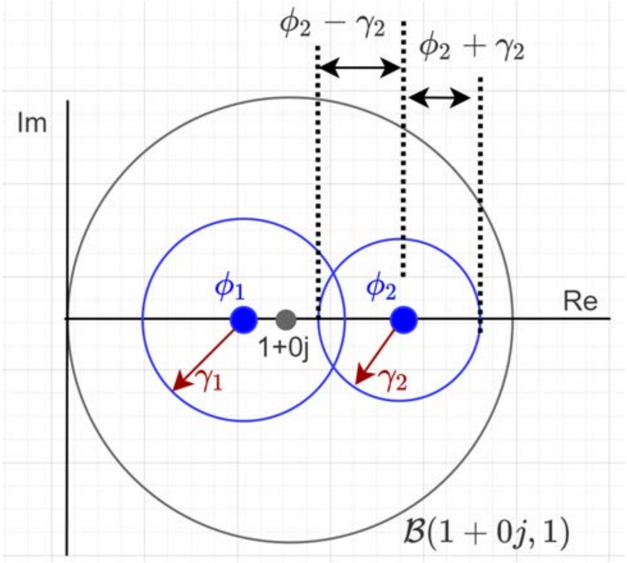

Figure 3.3: Theorem 3 represented on the real-imaginary complex plane. Two example Gershgorin discs are drawn in blue and characterized by center ϕ_i and radius γ_i for $i = 1, 2$. The stability ball $\mathcal{B}(1+0j,1)$ is drawn in black. By applying the Gershgorin Disc Theorem (Theorem 1), observe that having all Gershgorin discs of $\bar{\boldsymbol{H}}$ inside the stability ball is sufficient for stability.

The value in Theorem 3 is twofold. First, we have a geometric interpretation of the small-signal eigenvalue stability of our system, and in the proofs that follow we reason about the Gershgorin disc radii and centers to tell when the system becomes unstable. Secondly, the stability region formulated in Theorem 3 can be viewed in the electrical impedance space for DER siting insights. Conversely, it can be viewed in the controller gain space for controller gain insights.

3.3 Siting-Stability Relationships

To quantify how close a system is to the stability boundary, we define the *shifted spectral radius* for a matrix $\mathbf{A}$ as

$$\rho_c(\mathbf{A}) := \max_i |c + \lambda_i(\mathbf{A})|.$$

where λ_i indicates the i^{th} eigenvalue. Typically the spectral radius has no shift, i.e., one has ρ_0. Here, because the system Σ^1 is stable when eigenvalues of $\boldsymbol{H}$ are in $\mathcal{B}(1+0j, 1)$, if $\rho_1(\boldsymbol{H}) < 1$ then the system Σ^1 is stable. Consider the point $\boldsymbol{\epsilon} \in \mathbb{C}$ that is the furthest point from point $1+0j$ in the union of all Gershgorin disks $\mathcal{G}_i(\boldsymbol{H})$. By Theorem 1, $|\boldsymbol{\epsilon}|$ is an upper bound on $\rho_1(\boldsymbol{H})$, so we define the distance $\rho_1^{ub}(\boldsymbol{H}) = |\boldsymbol{\epsilon}|$. For any state space system with closed-loop dynamics matrix of the form $(\boldsymbol{I} - \boldsymbol{W})$, the *stability margin* of the system $m(\boldsymbol{W})$ is

$$m(\boldsymbol{W}) = 1 - \rho_1^{ub}(\boldsymbol{W}). \tag{3.35}$$

Observe that if ρ_1^{ub} increases, m decreases.

Remark 1. *System Σ^1 (3.26) having greater stability margin $m(\boldsymbol{W})$ results in faster convergence to the voltage phasor, faster rejection of disturbances, and faster achievement of the optimal grid state. See Chapter 2 section 2.3 for details on how the PBC framework achieves an optimal grid state.*

Proposition 1. *(adding and removing DER-sensor pairs) Consider a DER system Σ^1. Removing a DER-sensor pair increases the Σ^1 stability margin $m(\mathbf{H})$; adding a pair decreases the stability margin*

Proposition 1 is powerful because it implies that if a sensor becomes compromised or stops producing measurements, stability of the remaining DER system is maintained and actually improved.

3.3.1 Expansion of Stability Region Expressions

Theorem 3 expressed a stability region in terms of $\bar{\boldsymbol{H}}$ Gershgorin discs. In what follows we expand out the Gershgorin disc center and radii in terms of $\bar{\boldsymbol{B}}$ and $\bar{\boldsymbol{F}}$ elements, which allows us to express the stability region in the space of impedances (section 3.3.2), and in the space of controller gains (section 3.5).

First we express $\boldsymbol{B}$ in terms of elements of $\boldsymbol{X^0}$ and $\boldsymbol{R^0}$ from (3.6). From the construction of $\boldsymbol{R}$ and $\boldsymbol{X}$ (3.11) we have

$$\boldsymbol{B} = \left[\begin{array}{c|c} x_{i\ell} & r_{i\ell} \\ \hline -\frac{1}{2}r_{i\ell} & \frac{1}{2}x_{i\ell} \end{array}\right]$$

for $i = 1...n$ and $\ell \in \mathcal{D}_1$. Then, from the construction of $\boldsymbol{T}$ (3.27) and $\boldsymbol{G} = \boldsymbol{\Gamma}(\{1...s\})$, $\boldsymbol{G}^\top \boldsymbol{T}^{-1}\boldsymbol{B} = \boldsymbol{B}_{pi}$ for $p \in \mathcal{S}$, and $i = 1...d$. Therefore, $\bar{\boldsymbol{B}} = \boldsymbol{G}^\top \boldsymbol{T}^{-1}\boldsymbol{B}$ in terms of $\boldsymbol{X}$ and $\boldsymbol{R}$ elements is

$$\bar{\boldsymbol{B}} = \left[\begin{array}{c|c} x_{i\ell} & r_{i\ell} \\ \hline -\frac{1}{2}r_{i\ell} & \frac{1}{2}x_{i\ell} \end{array}\right] \tag{3.36}$$

for $i \in \mathcal{S}_1$ and $\ell \in \mathcal{D}_1$.

The elements of X and R are indexed by one set of indices while $\bar{\boldsymbol{H}}$ are indexed by another due to the matrices having differing dimensions. We define a function $\sigma : \mathbb{R}^1 \times \mathbb{R}^n \to \mathbb{R}^1$

$$\sigma(S, v) = u \text{ s.t. } S_u = v \tag{3.37}$$

that takes in an ordered set and a value, then outputs the index of the set where the value is found. Function (3.37) allows us to map the elements of $\boldsymbol{H}$ to those of $\bar{\boldsymbol{H}}$.

Next we substitute (3.36) into $\bar{\boldsymbol{H}} = \bar{\boldsymbol{B}}\bar{\boldsymbol{F}}$ to get $\bar{\boldsymbol{H}}$ in terms of X, R, and $\bar{\boldsymbol{F}}$ elements (which we'll label as f).

Gershgorin disc center: The diagonal elements of $\bar{\boldsymbol{H}}$ gives the first $s/2$ Gershgorin disc $\mathcal{G}(\bar{\boldsymbol{H}})$ centers as

$$\phi_c = \sum_{\ell \in \mathcal{D}_1} x_{i\ell} f_{\sigma(\ell,\mathcal{D}_1),w} + \sum_{\ell \in \mathcal{D}_1} r_{i\ell} f_{\sigma(\ell,\mathcal{D}_1),w} \tag{3.38}$$

where $i \in \mathcal{S}_1$, $w \in \{1...s\}$, and $c \in \{1...s/2\}$. For the latter $s/2$ Gershgorin discs, we have

$$\phi_c = \sum_{\ell \in \mathcal{D}_1} -\frac{1}{2} r_{i\ell} f_{\sigma(\ell,\mathcal{D}_1),w} + \sum_{\ell \in \mathcal{D}_1} \frac{1}{2} x_{i\ell} f_{\sigma(\ell,\mathcal{D}_1),w} \tag{3.39}$$

where $i \in \mathcal{S}_1$, $w \in \{1...s\}$, and $c \in \{s/2+1...s\}$. The first key is that each Gershgorin disc center ϕ represents the *self-impact* of the of the DER's power injection on the voltage it is tracking.

Gershgorin disc radius: The first $s/2$ Gershgorin disc $\mathcal{G}(\bar{\boldsymbol{H}})$ radii are

$$\gamma_c = \sum_{j \in \mathcal{S}} \left| \sum_{\ell \in \mathcal{D}_1 \setminus \{i\}} x_{i\ell} f_{\sigma(\ell,\mathcal{D}_1),w} + \sum_{\ell \in \mathcal{D}_1} r_{i\ell} f_{\sigma(\ell,\mathcal{D}_1),w} \right| \tag{3.40}$$

where $i \in \mathcal{S}_1$, $w \in \{1...s\}$, and $c \in \{1...s/2\}$. The latter $s/2$ Gershgorin disc $\mathcal{G}(\bar{\boldsymbol{H}})$ radii as $\sigma(i+n, \mathcal{S})$ are

$$\gamma_c = \sum_{j \in \mathcal{S}} \left| \sum_{\ell \in \mathcal{D}_1} -\frac{1}{2} r_{i\ell} f_{\sigma(\ell,\mathcal{D}_1),w} + \sum_{\ell \in \mathcal{D}_1 \setminus \{i\}} \frac{1}{2} x_{i\ell} f_{\sigma(\ell,\mathcal{D}_1),w} \right| \tag{3.41}$$

where $i \in \mathcal{S}_1$, $w \in \{1...s\}$, and $c \in \{s/2+1...s\}$. The second key is that each Gershgorin disc radius γ represents the *cross-impact* of other actuator power injections on the voltage of interest.

Now if we substitute (3.38), (3.39), (3.40), and (3.41) into Theorem 3, we have the expanded stability conditions:

$$RHS(3.38) + RHS(3.40) < 2 \tag{3.42a}$$

$$RHS(3.39) + RHS(3.41) < 2 \tag{3.42b}$$

$$RHS(3.38) - RHS(3.40) > 0 \tag{3.42c}$$

$$RHS(3.39) - RHS(3.41) > 0 \tag{3.42d}$$

where RHS(.) denotes a function that outputs the right-hand side of an equality. The equations (3.42) are explicit conditions on impedances and controller gains (x, r, f) that ensure convergence to the voltage phasor at sensor nodes.

These conditions are in an intuitive form. First of all, we need every Gershgorin disc to satisfy these conditions, so each can be examined independently. Equations (3.42a) and (3.42b) enforce a limit on the sum of self-impacts and cross-impacts, as they could combine in the same direction, creating overshoot or instability in the response. Then equations (3.42c) and (3.42d) indicate that when cross-impacts apply in the opposite direction to the self-impacts, the self-impacts should dominate the cross-impacts.

3.3.2 Dependence of Siting on Stability

In this section, we consider $\bar{\boldsymbol{F}}$ to be known $\bar{\boldsymbol{B}}$ elements unknown. There are three related, technical metrics for siting DERs: stability margin defined in (3.35), power-voltage sensitivities (3.5), and a third metric, which we now define.

Consider that the power injection from a DER at the very end of the circuit has the same power-voltage sensitivity with respect to a voltage sensor near the head of a circuit as a DER at the sensor location. Yet, power injected at the end of the feeder incurs a greater change of power across the substation, because it imparts greater changes to voltages at the end of the feeder. Essentially, two DERs can do the same amount of *work* on the associated sensor but differ in the *input power* exchanged across the substation. Hence we define

$$\eta = |\boldsymbol{Z}_{ij}|/|\boldsymbol{Z}_{jj}|, \tag{3.43}$$

on a DER-sensor pair. Recall that $|\boldsymbol{Z}_{ij}|$ is the common-node impedance between the sensor node i and the associated DER node j. Because $|\boldsymbol{Z}_{ij}| \leq |\boldsymbol{Z}_{ii}|\ \forall(i,j)$ (see Fig 2.1), when a DER-sensor pair is co-located, $\eta = 1$ which is the maximum efficiency.

Proposition 2. *Consider a DER system Σ^1 with no DERs. If we consider adding a new DER-sensor pair at node i with fixed $\bar{\boldsymbol{F}}$, selecting i to be deeper in the network (larger common-node impedance $|\boldsymbol{Z}_{ij}|$) increases power-voltage sensitivity, but there exists a limit* *on depth for maintaining SISL stability.*

Proposition 2 demonstrates that for a set controller gain there is a limit to how deeply you can place your DER-sensor pair to maintain stability. On small feeders and for small controller gains, all node locations may meet this impedance limit, while on larger feeders the entire downstream portion could be unstable. Other works such as [1,16,37] remark that injecting power deeper in a network as greater power-voltage sensitivity, but they do not comment on the relationship between DER depth and stability. This proposition formalizes that there is a sensitivity-stability trade-off for this control system.

Proposition 3. *Consider a DER system* Σ^1 *with multiple DER-sensor pairs. For set controller gains* $\bar{\boldsymbol{F}}$*, the stabilit of* Σ^1 *is only determined by* $(\boldsymbol{X}_{ij}, \boldsymbol{R}_{ij})\ \forall\ i \in \mathcal{S}_1$ *and* $\forall\ j \in \mathcal{D}_1$*.*

Proposition 3 establishes that the stability of the DER system is determined only by the common-node impedance between each DER and the sensors not associated with the DER; any other nodes on the network are irrelevant. That means you can use an inaccurate impedance model if the inaccurate impedances are not on the DER paths to the substation.

By Assumption 6, there is always one DER located at the sensor node. But that DER may not have enough capacity to meet the phasor tracking objective, in which case we consider DERs acting at nodes other than the sensor node.

Proposition 4. *Consider three instances of a DER system* Σ^1 *with multiple DER-sensor pairs including one sensor at node* i *and the associated DER at node* j*. Suppose all controller gains* $\bar{\boldsymbol{F}}$ *are fixed. Each instance can be characterized by the system stability margin* (3.35) *and the controller efficiency of the* (i,j)*th pair* (3.43)*:* $(\bar{\boldsymbol{H}}^p, \eta^p)$ *for* $p = 1, 2, 3$*.*

1. *The first instance has* $i = j$ *(co-located)*
2. *The second instance has* $i \neq j$ *such that* $|\boldsymbol{Z}_{ij}| < |\boldsymbol{Z}_{ii}|$*. For example, when the DER is upstream from its sensor.*
3. *The third instance has* $i \neq j$ *such that* $\boldsymbol{Z}_{ij} = \boldsymbol{Z}_{ii}$*. For example, when the DER is downstream from its sensor.*

Then, $m(\bar{\boldsymbol{H}}^1) \geq m(\bar{\boldsymbol{H}}^3)$*,* $m(\bar{\boldsymbol{H}}^2)$ *is inconclusive, and* $\quad \eta^1 = \eta^2 > \eta^3$*.*

The main takeaway is that placing a DER downstream from the associated sensor is worse both in terms of stability and efficiency. So when placing a DER that is not co-located with its associated sensor, it is better to place it upstream from the sensor. This insight is surprising, given that planners may approve interconnections for DERs on edge nodes and place sensors on more central nodes.

3.4 Structured Controller Synthesis Problem

Now that we have established how siting impacts stability of DER systems, we seek to understand how controller gains impact stability. We can formulate this investigation into the design of controllers that make the closed-loop DER system stable. As will be described, this problem is made difficult because communication requirements impose a required structure on the controllers.

As established in section 3.2.4, the reduced DER system model Σ^2 (3.28) is completely controllable. Therefore, there exists a stabilizing state feedback gain matrix, $\bar{\boldsymbol{F}} \in \mathbb{R}^{d \times s}$, that satisfies

$$\boldsymbol{u}[k] = -\bar{\boldsymbol{F}}\bar{\boldsymbol{e}}[k]. \tag{3.44}$$

We note that the stabilizing $\bar{\boldsymbol{F}}$ that exists could be totally dense. A dense $\bar{\boldsymbol{F}}$ matrix corresponds communication infrastructure (CI) where each DER has access to *all* sensor measurements. This requirement on access may incur excessive communication overhead, and may violate the privacy preferences of certain DER customers. For example, one may want to design a DER system in which DERs at two nodes only access phasor measurements at a third node. Therefore, controllability of (3.28) is not generally sufficient for designing controllers the DER system (3.28). Instead, we define the subspace $\mathcal{W} \in \mathbb{R}^{s \times s}$ to encapsulate all sparsity structure requirements on the matrix $\bar{\boldsymbol{F}}$. Then we define

$$\mathcal{I}_{\mathcal{W}} = \{(i,j) \mid \bar{\boldsymbol{F}}_{ij} = 0 \text{ is required}\}. \tag{3.45}$$

For an example of CI requirements, in droop volt-var control inverters compute power setpoints using only measurements at their own nodes [1, 12, 38, 46]. In this case, $\bar{\boldsymbol{F}}$ is required to be diagonal, and $\mathcal{I}_W = \{(i,j) \mid i \neq j \ \forall i = 1, ..., s, \ j = 1, ..., s\}$. In many distributed OPF approaches, inverters compute power setpoints using communication between only neighboring DERs [55–58]. In this case, each row of $\bar{\boldsymbol{F}}$ would have two nonzero elements for accessing voltage magnitude and voltage phase angle measurements at its own node, and two nonzero elements for each neighboring DER.

Given the circuit impedances $\bar{\boldsymbol{B}}$, DER-sensor locations ($\mathcal{N}_s$, $\mathcal{N}_d$), and CI requirements $\mathcal{I}_W$, we seek an $\bar{\boldsymbol{F}} \in W$ such that the eigenvalues of $\bar{\boldsymbol{H}}$ are in $\mathcal{B}(1 + 0j, 1)$ (see Theorem 2). More generally, we are interested in solving the following problem:

Problem 1. *(structured controller synthesis problem (P1)) Consider the lienar time-invarant system* (3.28)*. Given an arbitrary non-zero pattern $\mathcal{I}_W$, determine whether there exists a state feedback gain matrix $\bar{\boldsymbol{F}} \in W$ such that the closed-loop system* (3.30) *is exponentially stable.*

In control theory literature, solving Problem 1 is sometimes referred to as the structured static output feedback (SOF) problem [64, 65]. Due to the a-priori assigned structural constraints on the feedback gain matrix, the problem is nonconvex [64, 66]. Specifically, it is a bilinear semidefinite program that is NP-hard [67]. This literature has proposed several categories of approaches to solving Problem 1 in the optimal controller context, including iterative algorithms [68], augmented Lagrangian methods [65], and gradient projection methods [67, 69]. However, due to its nonconvexity, Problem 1 remains challenging to solve accurately for large systems, which is essential for the power grid context. In what follows, we propose two ways to solve Problem 1. The first is an analytic approximation of the region of stabilizing controllers, and the second is a heuristic algorithm for sampling candidate controllers.

3.5 Designing Parameter Ranges for Stabilizing Controllers

In this section, we consider $\bar{\boldsymbol{B}}$ to be known. We seek to characterize the set of stabilizing $\bar{\boldsymbol{F}}$ matrices that have a sparsity requirements $\mathcal{I}_{\mathcal{W}}$ associated with a given CI. By defining a stability region in terms of the non-zero $\bar{\boldsymbol{F}}$ elements, we can determine ranges of controller parameters that ensure network-wide stability.

With $\bar{\boldsymbol{B}}$ known and elements of $\bar{\boldsymbol{F}}$ unknown, the Gershgorin disc conditions from Theorem 3 are linear in the elements of $\bar{\boldsymbol{F}}$, as shown by the expanded stability conditions (3.42). We collect these elements into a vector $\boldsymbol{f} \in \mathbb{R}^y$. If there are no CI, y is simply the number of elements of a dense $\bar{\boldsymbol{F}}$; that is, $y = sd$. The linear Gershgorin disc conditions (3.42) define a convex polytope in the controller parameter space. A compact way to express $\mathcal{F}$, the Gershgorin disc stability region in the y-dimensional gain space, is

$$\begin{aligned} \mathcal{F} :=& \{\boldsymbol{f} \in \mathbb{R}^y \mid (3.42) \text{ holds}\} && (3.46) \\ =& \{\boldsymbol{f} \in \mathbb{R}^y \mid \boldsymbol{A}^+ f \leq \boldsymbol{b}^+\}. && (3.47) \end{aligned}$$

Since $\bar{\boldsymbol{H}} \in \mathbb{R}^{s \times s}$ has s Gershgorin discs, and each Gershgorin disc must satisfy two conditions, $\mathcal{F}$ comprises $2s$ conditions. Notice the absolute value operations in each condition of (3.42), which comes from the definition of Gershgorin disc radii. Each inequality has $s-1$ absolute value operations, since the the diagonal element of each row of $\bar{\boldsymbol{H}}$ is zero. For every absolute value term $|x|$, we could have $x < 0$ or $x \geq 0$. Thus there are 2^{s-1} sign possibilities for the absolute value terms in each Gershgorin disc condition. Therefore, with $2s$ Gershgorin disc conditions, $\mathcal{F}$ is defined by $2s \cdot 2^{s-1}$ inequalities.

Despite the large number of inequalities that define $\mathcal{F}$, we can still leverage the geometry of the polytope to determine *ranges* of controller parameters. Specifically, we seek to compute a y-dimensional box inside $\mathcal{F}$. The geometry of the rectangle allows each controller parameter to slide along its associated dimension freely, without any knowledge of the other DER controller parameters or network impedances. That is, one can adjust the gains of a DER without communication with other DERs while ensuring that the system is SISL. If we are interested in computing the *best* box, we could formulate a convex optimization problem (see Appendix 7.2). Unfortunately, an optimization problem may need to enforce that each vertex of the box is within the polytope. The number of vertices of a y-dimensional rectangle is 2^y. As such, the number of constraints enforced by the above problem grows exponentially with the number of controller parameters y.

To address the complexity issue of computing the the *best* box inside $\mathcal{F}$, we instead compute a square. Characterizing controller parameter ranges with a square aligns well for practical situations because it is equitable to allow each DER to have the same range. To compute a square inside a convex polytope, we can compute the Chebyshev ball of the polytops witha linear program [70, Chapter 4.3]. The largest inscribed square in the ball has width $a = \mu \cdot \sqrt{2}$, were μ is the Chebyshev ball radius. A diagram of $\mathcal{F}$ and the associated Chebyshev ball is in section 3.5.1. Note that if the Chebyshev ball has a nonzero radius, then $\mathcal{F}$ is nonempty and there exists at least one set of controller parameters adhering to the CI requirements that results in SISL stability of system Σ^1. Then, the projection of the square along dimension i is the stabilizing controller parameter range of the i^{th} DER.

Remark 2. *In the next section, we consider scenarios in which the Chebyshev ball has nonzero radius. In other cases, the polytope could be degenerate in at least one direction, which yields a Chebyshev ball with zero radius. Exploring methods for enabling a nonzero or large Chebyshev ball in the rest of the dimensions will be future work.*

3.5.1 Case Studies on DER Control using Stability Regions

In this section, we demonstrate the value in computing stability regions for DER control. We first use the stability region defined in section 3.5 to design controller gains. Then we demonstrate the value of accommodating any externally defined communication structure by comparing our model to the baseline formulation for incremental volt-var [1], where the baseline shows a danger of instability. Next we examine how conservative the gains from the stability regions are, and demonstrate how appropriate DER siting can improve the tracking performance.

3.5.2 Test Setup

Throughout this section, we consider groups of DER-sensor pairs (DSPs) acting on the IEEE 123-node unbalanced test feeder (123NF) [71]. We modify the 123NF by removing the voltage regulators and the capacitors, which exacerbates underlying voltage issues. The slack node is assigned to node 150 with a fixed and nominal voltage of 2401.8 volts line-to-line. We consider $2401.8 \cdot \sqrt{3}$ as the base voltage for computing per unit (pu) values.

For all simulations, we include time-varying load data profiles for the medium-voltage 123NF that are constructed as follows: reported spot loads on the 123NF are replaced with aggregate second-wise time-varying net load data. The data is generated based on public commercial loads, and residential loads and solar PV generation profiles from Southern California Edison recorded during a typical summer day. At each node we scale the solar power profile to have 125% solar PV penetration, which creates an overvoltage of up to

Table 3.1: DER configurations (CFGs), where each DSP is defined by a DER node (left side of →) tracking the voltage phasor at a sensor node (right side of →). The secondary columns indicate on which phases the control acts.

CFG χ_1		CFG χ_2		CFG χ_2	
$57 \rightarrow 57$	A/B/C	$56 \rightarrow 57$	B	$41 \rightarrow 49$	C
$300 \rightarrow 300$	A/B/C	$57 \rightarrow 57$	A/B/C	$45 \rightarrow 49$	A
		$63 \rightarrow 57$	A	$49 \rightarrow 49$	A/B/C
		$76 \rightarrow 76$	A/B/C	$76 \rightarrow 76$	A/B/C
		$80 \rightarrow 76$	A/B/C	$80 \rightarrow 76$	A/B/C
		$87 \rightarrow 76$	B	$87 \rightarrow 76$	B

1.065 pu (at 11:00am) when there is no DER control. PV penetration is computed as the maximum of the solar profile divided by to the maximum of the load profile.

We consider three configurations (CFGs) of DSPs, χ_i for $i = 1, 2, 3$ which are defined in Table 3.1. A DSP is *co-located* if the DER and associated sensor are at the same node. CFG χ_1 is comprised of co-located DSPs, while χ_2 and χ_3 do not have them. Each DER is considered to be a battery with unlimited stored charge. In section 3.5 we modeled a single-phase balanced feeder. To apply our approach to three-phase unbalanced feeders, we replace each element of $\boldsymbol{R}^0$ and $\boldsymbol{X}^0$ by a 3×3 matrix that represents impedances across phase A, B, and C [29, 38]. In turn, changing the nodal locations of the DERs and sensors results in different 3×3 sub-matrices becoming nonzero in $\boldsymbol{F}$ (3.24).

We will perform nonlinear timeseries simulations using Opal-RT's full AC power flow solver ePHASORSIM. We consider a simulation time step is 5 seconds (i.e., $\Delta = 5$ second, $K = 120$ timesteps, and $\tau = K\Delta = 600$ seconds for the simulation duration). Using an Intel Core i7-8565U CPU @ 1.80 GHz, it takes approximately 45 seconds to compute the operating parameter ranges with MATLAB, and 120 seconds to perform the nonlinear simulations in ePHASORsim.

3.5.3 DER Clusters for Voltage Stability

We first consider simulations of DERs arranged in the CFG χ_1, where there is a co-located DSP at node 57 and node 76, notably without any measurements sent between the DERs. Siting at node 57 and 76 is consistent with [56], where DERs are cited at a node with average voltage and a node with high voltage. Because the DSPs are co-located, $\mathcal{D} = \mathcal{S}$ and $d = s$. The incremental volt-var control proposed in [1] is implemented by populating the upper left $\frac{d}{2} \times \frac{s}{2}$ sub-block of $\bar{\boldsymbol{F}}$ with $\bar{\boldsymbol{F}}_{ii} = (1.98/y) * (2/\boldsymbol{X}_{ii})$ for $i = 1...s/2$ and $y = \frac{s}{2}$ and zero otherwise. This control policy was proved by authors in [1] to stable in the linear system sense for co-located CFGs. We simulate the system from 11:00am to 11:08am. In Fig. 3.4 we plot a voltage magnitude envelope to encompass the minimum and maximum of all network voltages, and overlay the example voltage trajectory of node 76 phase B. After the controllers turn on at $\tau = 60$ seconds, and the overvoltage is mitigated within 15 seconds (3 iterations), resulting in all network voltages arriving in the desired 5% ANSI range. This simulation validates that the method proposed in [1] is effective at regulating voltages when DSPs are co-located.

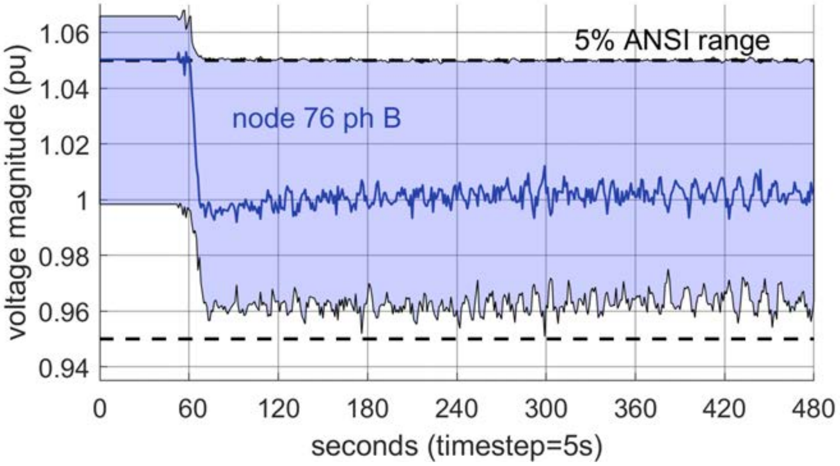

Figure 3.4: Voltage magnitude envelope capturing all 123NF voltages from simulation of CFG χ_1 with the control approach proposed in [1].

Not allowing DERs to share voltage measurements can limit the network-wide performance of the DER system. Transmitting voltage measurements to one or more DERs at other nodes could enable DERs to share power and respond directly to voltages at the most important network nodes. Further, the flexibility of allowing newly installed DERs to help out with existing DER clusters without needing to install a new sensor promotes modularity when deploying DER systems. Hence we next consider a CFG χ_2 where three DERs help track the nearby sensor at node 57 and another three DERs help track the sensor at node 76. See Fig. 3.5 for an illustration of CFG χ_2 marked in gold on the 123NF. To design DERs for this CFG, we extend the approach from [1] to allow for $i \neq j$ with $\bar{\boldsymbol{F}}_{ij} = (1.98/y) * (2/\boldsymbol{X}_{ij})$ for $i = 1...s/2, j = 1...d/2$. We simulate the system and plot the voltage magnitude envelope in Fig. 3.6. We observe voltage oscillations, accompanied by not only excessive actuation that may degrade the battery DERs, but also repetitive undervoltage violations.

We have demonstrated that the stability guarantees proved in [1] for co-located DSPs does not necessarily extend to CFGs where DSPs are not co-located. The voltage oscillations in Fig. 3.6 illustrates a danger in assuming the DSP arrangement and communication structure. This assumption is common to many works in volt-var control literature, including [12, 38,

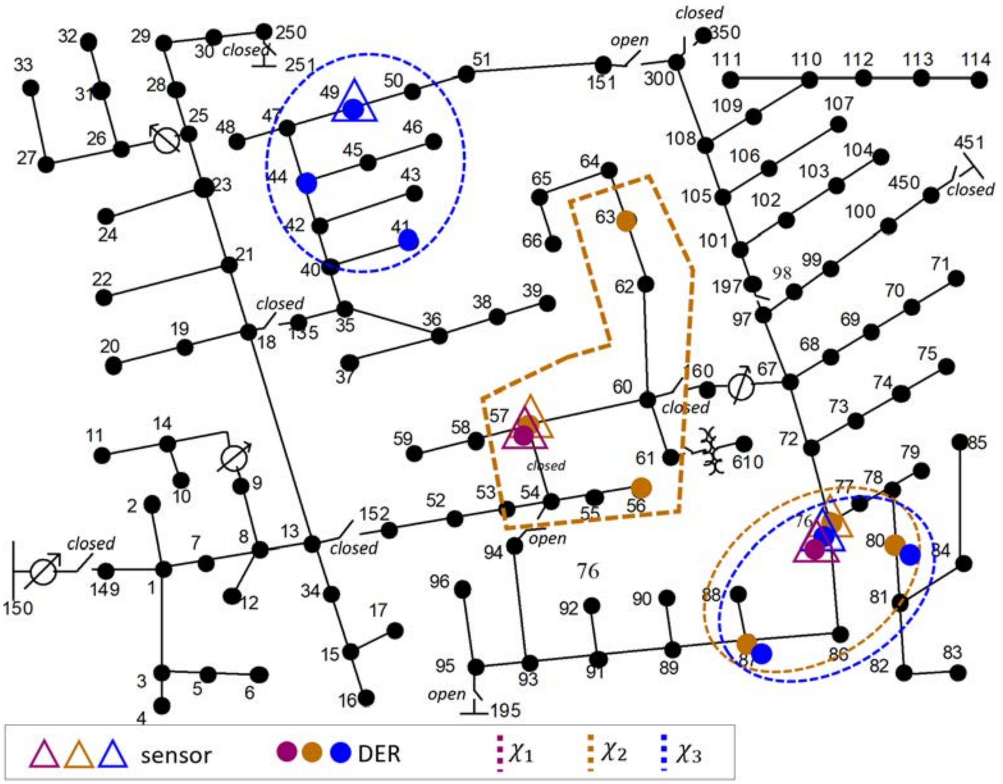

Figure 3.5: Diagram of DERs and sensors on the 123-node feeder. The CFG The CFG χ_1 is marked in pink, CFG χ_2 is marked in gold, and CFG χ_3 is in blue. Feeder is operated as a radial network.

53, 56]. As described, it can be beneficial to allow coordination among groups of DERs is the system can be stabilized.

Our modelling approach accommodates any externally defined communication structure, where any arrangement of sensors can share voltage phasor measurements with any set of DERs, allowing us to capture logistical or data privacy requirements. From CFG χ_2, we define the sensor nodes $\mathcal{S}$ and DER nodes $\mathcal{D}$ (3.1) for our model. Then the DER system model Σ^1 (3.23a) and the reduced system Σ^2 (3.28) is constructed according to section 3.2 and 3.2.5 using the given grid impedances $\bar{\boldsymbol{B}}$. For CFG χ_2, $d = 24$, $s = 12$, and $y = 120$. To compute operating parameter ranges, the stability region in the parameter space $\mathcal{F}$ is constructed according to section 3.5. The upper left $d/s \times s/2$ sub-block of $\bar{\boldsymbol{F}}$ is shown in Fig. 3.7 to how the CI requirements $\mathcal{I}_{\mathcal{W}}$ translates to the nonzero pattern of $\bar{\boldsymbol{F}}$. In Fig. 3.8, we plot $\mathcal{F}$, Chebyshev ball of $\mathcal{F}$, and the parameter range square in the space of two of the $y = 120$ parameters. We approximate the true stability region by fixing all except the plotted dimensions as the center of the Chebyshev ball, then evaluating the stability of the system (using Theorem 2) as the plotted dimensions are varied. We

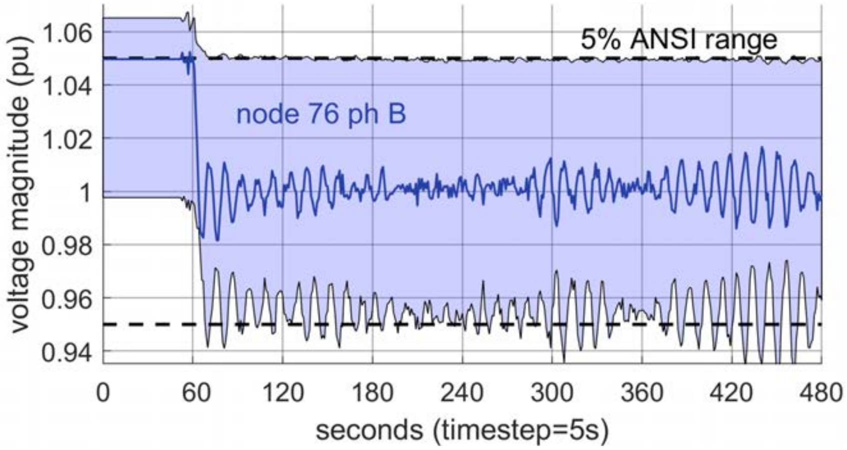

Figure 3.6: Voltage magnitude envelope from simulation of CFG χ_2 with the control approach from [1]

.

validate that the analytical stability polytope $\mathcal{F}$ is a subset of the true stability region. The Chebyshev ball radius is 0.0275 so the parameter range square width is $0.0275 \cdot \sqrt{2} = 0.0389$. Finally, we select the mid-way point of all parameter ranges (equivalent to the Chebyshev ball center) and simulate the closed-loop system. From the voltage envelope in Fig. 3.9, we observe stable tracking, resulting in achieving the voltage phasor references and all voltages arriving in the desired 5% ANSI range after about 300 seconds (60 iterations). Our proposed modeling approach effectively employs the externally defined communication structure to achieve voltage stability and the optimal grid state.

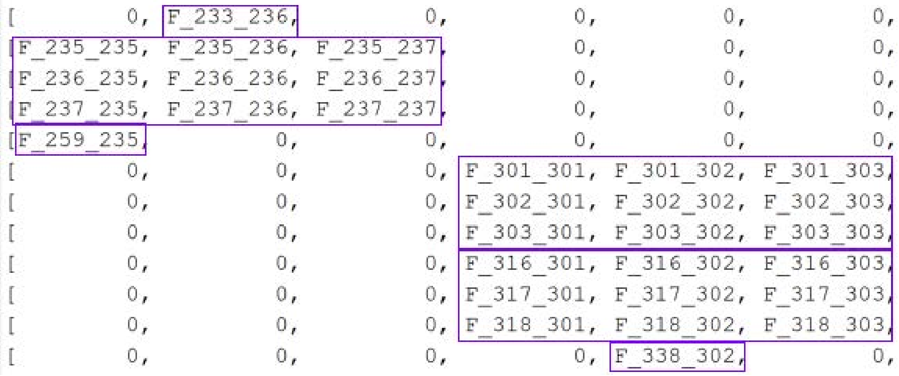

```
[        0, F_233_236,         0,         0,         0,         0,
[F_235_235, F_235_236, F_235_237,         0,         0,         0,
[F_236_235, F_236_236, F_236_237,         0,         0,         0,
[F_237_235, F_237_236, F_237_237,         0,         0,         0,
[F_259_235,         0,         0,         0,         0,         0,
[        0,         0,         0, F_301_301, F_301_302, F_301_303,
[        0,         0,         0, F_302_301, F_302_302, F_302_303,
[        0,         0,         0, F_303_301, F_303_302, F_303_303,
[        0,         0,         0, F_316_301, F_316_302, F_316_303,
[        0,         0,         0, F_317_301, F_317_302, F_317_303,
[        0,         0,         0, F_318_301, F_318_302, F_318_303,
[        0,         0,         0,         0, F_338_302,         0,
```

Figure 3.7: Upper left sub-block of operating parameter matrix $\bar{\boldsymbol{F}}$ for CFG χ_2. Purple outlines mark each DER acting on one or three phases.

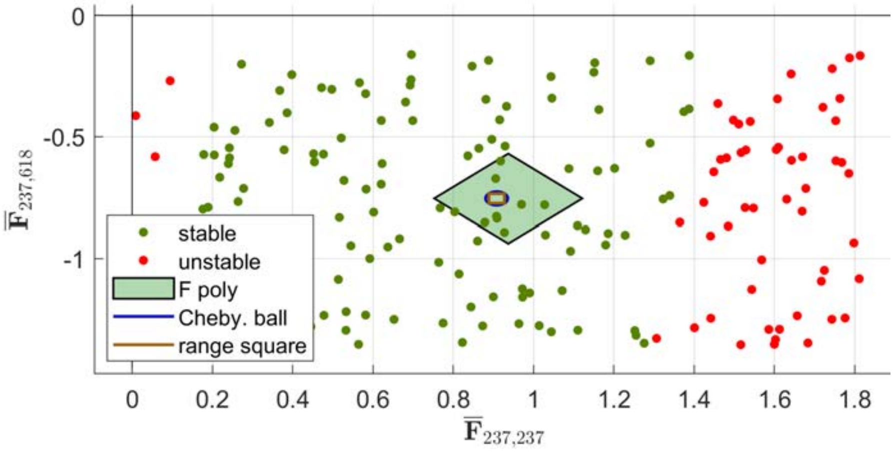

Figure 3.8: Space of stable and unstable operating parameters for CFG χ_2, including the analytical stability region $\mathcal{F}$ and the parameter range square.

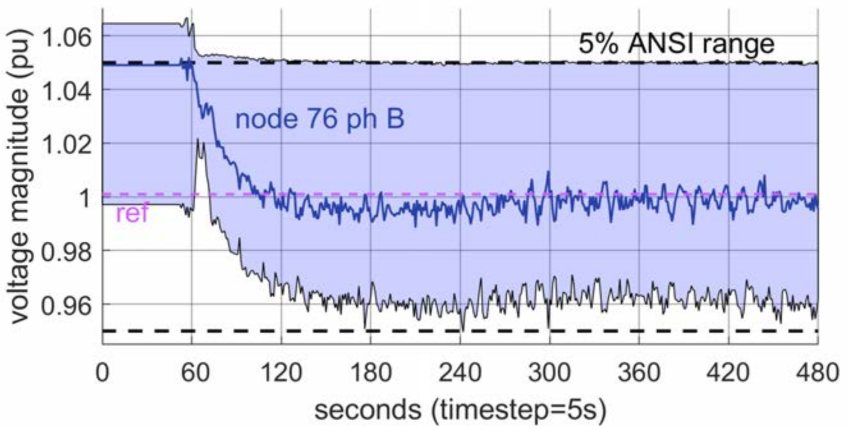

Figure 3.9: Voltage magnitude envelope from simulation of CFG χ_2 with the control approach proposed in section 3.5 of this thesis. The voltage phasor reference for node 76 phase B is included in purple.

3.5.4 Siting for Improved Performance

The settling time of the proposed control when applied to CFG χ_2 is 300 seconds (see Fig 3.9). On real grids, it may be important to mitigate overvoltages more quickly so as to better protect electrical equipment and achieve optimal operation faster. By siting the DSPs more effectively using siting Propositions 2 and 3, we seek to improve the voltage regulation performance while maintaining stability. We design CFG χ_3 and mark it in blue on the 123NF diagram of Fig. 3.5. The CFG is comprised of two clusters of DSPs that are placed more deeply (guidance of Proposition 2) and further apart (guidance of Proposition 3) than CFG χ_2. Specifically, the cluster around node 49 is deeper in the grid network since $|\boldsymbol{Z}_{49,49}| = 0.8$ is greater than $|\boldsymbol{Z}_{57,57}| = 0.5$. Furthermore, the cluster around node 49 is further apart from the node 76 cluster since $|\boldsymbol{Z}_{49,76}| = 0.26$ is less than $|\boldsymbol{Z}_{57,76}| = 0.5$. We then construct the original and reduced systems for CFG χ_3, resulting in $d = 24$, $s = 12$, and $y = 120$. In Fig. 3.10, we plot the stability region $\mathcal{F}$, Chebyshev ball of $\mathcal{F}$, and the parameter range square in the space of two of the $y = 120$ parameters. We also vary the plotted parameters and evaluate the system stability to approximate the true stability region and validate that $\mathcal{F}$ is a subset of it. We observe that the Chebyshev ball radius of $\mathcal{F}$ is 0.1037 (instead of 0.0275), which indicates that the stablity region $\mathcal{F}$ is more than three times larger when siting at CFG χ_3 than when siting at CFG χ_2. The parameter range square width for χ_3 is $0.1037 \cdot \sqrt{2} = 0.1466$.

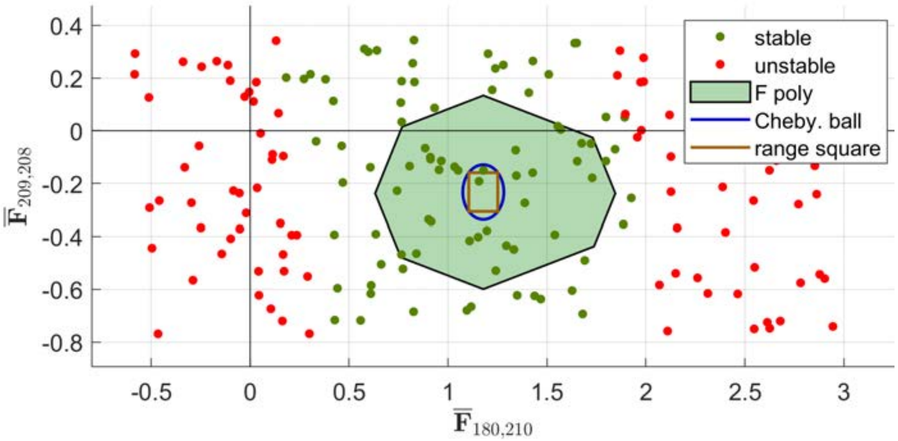

Figure 3.10: Space of stable and unstable operating parameters for CFG χ_3, including the analytical stability region $\mathcal{F}$ and the parameter range square.

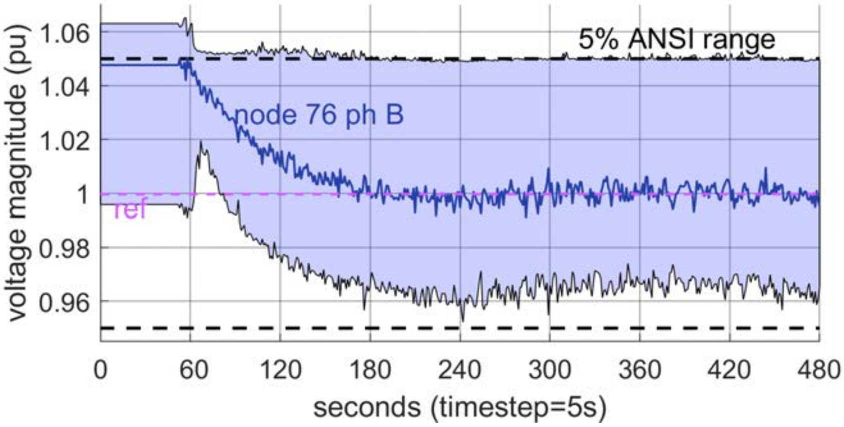

Figure 3.11: Voltage magnitude envelope from simulation of CFG χ_3 with the control approach proposed in section 3.5 of this thesis.

We select the mid-way point of all operating parameter ranges and simulate the closed-loop system operating in CFG χ_3. In Fig. 3.11, the voltage phasor references are achieved and all voltages arriving at appropriate voltage levels — as observed in the case of CFG χ_2. However, for this simulation the voltage phasors settle to their references after 210 seconds (42 controller iterations) compared to 300 seconds for CFG χ_2. Therefore, we have improved the voltage regulation speed by strategically siting our DSPs using Propositions 2 and 3.

In summary, we have demonstrated an approach to compute ranges of operating parameters for DER systems without co-located DSPs, and show how those ranges can be lengthened using strategic siting of DERs and sensors.

3.6 Designing Fixed Parameters of Stabilizing Controllers

3.6.1 Sampling Algorithm

As described in the previous section, the analytical stability region $\mathcal{F}$ can be conservative compared to the true stability region. As a result, even if $\mathcal{F}$ is empty, there may exist a solution to problem (P1), i.e. a stabilizing controller with the given CI requirements. In this section, we develop a sampling algorithm that is effective at finding many stabilizing $\bar{\boldsymbol{F}}$ matrices, which provide fixed sets of parameters. The benefit of this algorithm is twofold: first, among the stabilizing $\bar{\boldsymbol{F}}$s found, one can perform simulations using the stabilizing $\bar{\boldsymbol{F}}$ that has the greatest stability margin. Secondly, we can compare DER configurations based on the number of stabilizing controllers found and the associated stability margin. Though there are many viable approaches, we propose sampling each candidate nonzero element of

$\bar{\boldsymbol{F}}$ from a Gaussian distribution, where the mean and standard deviation are selected as functions of the grid impedances.

Suppose we are given a set of communication requirements $\mathcal{I}_W$ (3.45). For the purpose of designing candidate $\bar{\boldsymbol{F}}$ matrices, we assume each nonzero element of $\bar{\boldsymbol{F}}$ as an independent random variable. We sample each nonzero element of $\bar{\boldsymbol{F}}$ from a Gaussian distribution, then for each $\bar{\boldsymbol{F}}$ evaluate the spectral radius of the DER closed-loop system (3.30). We assess m candidate $\bar{\boldsymbol{F}}$ matrices, collected into set $\mathcal{F}$, to find the candidate that yields the best closed-loop performance. We measure performance using the system's spectral radius ρ, since the spectral radius indicates how quickly the closed-loop system converges to a steady state voltage. A formalization of the sampling problem is

Problem 2.

$$\begin{aligned} \textit{(P2)} \quad & \min_{\bar{\boldsymbol{F}}^k \in \mathcal{F}} \quad c = \rho(\boldsymbol{I} - \bar{\boldsymbol{B}}\bar{\boldsymbol{F}}^k) \\ & s.t. \quad [\bar{\boldsymbol{F}}^k]_{ij} = \begin{cases} \sim N(\mu_i, \bar{\sigma}) & \forall\ (i,j) \in \mathcal{I}_W \\ 0 & \forall\ (i,j) \notin \mathcal{I}_W \end{cases} \end{aligned} \tag{3.48}$$

If the Gaussian sample is negative, we re-sample from the same distribution. We impose that all gains are non-negative in order to apply the Gershgorin disc stability condition from Theorem 3, $\phi_i(\boldsymbol{H}) + \gamma_i(\boldsymbol{H}) < 2 \forall\ i = 1...s$, when designing the Gaussian μ parameter.

Gaussian mean parameter: We seek to define a starting point for sampling each nonzero element of $\bar{\boldsymbol{F}}$, which will be the mean of each gaussian distribution. The intuition is as follows: because every element of $\bar{\boldsymbol{H}}$ is comprised of the sum of products between elements of $\bar{\boldsymbol{B}}$ and $\bar{\boldsymbol{F}}$, if every element of $\bar{\boldsymbol{F}}$ is chosen to be the multiplicative inverse of an element of $\bar{\boldsymbol{B}}$, every product term will evaluate to about 1. Then to satisfy $\phi_i + \gamma_i < 2$, we require that each product term be scaled down by the number of terms appearing in $\phi_i + \gamma_i$.

To formalize this intuition, we expand $\bar{\boldsymbol{H}} = \bar{\boldsymbol{B}}\bar{\boldsymbol{F}}$ into

$$[BF]_{ij} = \sum_{l}^{2n} b_{i\ell} f_{\ell j}. \tag{3.49}$$

From matrix multiplication, the (ℓ, j) element of $\bar{\boldsymbol{F}}$, $\bar{\boldsymbol{F}}_{\ell j}$, only appears in the j^{th} column of $\bar{\boldsymbol{H}}$. Further, when it appears, it is always multiplied by an element in the ℓ^{th} column of $\bar{\boldsymbol{B}}$. we start by considering the simpler, special case where (1) the only nonzero element in $\bar{\boldsymbol{F}}$ is $\bar{\boldsymbol{F}}_{\ell j}$ and (2) $\bar{\boldsymbol{B}}_{i\ell} = c\ \forall\ i = 1...s$. If we select $\bar{\boldsymbol{F}}_{\ell j} = 1/|c|$, $\phi_i + \gamma_i < 2$ condition is $\bar{\boldsymbol{B}}_{i\ell}\bar{\boldsymbol{F}}_{\ell j} < 2$, which evaluates to $1 < 2$. In this case, the system is quite stable because the Gershgorin disc center is at $1 + 0j$ which is in the exact center of the stability ball $\mathcal{B}(1 + 0j, 1)$. If we relax (2), we would define

$$b^{max} := \max_{i=1...s} |\bar{\boldsymbol{B}}_{i\ell}| \tag{3.50}$$

Then we select $\bar{\boldsymbol{F}}_{\ell j} = 1/b^{max}$, which makes $\phi_i + \gamma_i < 2\ \forall\ i = 1...s$ hold. If we then relax (1), the number of terms in $\phi_i + \gamma_i < 2$ for each i is exactly equal to y, the number of nonzero elements in $\bar{\boldsymbol{F}}$. To maintain $\phi_i + \gamma_i < 2 \; \forall \; i = 1...s$, we scale down each term by y:

$$\mu(f_{\ell j}) = \frac{1}{y} \cdot \frac{1}{b^{max}} \tag{3.51}$$

Notice that μ is independent of j. That is, μ is the same for all elements in a given row of $\bar{\boldsymbol{F}}$. As such, this design yields s unique values of μ. The $1/y$ part of the computation of μ scales down μ for larger DER systems. This is reasonable because the stability condition $\phi_i + \gamma_i < 2$ considers the worst case in which all DER impacts push in the same direction, in which case it would be stable for each $\bar{\boldsymbol{F}}$ element to be small-valued. The selection of the Gaussian standard deviation enables us to explore less conservative controller gains.

Gaussian standard deviation parameter: In (P2), we have a fixed $\sigma = \bar{\sigma}$, and it is not straightforward to select. The selection of the parameter σ adjusts how widely to explore gain values. There is a trade-off between finding gain matrices that yield smaller spectral radii and finding stabilizing gain matrices at all. If σ is chosen to be too large, none or only a few stabilizing matrices may be found. Conversely, if σ is too small, many stabilizing matrices may be found but the matrices would be quite uniform resulting in similarly high spectral radii. Due to this stability-performance trade-off, we assume that the function from $c(\sigma)$ from P2 is strictly convex. Then we formalize determining a good σ as

Problem 3.

$$\textit{(P3)} \quad \bar{\sigma}^* = \arg\min_{\sigma} \quad c(\sigma) \tag{3.52}$$

Due to the non-convexity of $c(\sigma)$ with respect to σ, it is challenging to solve this problem directly. Instead, we approximate $c(\sigma)$ with $\hat{c}(\sigma)$, where we evaluate (P2) for a range of σ:

$$\hat{c}(\sigma) = c(\sigma)|_{\sigma \in [\sigma^{lb},...,\sigma^{ub}]} \tag{3.53}$$

If $\hat{c}(\sigma)$ is not strictly convex, we widen the range $[\sigma^{lb},...,\sigma^{ub}]$ until $\hat{c}(\sigma)$ becomes strictly convex. A diagram of $c(\sigma)$ and $\hat{c}(\sigma)$ for different ranges $[\sigma^{lb},...,\sigma^{ub}]$ is shown in Fig. 3.12. Once $\hat{c}(\sigma)$ is strictly convex, we select $\bar{\sigma} = \arg\min_{\sigma} \hat{c}(\sigma)$ for (P2) .

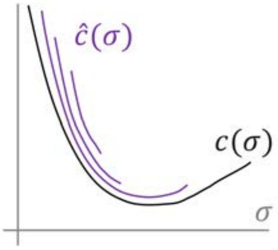

Figure 3.12: Selection of Gaussian parameter σ for sampling stabilizing gain matrices $\bar{\boldsymbol{F}}$.

The sampling algorithm described in this section allows us to evaluate a DER system (3.30) given the inputs of the grid impedances $\bar{\boldsymbol{B}}$, the DER and sensor locations ($\mathcal{N}_s$,$\mathcal{N}_d$), and CI requirements $\mathcal{I}_W$. The sampling algorithm samples a specified number of candidate gain matrices $\bar{\boldsymbol{F}}$, and records the spectral radius for each candidate. The algorithm has three outputs. The first is the number of stabilizing $\bar{\boldsymbol{F}}$ matrices found as a percentage of $m = 20$ candidates. The second output is the minimum spectral radius across the stabilizing $\bar{\boldsymbol{F}}$ matrices, which would be the optimal objective value c^* of (P2). The third output is the $\bar{\boldsymbol{F}}$ matrix associated with that minimum, which would be the optimal solution $\bar{\boldsymbol{F}}^*$ of (P2). These outputs are used in the next section to compare many DER systems on a given circuit.

3.6.2 Case Studies on Assessing the Stability of DER Configurations

In this section we illustrate how Propositions 1 to 4 can be used to inform the siting of DERs and sensors in realistic scenarios from academic literature and industry. Throughout this section, we consider groups of DER-sensor pairs (DSPs) acting on the IEEE 123-node feeder (123NF) [72]. We modify the 123NF by removing the voltage regulator transformer and the capacitors. Without these devices, underlying voltage issues are exacerbated, creating a more challenging voltage regulaton task for the DERs. We will evaluate many arrangements of DSPs, each of which is referred to as a *configuration* (CFG). For each configuration, we change the nodal locations of the DERs and sensors to enforce different structural requirements on $\bar{\boldsymbol{F}}$. A DSP is *co-located* if the DER and associated sensor are at the same node location, and *non-colocated* otherwise. Non co-located configurations can be valuable because they enable coordinating DERs at different nodes to track a voltage at another node. We measure *depth* of a DER or sensor at node i as the length of the unit's self-impedance path $|\boldsymbol{Z}_{ii}|$ (3.7) to the circuit substation. We focus on nine configurations that are denoted with χ_i for $i = 1, ..., 9$.

In what follows, we evaluate configurations by assessing stability of the linear model, and by simulating the control in simulations that solve nonlinear power flow. For the stability analysis, we apply the sampling algorithm developed in section 3.6 and evaluate the stability of the linear model (3.30) using Theorem 2 for different candidate controller gains. For each configuration, we compute the percent of stabilizing $\bar{\boldsymbol{F}}$ matrices found among the twenty candidate matrices, and the minimum spectral radius computed across the stabilizing $\bar{\boldsymbol{F}}$ matrices.

For all time series simulations, we include time-varying load data profiles that are constructed as follows: reported spot loads on the 123NF are replaced with aggregate secondwise time-varying net load data. The data is generated based on public commercial and residential loads and solar PV generation profiles from Southern California Edison during a typical summer day. At each node we scale the solar power profile to have 125% PV penetration. We consider 11:10am, the time of the highest overvoltage of about 1.06 per unit, for the five-minute simulations that follow. For our simulations, PV penetration is computed as the maximum (across the day) of the solar profile divided by to the maximum of the load profile. The DERs are considered to have unlimited capacity so that the control algorithm convergence and associated actuation effort can be observed. For each configuration, we select the stabilizing $\bar{\boldsymbol{F}}$ matrix associated with the minimum spectral radius, and simulate the controlled system as a quasi-static-time-series (see Chapter 2 section 2.2). For the simulations, we use Opal-RT's nonlinear power flow software ePHASORsim, where the time-step of each simulation iteration is five seconds. The voltage phasor targets for each DER controller are computed by solving an optimal power flow problem (see Chapter 2 section 2.3) with an optimization objective of reducing real and reactive power actuation by the controlled DERs. The performance evaluation criteria is (i) the integrated actuation summed across all DERs, (ii) the integration of all voltage violations outside the 5% range across all nodes of the network, and (iii) the maximum settling time across all performance nodes.

Scenario 1

As described in section 3.1, academia and industry have patterns for the siting of DERs, but may not analyze the how the siting affects DER system stability or simulation performance. Some authors of distributed OPF approaches [55,56,66] and incremental volt-var approaches [1, 12, 13] site DERs evenly throughout a feeder. Planning teams at utilities may approve request for DERs that are deep in the feeder [37] because they have a greater power-voltage sensitivity, or impact on the voltage per unit of actuation (see Chapter 2 section 2.1.5). Finally, the siting decision may be influenced by the deployment trends of DER programs, which could favor clustering DERs in a similar part of the feeder out of convenience.

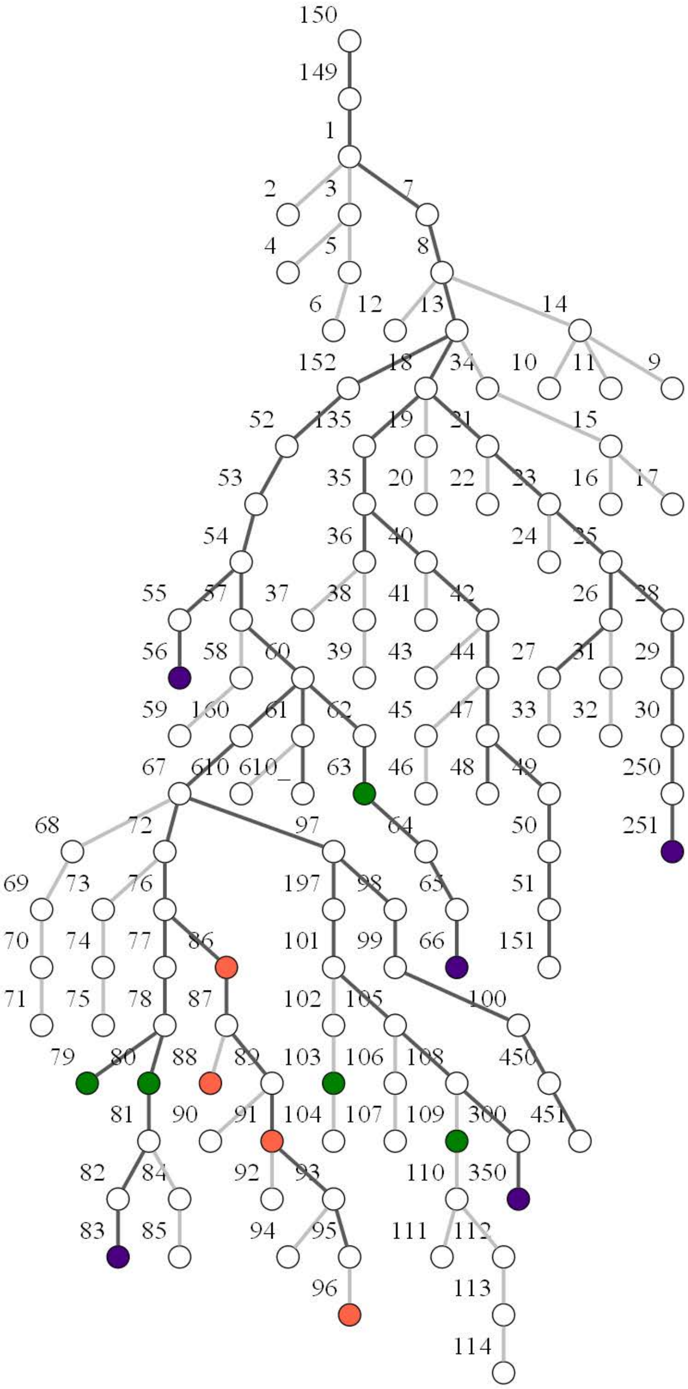

Figure 3.13: Case study scenario 1 for assessing the stability of DER configurations. Configurations of co-located DSPs are shown in green (CFG χ_1), indigo (CFG χ_2), and orange (CFG χ_3) are marked on the 123NF network graph. Light network edges indicate single or two-phase power lines.

Table 3.2: Scenario 1: table of metrics comparing the performance three DER configurations (CFG). The linear analysis samples twenty sets of controller parameters to find stabilizing sets with the lowest minimum spectral radius for use in the nonlinear simulation. From the nonlinear simulation, the sum of actuation of all DERs, the sum of voltage violations outside the 5% ANSI range across all nodes of the network, and the maximum settling time across all performance nodes are tabulated.

	Linear Analysis		Nonlinear Simulation		
CFG	**percent stable (%)**	**min spectral radius**	**integrated voltage violation (pu)**	**sum of integrated actuation (kWh)**	**settling time (sec)**
χ_1	75	0.944	0.0093	-335.9	93
χ_2	45	0.994	0.0030	-292.0	116
χ_3	15	0.969	0.0025	-332.2	187

In light of the DER siting observed in literature and industry, we compare three configurations, each comprised of five co-located DSPs. In χ_1, DERs are placed at edge nodes that are evenly spaced throughout the feeder as done by authors in [1, 12, 13]. In χ_2, DERs are sited deeply in a clustered part of the grid, which could be done on real grids out of convenience when quickly deploying newDER programs. In χ_3, which is our proposed configuration, we site the DERs using using Propositions 2 and 3. Fig. 3.13 has the 123NF network marked with the three configurations.

For configurations χ_1,χ_2, and χ_3 the voltage magnitudes, voltage phase angle tracking error, and DER power outputs from the nonlinear simulations are plotted in Fig 3.14. Table 3.2 compares the metrics from the linear system stability analysis and the nonlinear system simulations. We observe for all simulations that the phasor target converges quickly and smoothly due to the controller design described in section 3.6. Because the phasor targets converge, we observe in the voltage envelopes of Fig 3.14 tht voltages at *all* nodes of the network converge to optimal values in the 5% ANSI range. The regulation of voltages at all nodes via tracking at only a subset of nodes is core to the PBC framework (see 2.3). The minimum spectral radius metric indicates that the sampling algorithm is most effective at stabilizing CFG 1, which is reasonable since the DERs are not placed as deeply (Proposition 2) in the network as the DERs in CFG2 and CFG3. However, considering the nonlinear simulations, we observe the worst voltage violations with CFG 1, which may be due to having fewer DERs placed deeply in the feeder where there are typically more severe voltage issues. Configuration 2 has the least actuation, which is reasonable because the clustering of the DERs may allow them to benefit from each others' voltage regulation efforts. Finally, CFG 3 exhibits the best voltage regulation by having the DERs placed deeply to achieve greater voltage sensitivity (Proposition 2), and by being spread out the

DERs achieve better stability (Proposition 3).

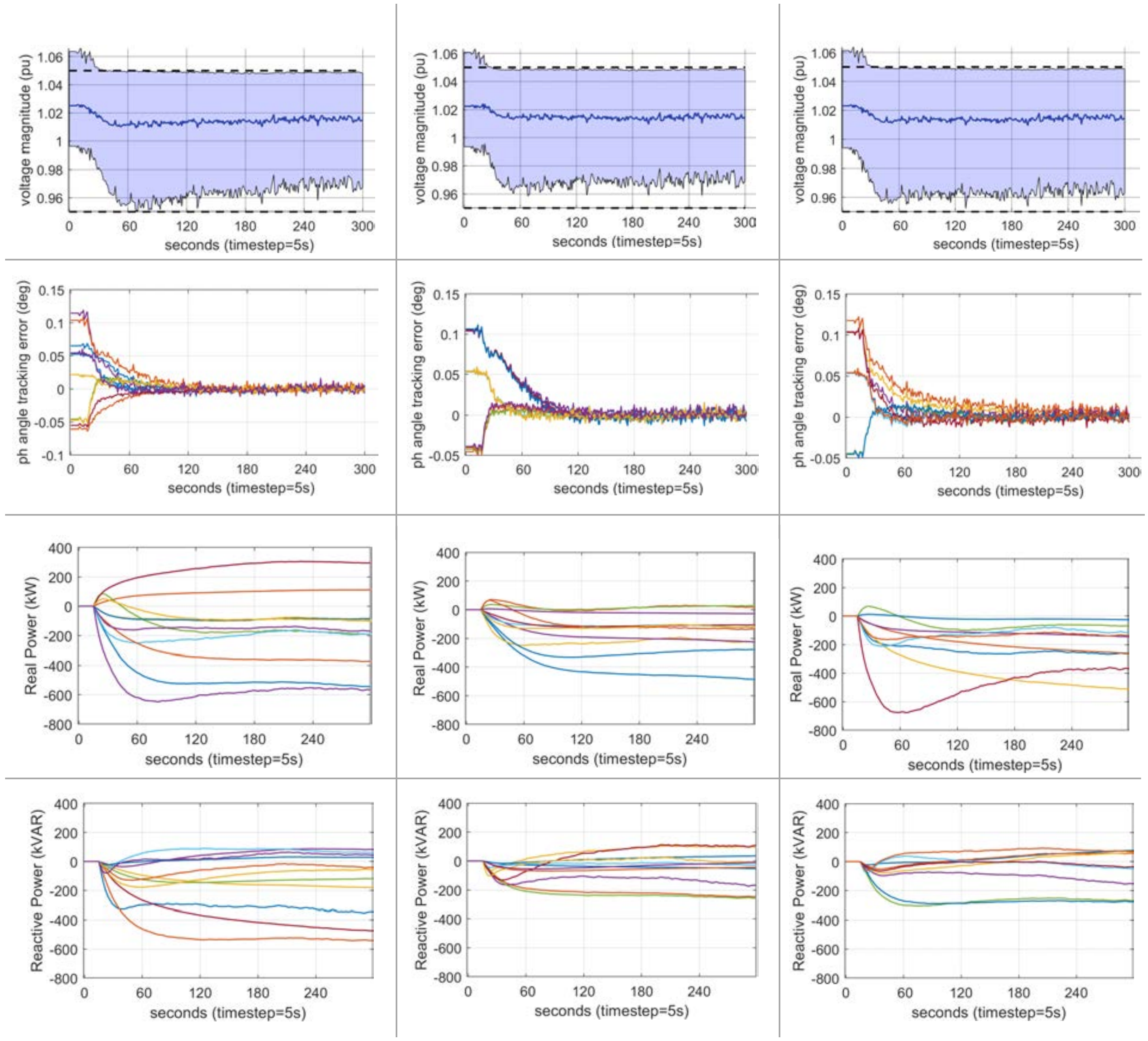

Figure 3.14: Scenario 1: plots comparing the nonlinear simulation performance of three DER configurations. The simulation runs from 11:00am to 11:05am with 125% PV penetration. ***Left column:*** performance of CFG χ_1. ***Middle column:*** performance of CFG χ_2.***Right column:*** performance of CFG χ_3.

Scenario 2

Next, we consider the value in coordinating multiple DERs to track a single phasor target. Suppose we have one sensor installed on a distribution grid and wish to site one or more DERs to track the phasor at the sensor node. From Proposition 4, we would prefer to *co-locate*

Table 3.3: Scenario 2: table of metrics comparing the performance of DER configurations (CFG).

	Linear Analysis		Nonlinear Simulation		
CFG	**percent stable (%)**	**min spectral radius**	**integrated voltage violation (pu)**	**sum of integrated actuation (kWh)**	**settling time (sec)**
χ_4	95	0.655	0.0035	-133.3	117
χ_5	100	0.587	0.0044	-143.5	64

a single DER of large capacity to achieve both stability and controller efficiency. However, suppose we have the option to install a group of small-capacity DER at many nearby nodes whose capacities sum to the large-capacity value. In literature about microgrids and medium-voltage grids, authors may assume these two scenarios yield similar technical performance because the grid network constraints between the DERs are assumed to have a negligible impact on DER performance [73, 74]. In this scenario we investigate this question about the equivalence of DER aggregations using the medium-voltage 123NF. We consider two configurations, both with a single sensor in the middle of the feeder at node 76. For χ_4, there is a single DER co-located with the sensor. For χ_5, there are ten DERs nearby (node 70,73,80,87,90,92,95,67,160, and 61) both upstream and downstream of the sensor node. Each of these DERs helps to track sensor node (node 76) voltage phasor.

For configurations χ_4 and χ_5, the DER power outputs from the nonlinear simulations are plotted in Fig 3.15. Table 3.3 compares the metrics from the linear system stability analysis and the nonlinear system simulations. From the stability analysis, we observe that CFG χ_4, the CFG with only one DER, has slightly higher spectral radius, which highlights how having many DERs creates more of a stability concern than when you have one DER due to the impedances between the DERs. Even still, both CFGs have very low spectral radii (far below a value of one, which is the boundary of stability), resulting in fast convergence to the voltage phasor. Configuration χ_4 also has less voltage violations, and requires slightly less total actuation, which may be due to the simplicity of controlling one DER over multiple. However, CFG χ_5 has faster settling time, because multiple DERs are recruited at once to respond to voltage issues. Overall, we have demonstrated that multiple DERs tracking the phasor are about as effective as a single large-capacity DER, but the multiple-DER case has slightly more concern for stability and slightly more total actuation incurred across the controlled devices.

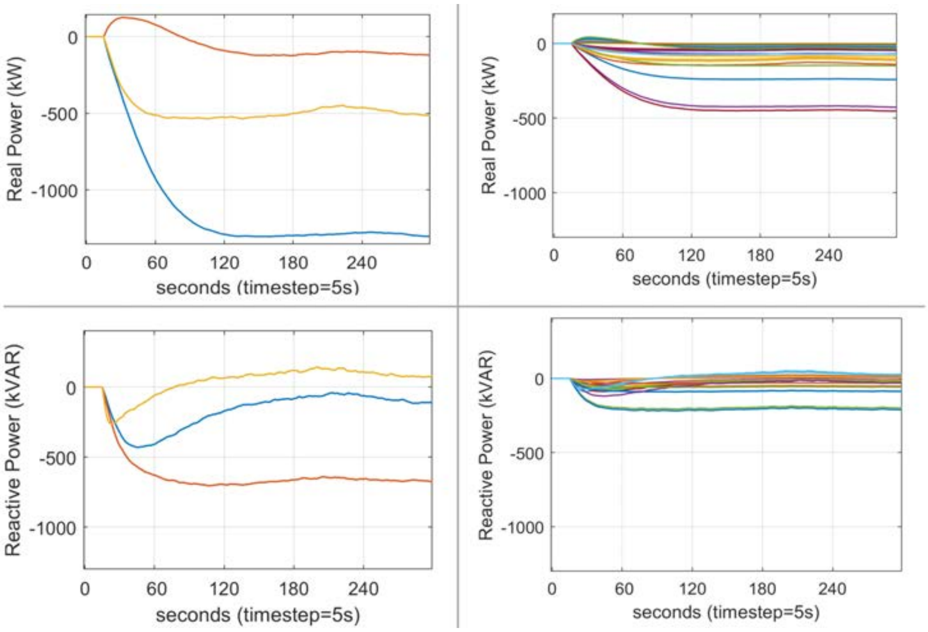

Figure 3.15: Scenario 2: plots comparing the nonlinear simulation performance of two DER configurations. The simulation runs from 11:00am to 11:05am with 125% PV penetration. ***Left column:*** performance of CFG χ_4. ***Right column:*** performance of CFG χ_5.

Visual Tool for Assessing Stability

In Scenario 1 and 2, we compared a few configurations of DSPs to illustrate how designers can use Propositions 1 to 4 to update their intuitions about siting DERs. Distribution planning literature often proposes iterative approaches to evaluate many DSP configurations [75, 76]. These approaches randomly select candidate DER or sensor locations, solve power flow, then based on the results decide whether to place the unit or not. Further, this literature sometimes illustrates the power flow results with a capacity map, were the nodes of a the graph network are colored to indicate how much resource capacity can be added until a voltage or thermal violation occurs [77]. Inspired by the illustrative aspect of these distribution planning approaches, we develop a visual tool to iteratively evaluate many configurations. Notably, instead of solving power flow once to evaluate each configuration, we iteratively assess the stability of candidate configurations, which does not require a power flow solver and determines the dynamic evolution of the system in response to voltage violations. Because our tool does not simulate any system, it does not make claims about time-series performance, DER capacity limit violations, or power loss. Our tool focuses in investigating the stability of proposed control configurations, whose results can then inform the setup of a simulation if needed.

The tool evaluates each configuration using the associated minimum spectral radius (c^* of (P2)), which is a measure of the system's stability margin. Recall from Remark 1 that a greater stability margin results in faster convergence to the voltage phasor, which provides disturbance rejection and optimality benefits. After defining a vector $\boldsymbol{c}$ that collects this spectral radius across all m configurations of interest, we define percentile ranges for generating the heatmap color gradient.

$$c^{min} = \min_i(c_i) \; \forall \; i = 1, ..., m \tag{3.54a}$$

$$\text{heatmap bin values:} \quad \ell_i = \frac{c_i - c^{min}}{1 - c^{min}} \; \forall \; i = 1, ..., m \tag{3.54b}$$

$$\text{heatmap colors:} \quad \begin{cases} \text{yellow} & \ell_i < 33\% \\ \text{yellow-orange} & 33 \leq \ell_i < 66\% \\ \text{orange} & 66 \leq \ell_i < 100\% \\ \text{red} & \ell_i \geq 100\% \end{cases} \tag{3.54c}$$

Scenario 3

Next we consider a scenario in which there are many existing DSPs. This is a realistic situation given that many real distribution grids already have DERs installed with some control logic. Given a desired location for the next sensor, for example at a location that commonly experiences overvoltages, we are interested in determining where future DERs should be sited to track that sensor. Propositions 2 to 4 can be used to identify relatively more stable nodes to site DERs, but the Propositions do not provide definitive answers about what specific node locations are stable. For example, a DER may be geographically close to a sensor but electrically far away (measured by the common-node impedance). The DER customer may agree to track the sensor, but doing so may make the system unstable or prohibitively inefficient in terms of actuation effort (see Proposition 4). Therefore, we design the non-colocated placement process (NPP) to evaluate configurations in a directed manner.

The NPP can be applied to a grid with any number of existing DSPs. We choose a candidate performance node location, then iterate through all other empty node in the feeder, fixing each as the associated candidate actuator node. We generate a heatmap of the network, where a node's color (3.54c) indicates the stability of the configuration created by appending the candidate DSP to the existing set of DSPs. Next, we place a DER on an orange or yellow node to become part of the core configuration, and this chosen node is colored indigo on subsequent heatmaps. We repeat this process until the desired number of DSPs have been placed. The NPP produces a configuration of DSPs in locations that yield fast voltage convergence, and the step-by-step heatmaps show how the choice of sensor ocations and DERs affect the stability of placing the next DSP.

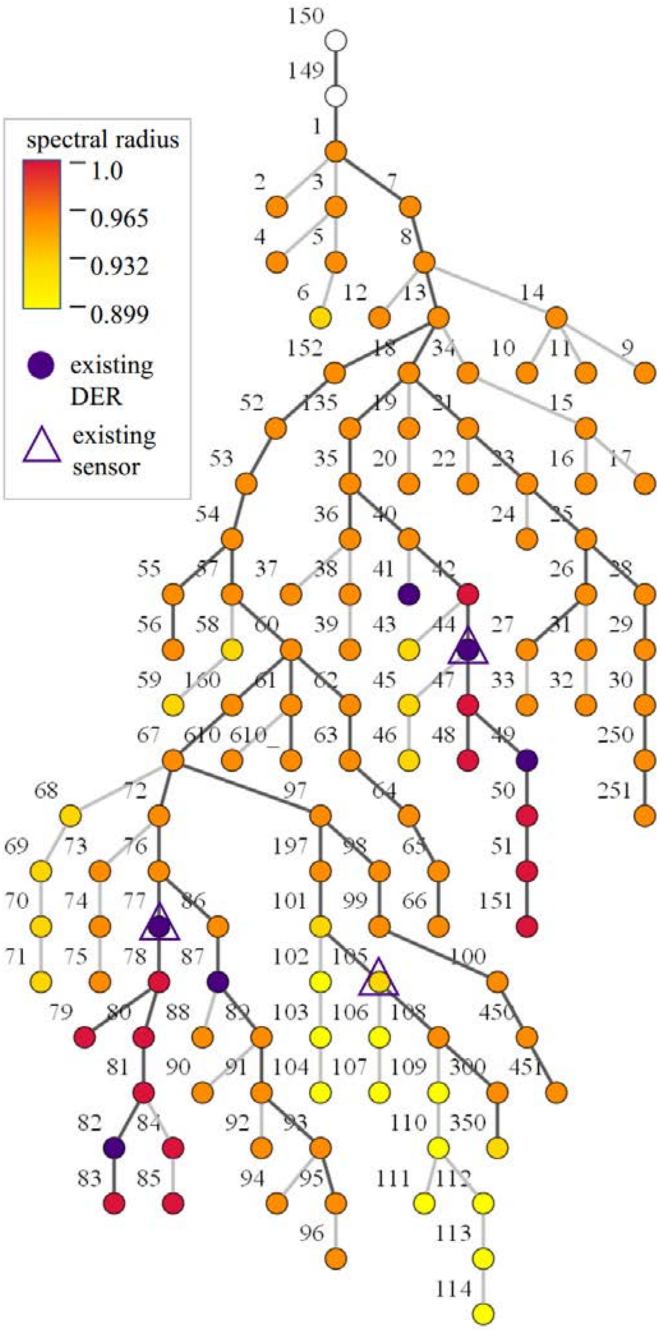

Figure 3.16: Scenario 3: Heatmap of the 123NF generated by the Non-colocated placement process (NPP). The heatmap colors indicate stable locations for adding a DER to the existing DER system that tracks the voltage phasor at node 105.

We demonstrate the NPP on a feeder where there are two neighborhoods of existing

DSPs. Specifically, χ_6 is comprised of a group of DERs located at node 41, 44, and 49 that track the voltage phasor at node 44, and a group of DERs at node 77, 82, and 87 that track the voltage phasor at node 77. In total, there is an existing configuration of six DSPs. We run the NPP to find good locations for placing a seventh DSP, which will start a new group of DERs for tracking the voltage phasor at the chosen performance node (node 105, marked with indigo triangle). As shown in the heatmap of Fig. 3.16, locations near node 105 are light yellow, indicating greater stability margin, while locations near the existing two neighborhoods of DERs are more orange and red. Notably, we have a color gradient indicating differing DER performance for placements between performance node 105 and performance node 44. Predicting the location of this color transition would have been challenging to determine without the heatmap.

We validate the heatmap colors of Fig. 3.16 by placing a DSP at each of the following nodes: 78 (red), 68, 62, 24 (orange), and 104 (yellow). For example, the CFG with DER at node 62 (orange) has greater settling time (261s) more integrated voltage violations (0.010), and incurs slightly more integrated actuation (-14.1) than the CFG with DER at node 104 (yellow), which has 89s, 0.007, -13.9 for these metrics respectively.

Circuit Topologies

From Propositions 1 to 4, one may wish to generalize the topological properties of radial circuit networks that enable well-performing DER systems. For example, authors in [44] placed a co-located DSP operating under incremental volt-var at every circuit node and considered different circuit topologies. They show that networks with line topologies (few branches and many deep nodes) have a smaller stable operating region than more radial topologies. We note that because every node had a co-located DER, the *effective grid network* (EGN) - defined as the set of impedances that are captured by the reduced system model (3.30) - was coincident with whole grid network. However, when a configuration does not have a DSP at every node, by Proposition 3, only the impedance paths to the substation and common-node impedances comprise the EGN and therefore determine the performance of the DER system. Moreover, DERs could be placed at the same depth on two different-sized circuits, resulting in the same EGN. This concept implies that Assumption 2 can be loosened. That is, only the impedances of the EGN, not those of all network nodes, need to be known for controller design. This notion is useful since many grid operators have inaccurate network model information, and topologies changes due to a switch opening or outage may change the grid network without changing the EGN. Then in considering only the EGN, Proposition 3 suggests that the EGN should have many branches to reduce the total of the common-node impedances, which is consistent with the findings in [44].

Scenario 4

We know from Proposition 3 and the previous scenarios that placing new DSPs should be placed electrically distant from existing ones. However, the distance metric is not purely based on the graph connectivity of the network. Complex impedance properties matter, specifically the R/X ratio and mutual impedances in the network paths. The impact of mutual impedance on effective DER power set-point control has been relatively unexplored in the literature apart from a few works such as [16] and [54]. In what follows we illustrate the value of considering these complex impedance properties on different branches of a distribution grid.

First we define the R/X ratio and phase ratio for three-phase grids using the impedance 3 × 3 block of a power grid line segment.

$$\begin{bmatrix} \boldsymbol{R}_{11} & \boldsymbol{R}_{12} & \boldsymbol{R}_{13} \\ \boldsymbol{R}_{21} & \boldsymbol{R}_{22} & \boldsymbol{R}_{23} \\ \boldsymbol{R}_{31} & \boldsymbol{R}_{32} & \boldsymbol{R}_{33} \end{bmatrix} + j \begin{bmatrix} \boldsymbol{X}_{11} & \boldsymbol{X}_{12} & \boldsymbol{X}_{13} \\ \boldsymbol{X}_{21} & \boldsymbol{X}_{22} & \boldsymbol{X}_{23} \\ \boldsymbol{X}_{31} & \boldsymbol{X}_{32} & \boldsymbol{X}_{33} \end{bmatrix} \tag{3.55}$$

We express the R/X of a three-phase network line as

$$d_1 := \frac{\boldsymbol{R}_{11}}{\boldsymbol{X}_{11}}, \quad d_2 := \frac{\boldsymbol{R}_{22}}{\boldsymbol{X}_{22}}, \quad d_3 := \frac{\boldsymbol{R}_{33}}{\boldsymbol{X}_{33}} \tag{3.56}$$

The R/X ratio is important for controlling DER systems because high R/X ratio causes cross interactions between real power and reactive power and voltage magnitude and phase angle [49]. On the 123NF, the R/X ratios of lines vary from 0.42 to 0.86.

We express the phase ratio of a three-phase network line as

$$g_1 := \frac{\boldsymbol{X}_{12} + \boldsymbol{X}_{13}}{\boldsymbol{X}_{11}}, \qquad g_4 := \frac{\boldsymbol{R}_{12} + \boldsymbol{R}_{13}}{\boldsymbol{R}_{11}} \tag{3.57a}$$

$$g_2 := \frac{\boldsymbol{X}_{23} + \boldsymbol{X}_{12}}{\boldsymbol{X}_{22}}, \qquad g_5 := \frac{\boldsymbol{R}_{23} + \boldsymbol{R}_{12}}{\boldsymbol{R}_{22}} \tag{3.57b}$$

$$g_3 := \frac{\boldsymbol{X}_{13} + \boldsymbol{X}_{23}}{\boldsymbol{X}_{33}}, \qquad g_6 := \frac{\boldsymbol{R}_{13} + \boldsymbol{R}_{23}}{\boldsymbol{R}_{33}} \tag{3.57c}$$

The phase ratio is important for controlling DER systems because high mutual impedances ($\boldsymbol{R}_{ij} + j\boldsymbol{X}_{ij}$ for $i \neq j$) relative to the self impedances causes cross interaction between phases. For example, high mutual impedances cause power injections on phase A to have a significant effect on phase B and C voltages. On the 123NF, the phase ratios of lines vary from 0.62 to 0.81.

The co-located placement process (CPP) illustrates good places to place the next co-located DSP to maintain stability of the DER system. It iterates through every empty node in the feeder, fixing each as a candidate co-located DSP. We assess the stability of appending the candidate to the existing configuration, and generate a heatmap on the network with colors (3.54c) indicating the stability of the different configurations.

We define two configurations of co-located DSPs, χ_7 = [node_8, node_53, node_57, node_66] and χ_8 =[node_8, node_53, node_57, node_74]. Note that χ_7 has an DSP on branch [node_62 node_66], which has the highest three-phase R/X ratios and phase ratios. Specifically, we consider the R/X ratio and phase ratio content of each node on the branches of interest. For a node of interest i, we consider a scalar metric for R/X ratio of the impedance $\boldsymbol{Z}_{ii}$ as $\max_j d_j$ for $j = 1, 2, 3$, where the maximum operator captures single-phase impedances. Similarly, we consider a scalar metric for phase ratio as $\max_j g_j$ for $j = 1, ..., 6$.

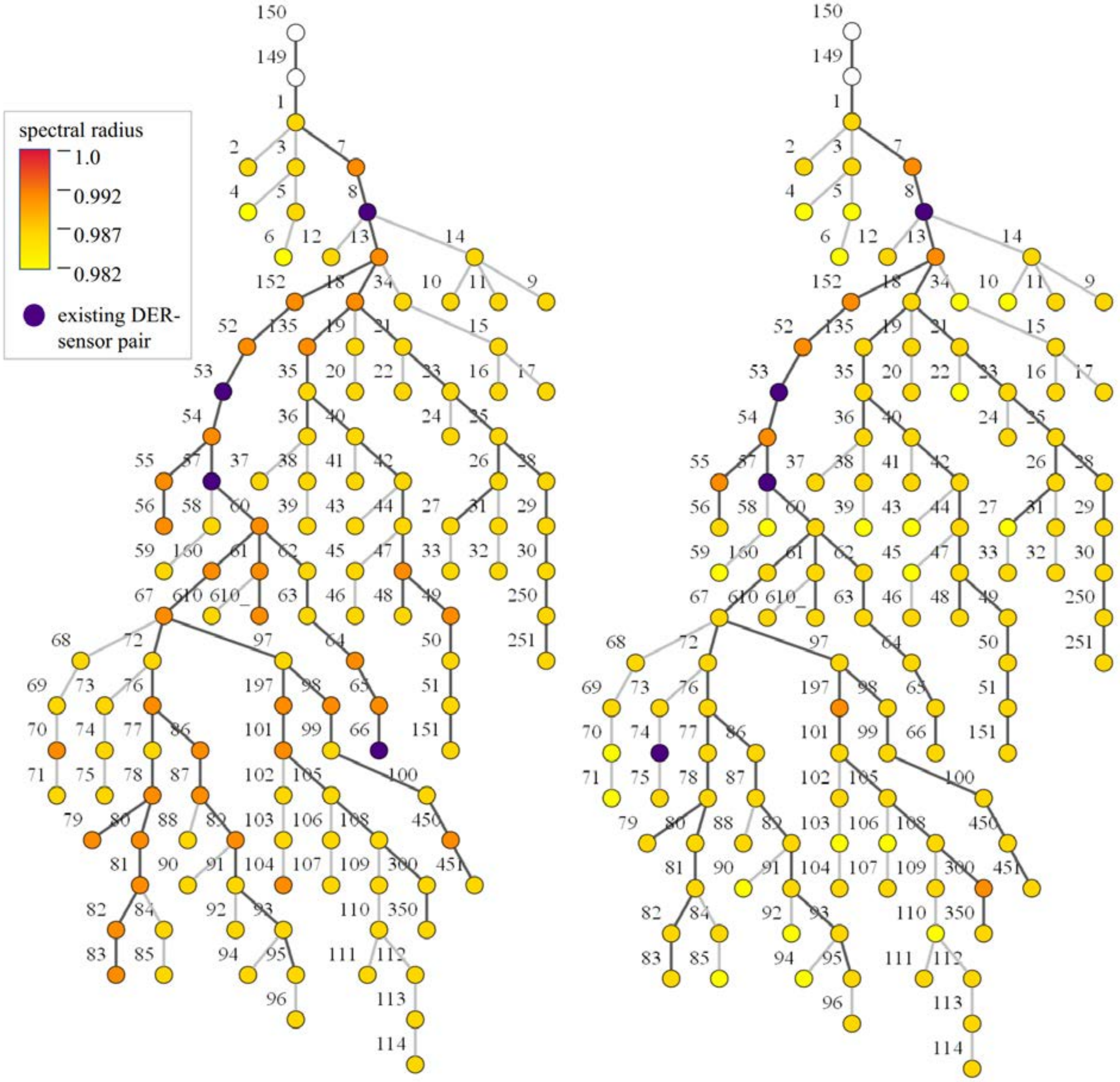

Figure 3.17: Scenario 4: Heatmaps generated by the co-located placement process (CPP) that indicate stable locations for placing another co-located DSP. ***Left:*** Cfg χ_7 is marked in purple, which includes a DER on a network branch with high R/X and phase ratio. ***Right:*** Cfg χ_8 is marked in purple, which includes a DER on a network branch with low R/X and phase ratio.

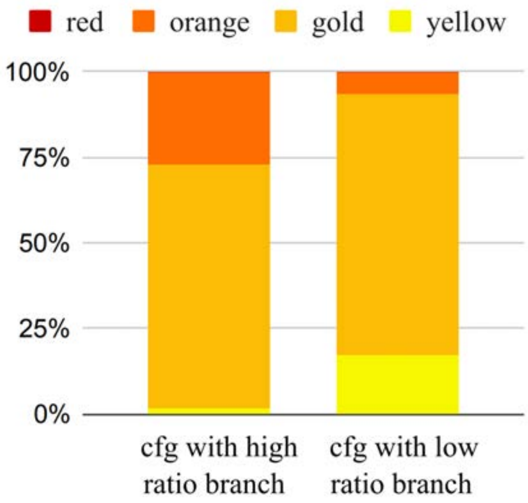

Figure 3.18: Scenario 4: Comparison of heatmap color gradients from Fig. 3.17 heatmaps. Cfg χ_7 (left bar graph) color gradient indicates greater spectral radii across network nodes than the color gradient for CFG χ_8 (right bar graph).

We place χ_7 on the 123NF, then run the CPP to find good locations for the fifth DSP, which is illustrated by the tool's heatmap in the left pane of Fig. 3.17. We do the same treatment to χ_8, producing the heatmap in the right pane of Fig. 3.17. In Fig. 3.18, we tabulate the number of nodes of each color across the two CPP runs. The greater percentage of dark orange nodes indicates that placing co-located DSPs on high R/X and phase ratio branches makes it difficult to place subsequent co-located DSPs.

3.7 Conclusion

In this chapter, we developed a novel dynamical system model for DERs operating under phasor-based control. The feedback controllers provide an immediate response to disturbances, and the model derivation is consistent with other power-voltage control laws in literature, making it easy to adapt to other control approaches. The main novelty of the model is its direct incorporation of any externally defined communication infrastructure, which allows DERs to unlock coordination benefits while adhering to privacy or ownership constraints. Then, stability conditions on the dynamical system model enabled us to establish stability guarantees in terms of the siting of DERs. Next, we described how computing controller parameters given communication infrastructure is generally a challenging problem to solve when formulated as an optimization. Yet by applying the Gershgorin disc theorem we were able to analytically compute stability regions instead. Further, we developed a reliable heuristic algorithm for sampling stabilizing controllers that was demonstrated to be effective in several realistic scenarios of the 123-node IEEE test feeder. Finally, the visual tool developed is accessible and intuitive to grid operators, enabling a more direct transfer of these modeling and stability analysis techniques to industry.

Chapter 4

Reachability Analysis for Ride-Through Disturbance Events

This chapter is based on the paper 'Reachability Analysis for Controlling DERs to Mitigate Disturbances in Distribution Grids' [78], written in collaboration with Alexandra von Meier.

In contrast to Chapter 3 where DER control was considered in the context of a normal voltage operating state, in this chapter we consider the abnormal scenario, where there is a significant voltage excursion outside of the safe range. To prevent the abnormal voltages from causing equipment damage, DERs are required to disconnect within a few seconds. In this problem, system stability, where voltages are guaranteed to to converge to nominal values, is insufficient. Instead, we are interested in assessing whether DER power set-point control can recover *within a given time limit* despite the presence of high voltage variability. We model this variability as a bounded polytope using real distribution phasor measurement unit (D-PMU) data. Then we compute backwards reachable sets which define the worst-case voltage excursion that the DER volt-var can recover from before the DERs must disconnect. We validate our design and analysis with simulations on a 4-bus, IEEE 13-bus, and IEEE 123-bus unbalanced networks.

4.1 Introduction

As more distributed energy resources (DERs) are installed on distribution grids, utilities have observed increased variability in power flows and voltages. To prevent equipment damage, there is increasing need to design advanced controls, especially for solar inverters, to mitigate this variability. We are interested in an abnormal voltage scenario, where DERs are required to provide real and reactive power support for several seconds (ride-through) before they and other devices must trip, as prescribed by the national IEEE 1547-2018 standard and California's Rule 21 [79]. Therefore, it is important to ensure that DERs can be effective at mitigating disturbances within an externally specified time limit.

Droop volt-var control (DVVC) is a standard DER function for mitigating voltage issues. But literature has shown that volt-var control can introduce risks of voltage oscillations [46], and [13] proves that volt-var control cannot maintain voltages in acceptable ranges. One growing class of alternatives is incremental volt-var control [1, 13, 80], where the reactive power injection is adjusted using the provisioning at the previous time. This control law removes steady-state error, thereby driving voltages into the 5% ANSI range to promote safe grid operation.

To analyze the convergence of an incremental volt-var control law, authors [1,13,80] may assume small-signal fluctuations in voltage due to grid phenomena not under our DER control to be zero. It is assumed that across the few seconds of ride-through those fluctuations do not significantly affect the control response. However, cloud transients can cause ramps in PV generation on the order of 15% per second at a particular location [81] and could change secondary voltages by up to 0.35V per second [82]. Furthermore, motor loads and legacy voltage regulation can impart significant step changes in voltage magnitude. Therefore, in this critical ride-through period it is important to guarantee against the worst-case impact of these fluctuations with our DER control response.

To the authors' knowledge, modeling distribution grid small-signal fluctuations on second-wise or faster timescales is rare in the literature. This may be due to the lack of accurate sensors with a high sample rate. The newer technology of D-PMUs provides ultra-precise, synchronized measurements of voltage (and optionally current) magnitudes and phase angles on distribution grids [49]. Many D-PMU data applications are for event detection, but the machine learning classification methods used do not explicitly develop a model of the event behavior [83]. Work of [84] does model a time-dependent disturbance ellipse using PMU measurements. The difference between our applications is that the authors examine transmission grids and only use the disturbance model to visualize the disturbance bounds. In this work, we use the PMU data for a small-signal voltage fluctuation model that we then use to compute disturbance rejection guarantees.

Reachability analysis has been extensively studied in control theory literature since the 1960s [85]. Backward reachable sets describe the set of system initial states that guarantee a dynamic system's trajectory will land in a specified target set within a certain time frame. To the authors' knowledge, computing these sets to attain guarantees around disturbance rejection in distribution grids is novel. Our goal is to compute the largest abnormal voltage conditions that our controller can overcome within the trip time limits, despite small-signal voltage fluctuations occurring each second. A conceptual diagram of the problem is in Fig. 4.1.

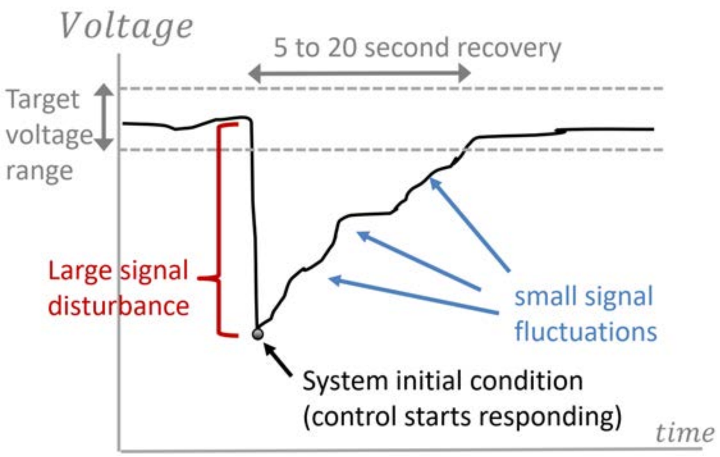

Figure 4.1: Conceptual diagram of the voltage disturbance rejection problem on distribution grids. Following a large-signal voltage disturbance, DER controllers are tasked with driving the voltage into the safe range within a few seconds despite small-signal voltage fluctuations.

4.2 Problem Formulation

4.2.1 Large-signal Disturbance

Suppose a large-signal disturbance shifts the voltage to an abnormal operating state outside the 5% ANSI range. We are interested in any disturbance where the voltage recovers slowly, on the order of several seconds. For example, in a Fault Induced Delayed Voltage Recovery (FIDVR) event, a fault [86] or [87] could cause a 20% to 55% voltage sag that stalls the motor loads, thereby lengthening the voltage recovery time. In what follows, we focus on system trajectories whose initial conditions are the operating point directly after the large-signal disturbance occurs.

4.2.2 Power Flow Linearization

In the next two subsections, we develop a closed-loop quasi-steady state dynamical system model that is comprised of the algebraic DistFlow equations and an incremental volt-var control law. This model is consistent with the works [1, 13, 80], with the extension of not setting the fluctuations from uncontrollable sources to zero. Consider the Distflow branch equation [27] for a single-phase radial network

$$|V_i|^2 - |V_j|^2 = 2(r_{ij}P_{ij} + x_{ij}Q_{ij}) + (r_{ij}^2 + x_{ij}^2)\frac{(P_{ij}^2 + Q_{ij}^2)}{|V_i|^2}, \tag{4.1}$$

which approximates the relationship between voltage magnitudes V_i, V_j and power flow $P_{ij} + \mathbf{j}Q_{ij}$ from node i to node j with complex impedance $r_{ij} + \mathbf{j}x_{ij}$.

We linearize (4.1) about a nominal voltage of $1p.u.$ by dropping the square term. Next, let v_i be the squared voltage magnitude, p_i the net real power, q_i the net reactive power at node i, and define vectors $\boldsymbol{v} = [v_1, v_2, ...v_n]^\top$, $\boldsymbol{p} = [p_1, p_2, ...p_n]^\top$, $\boldsymbol{q} = [q_1, q_2, ...q_n]^\top$,$\boldsymbol{v}_0 = [v_0, v_0, ...v_0]^\top$ on a network with n nodes. Here $\boldsymbol{v}_0$ refers to the substation node which is constant at $1p.u.$. As done in [1, 38], we define the time step k to be sufficiently large for the dynamics from inverters, lines, and loads to settle to steady state before new power injections are updated. The algebraic relationship between nodal power injections and squared nodal voltages at all nodes for time steps k and $k+1$ becomes

$$\boldsymbol{v}[k] = Rp[k] + Xq[k] + v_0 \tag{4.2a}$$

$$\boldsymbol{v}[k+1] = Rp[k+1] + Xq[k+1] + v_0 \tag{4.2b}$$

where the entries of matrices R and X at the i^{th} row and j^{th} column are given by

$$\boldsymbol{R}_{ij} = 2 \sum_{(h,k)\in\mathcal{P}_i\cap\mathcal{P}_j} r_{hk} \tag{4.3a}$$

$$\boldsymbol{X}_{ij} = 2 \sum_{(h,k)\in\mathcal{P}_i\cap\mathcal{P}_j} x_{hk}. \tag{4.3b}$$

Set $\mathcal{P}_i$ is the unique set of lines (or path) connecting node i back to the substation node. Net nodal powers are given by

$$\boldsymbol{q}[k] = \boldsymbol{q}^{inv}[k] + \boldsymbol{q}^{other}[k] \tag{4.4}$$

where $\boldsymbol{q}^{inv}$ are DER-inverter combination reactive power set-point commands, and $\boldsymbol{q}^{other}$ are reactive power injections from sources not under our control.

4.2.3 Model with Incremental Volt-Var Control

We employ incremental volt-var control for computing inverter reactive power set-points q^{inv} with

$$\boldsymbol{q}^{inv}[k+1] = \boldsymbol{q}^{inv}[k] - \boldsymbol{G}(\boldsymbol{v}[k] - \boldsymbol{v}^{ref}) \tag{4.5}$$

Note that equation (4.5) differs from the related DVVC law, $\boldsymbol{q}^{inv}[k+1] = -\boldsymbol{G}(\boldsymbol{v}[k] - \boldsymbol{v}^{ref}[k])$. The tracking error is mapped to the next *change in actuation* command, in contrast to how DVVC maps the tracking error to the next *actuation* command.

We subtract equation (4.2a) from (4.2b), giving

$$\boldsymbol{v}[k+1] = \boldsymbol{v}[k] + \boldsymbol{R}(\boldsymbol{p}[k+1] - \boldsymbol{p}[k]) + \boldsymbol{X}(\boldsymbol{q}[k+1] - \boldsymbol{q}[k]). \tag{4.6}$$

Next, consider the update equation (4.4) at time step $k+1$, then substitute these two equations into (4.6), giving

$$\boldsymbol{v}[k+1] = \boldsymbol{v}[k] + \boldsymbol{X}(\boldsymbol{q}^{inv}[k+1] - \boldsymbol{q}^{inv}[k]) + \boldsymbol{w}[k] \tag{4.7}$$

where $w[k] \coloneqq \boldsymbol{R}(\boldsymbol{p}[k+1]-\boldsymbol{p}_k)+\boldsymbol{X}(\boldsymbol{q}^{other}[k+1]-\boldsymbol{q}^{other}[k])$. Then we substitute the control law (4.5), giving

$$\boldsymbol{v}[k+1] = \boldsymbol{v}[k] - \boldsymbol{X}\boldsymbol{G}(\boldsymbol{v}[k] - \boldsymbol{v}^{ref}) \tag{4.8}$$

Finally, we subtract the constant reference voltage $\boldsymbol{v}^{ref}$ from both sides and let $\boldsymbol{e}[k] = \boldsymbol{v}[k] - \boldsymbol{v}^{ref}$. Our closed-loop system is

$$\boldsymbol{e}[k+1] = (I - \boldsymbol{X}\boldsymbol{G})\boldsymbol{e}[k] + \boldsymbol{w}[k] \tag{4.9}$$

Note that if all nodes of the network are being tracked, $\boldsymbol{v}^{ref}$ must be a feasible power flow solution. If only a subset of the network nodes are being tracked, $\boldsymbol{v}^{ref}$ can be assigned to the nominal vector of ones.

Author [1] proves in their Theorem 3.1 that for the system (4.9), $\boldsymbol{v} \to \boldsymbol{v}^{ref}$ iff

$$0 \prec \boldsymbol{G} \prec 2\boldsymbol{X}^{-1}.. \tag{4.10}$$

where the symbol '$\succ$' denotes a positive definite matrix. For intuition, condition (4.10) applied to the one-dimensional case (single phase grid with one DER) establishes that the integrator gain should be $0 < g < \frac{2}{x}$, which is positive but not too large. Condition (4.10) also implies that for any state and input independent term $\boldsymbol{w}[k]$, $\boldsymbol{v} \to \boldsymbol{v}^{ref}$. Therefore a major benefit from the reachability analysis is to determine whether $\boldsymbol{v} \to \boldsymbol{v}^{ref}$ *soon enough*, before the DER devices are required to trip (disconnect).

4.2.4 Small-signal Fluctuation Modeling

Small-signal voltage fluctuations in distribution grids can be due to solar PV, loads, and legacy voltage regulation devices. These fluctuations are captured by $\boldsymbol{w}[k]$ which is defined in (4.9) as changes in system voltages between time steps. In this section we develop a polytope

$$\mathcal{W} = \{\boldsymbol{w} \in \mathcal{R}^n \mid w_{lb}\mathbf{1} \leq \boldsymbol{w} \leq w_{ub}\mathbf{1}\} \tag{4.11}$$

such that $\boldsymbol{w}[k] \in \mathcal{W}$. We assume the fluctuation at each node is independent across nodes, which is realistic given the variety of phenomena that could occur on different nodes of medium-voltage networks. Thus w_{lb} amd w_{ub} are scalars that are repeated n times to define $\mathcal{W}$ (4.11).

We determine polytope bounds w_{lb} and w_{ub} using distribution PMU voltage data from the Sunshine dataset of the ARPA-E initiative NI4AI [2]. The dataset consists of six D-PMUs measuring voltage phasors, current phasors, and frequency across two circuits. The circuits are 12.47 kV (line-to-line) in a sunny region of the United States, both having buildings and a community-scale PV array. Circuit B has a capacitor bank. The data was sampled at 120 frames per second over four years (2015-2020) with some offline time during scheduled outages or reconfigurations.

From this data, we extract groups of 16 three-minute voltage magnitude timeseries snippets. Across five times of day (TODs) (hour 10, 12, 14 16, 18), two months (January and

June), and two circuits (circuits A and B), we have 320 snippets. For each snippet we interpolate the data to be second-wise, then compute the variance and derivative of each snippet. Then we find the maximum variance var_{max}, maximum negative derivative μ_{lb}, and maximum positive derivative μ_{ub} among each group of 16, and record them in Table 4.1.

Table 4.1: Distribution phasor measurement unit (D-PMU) data from the Sunshine dataset of the ARPA-E initiative NI4AI [2]. The data is collected at five different times of day (TOD), during a summer and winter month, on two different distribution circuits. The variance, maximum change, and minimum change in voltage magnitude is determined for each data snippet.

	Circuit A, June 2016			**Circuit B, June 2016**		
TOD	$\boldsymbol{var_{max}}$	$\boldsymbol{\mu_{lb}}$	$\boldsymbol{\mu_{ub}}$	$\boldsymbol{var_{max}}$	$\boldsymbol{\mu_{lb}}$	$\boldsymbol{\mu_{ub}}$
multiply	$\times e^{-8}$	$\times e^{-4}$	$\times e^{-4}$	$\times e^{-8}$	$\times e^{-4}$	$\times e^{-4}$
10:00	36.0	-26.4	30.7	69.7	-27.4	24.6
12:00	29.7	-49.1	34.3	27.0	-76.5	39.4
14:00	54.0	-30.2	33.0	49.0	30.2	23.3
16:00	34.8	-27.8	32.3	36.0	-34.7	37.9
18:00	47.6	-43.5	25.2	64.0	-29.0	27.0
	Circuit A, Jan 2017			**Circuit B, Dec 2015**		
TOD	$\boldsymbol{var_{max}}$	$\boldsymbol{\mu_{lb}}$	$\boldsymbol{\mu_{ub}}$	$\boldsymbol{var_{max}}$	$\boldsymbol{\mu_{lb}}$	$\boldsymbol{\mu_{ub}}$
multiply	$\times e^{-8}$	$\times e^{-4}$	$\times e^{-4}$	$\times e^{-8}$	$\times e^{-4}$	$\times e^{-4}$
10:00	69.7	-61.8	32.7	20.7	-30.5	30.5
12:00	44.2	-27.4	38.3	23.5	-24.4	22.3
14:00	29.2	-24.9	26.9	34.2	-37.4	39.0
16:00	33.1	-18.6	19.8	23.5	-43.0	34.7
18:00	15.2	-18	16.7	19.8	-108.7	36.2

Next we determine w_{lb} and w_{ub}. We believe a multimodal Gaussian distribution has an appropriate probability density function (PDF) for w. Distribution grid voltage changes tend to occur as small fluctuations (mode around mean of zero), step changes down (mode μ_{lb} at some negative value), or step changes up (mode μ_{ub} at some positive value) due to discrete device actions. By defining

$$w_{lb} = -2\sqrt{v\tilde{a}r_{max}} + \tilde{\mu}_{lb} \tag{4.12a}$$

$$w_{ub} = +2\sqrt{v\tilde{a}r_{max}} + \tilde{\mu}_{ub}, \tag{4.12b}$$

our polytope bounds capture 95% of the Guassian-modeled voltage fluctuation values. $v\tilde{a}r_{max}$, $\tilde{\mu}_{lb}$, and $\tilde{\mu}_{ub}$ are the largest (by magnitude) of the var_{max}, μ_{lb}, and μ_{ub} entries in Table 4.1, respectively. The multimodal Gaussian PDF along with the polytope range is conceptually illustrated in Fig. 4.2. This worst-case polytope is conservatively large since the short ride-through period is unlikely to exhibit the largest voltage shifts observed across the PMU dataset.

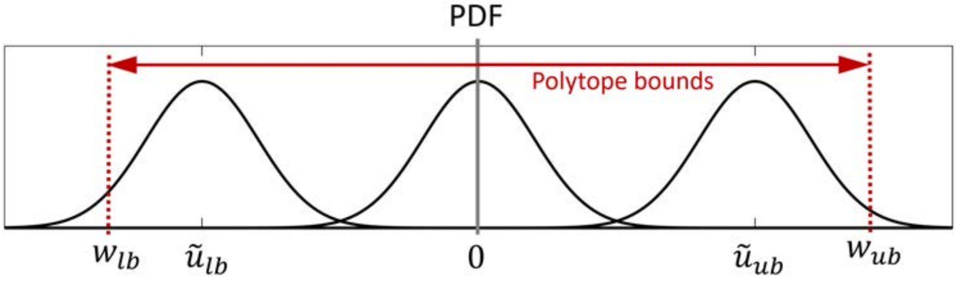

Figure 4.2: Multimodal Gaussian probability distribution function (PDF) fitted to the Distribution phasor measurement unit (D-PMU) dataset. The function is used to determine that define the disturbance polytope $\mathcal{W}$.

4.2.5 Robust Backwards Reachable Set Computation

This subsection's methods are from [88, Chapter 10]. The reachability analysis methods make use of our system (4.9) being affine, where the affine term $w[k]$ is independent of the state and inputs.

Definition 1. *The N-step robust backwards reachable set (RBRS) of the system* (4.9) *is*

$$\mathcal{K}_N := \{\boldsymbol{e}[0] \in E \mid \forall k = 0...N-1,\ \boldsymbol{e}[k] \in E \text{ and } \boldsymbol{e}[N] \in E_f,\ \forall w[k] \in \mathcal{W}\} \quad (4.13)$$

where E is the set of admissible states, E_f is the target set, and $\mathcal{W}$ is the small-signal fluctuations poytope set. To compute $\mathcal{K}_N$, we need to compute predecessor sets. A predecessor set of set S is the set of states from which the system evolves to be in S in one time step. The predecessor set for the linear autonomous system in (4.9) is

$$Pre(S, \mathcal{W}) = \{\boldsymbol{e} \mid \boldsymbol{H}((I - \boldsymbol{XG})e + \boldsymbol{w}) \leq \boldsymbol{h}\} \quad (4.14)$$

where $\boldsymbol{H}$ and $\boldsymbol{h}$ define the set $S = \{\boldsymbol{e} \mid \boldsymbol{He} \leq \boldsymbol{h}\}$. Algorithm 1 computes $\mathcal{K}_N$ using predecessor sets.

We seek to allow w to lie anywhere in $\mathcal{W}$ when computing the RBRS. One option is to set $\boldsymbol{w} = \bar{\boldsymbol{w}}^j$ in (4.14), where $\bar{\boldsymbol{w}}^j$ is the j^{th} vertex of the polytope $\mathcal{W}$. Then one would compute $\mathcal{K}_N(\bar{\boldsymbol{w}}_{\boldsymbol{j}})\ \forall \bar{\boldsymbol{w}}_{\boldsymbol{j}} \in \mathcal{V}_{\mathcal{W}}$ where $\mathcal{V}_{\mathcal{W}}$ contains all vertices of $\mathcal{W}$. The intersection of these reachable sets is the RBRS that approximates $\boldsymbol{w} \in \mathcal{W}$. The drawback of this method is that it requires computing $|\mathcal{V}_{\mathcal{W}}|$ reachable sets, where $|.|$ denotes cardinality. $|\mathcal{V}_{\mathcal{W}}|$ grows in a combinatorial way as $|\boldsymbol{w}|$ increases.

```
Algorithm 1: Compute the N-step RBRS, $\mathcal{K}_N$
  Input: $E$, $E_f$. $N$
  Output: $\mathcal{K}_N(S)$
$i = 0$, $\mathcal{K}_0(S) = E_f$;
repeat
    $i = i + 1$;
    $\mathcal{K}_i(S) = Pre(\mathcal{K}_{i-1}(S)) \cap E$
until $i > N$;
```

The second option, which we pursue, captures the effect of all $\bar{\boldsymbol{w}}^j \in \mathcal{V}_{\mathcal{W}}$ on the set S by solving the linear program

$$\min_{\boldsymbol{w}\in\mathcal{W}} (\boldsymbol{h}_i - \boldsymbol{H}_i\boldsymbol{w}) \tag{4.15}$$

where $\boldsymbol{H}_i$ is the i^{th} row of $\boldsymbol{H}$. We concatenate each linear program's optimal objective into a vector $\tilde{\boldsymbol{h}}$, which replaces $(\boldsymbol{h} - \boldsymbol{H}\boldsymbol{w})$ in the $Pre(S)$ computation. Therefore, each $Pre(S)$ computation requires the solving of a new set of linear programs, but notably only a single RBRS is computed to capture the $\boldsymbol{w} \in W$. This route scales better than the aforementioned method because fewer set intersections are needed.

4.3 Case Studies

In this section, we compute reachable sets to assess the voltage recovery by DERs for three different distribution grid circuits. Disturbance polytope $\mathcal{W}$ bounds were found by computing $v\tilde{a}r_{max} = 69.72e^{-8}$, $\tilde{\mu}_{lb} = -0.01087$, and $\tilde{\mu}_{ub} = 0.00394$ from the PMU dataset described in section II.D. Then from (4.12b) we have $w_{lb} = -0.0125\ Vpu$ and $w_{ub} = 0.0056\ Vpu$, each repeated n times to define $\mathcal{W}$.

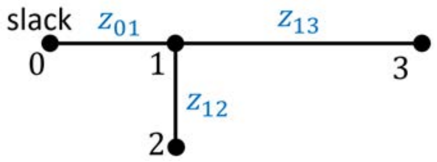

Figure 4.3: Network graph of 4-node radial circuit (4NF). The figure has single lines, but the experiments model the circuit as three-phase unbalanced with significant mutual impedances. The circuit self impedances satisfy the relationships $z_{01} = z_{12}$, and $z_{13} = 2z_{01}$.

4.3.1 4-Bus Network

We created a 4-node unbalanced circuit (4NF) that is defined in Fig. 4.3. It has mutual impedances equal to 30% of the self impedances, and the single phase equivalent impedances r_{01} and x_{01} are in Table 4.2. We specify E as 0.7 to 1.2 Vpu on all $n = 3$ nodes and the target set E_f as the ANSI 5% range. We placed incremental volt-var controllers at nodes 2 and 3. We compute $\mathcal{K}_{10}$ using the base case of parameters in Table 4.2. To execute Algorithm 1, we use MATLAB CVX to solve the linear programs and MATLAB's Multi-Parametric Toolbox (MPT) toolbox to compute set intersections and projections. The resulting 10-step RBRS in Fig. 4.5 has E, E_f, and $\mathcal{K}_{10}$ shifted up by 1 Vpu to convert from errors to voltage values.

Table 4.2: Base case parameters used to simulate the DER control and compute the RBRS on the 4-node test circuit (4NF).

Parameter	**Matrix Value**	**Units (not p.u.)**
reactance of line 01, x_{01}	0.1776 pu	0.0852 ohms
reactance of line 01, r_{01}	0.0864 pu	0.0415 ohms
control gain for DER at node 2, f_2	0.8	100 kW for deviating by quarter of 5% ANSI range
control gain for DER at node 3, f_3	0.5	62.5 kW for deviating by quarter of 5% ANSI range
polytope lower bound, w_{lb}	-0.0125 pu	30 volts
polytope upper bound, w_{ub}	0.0056 pu	13.44 volts

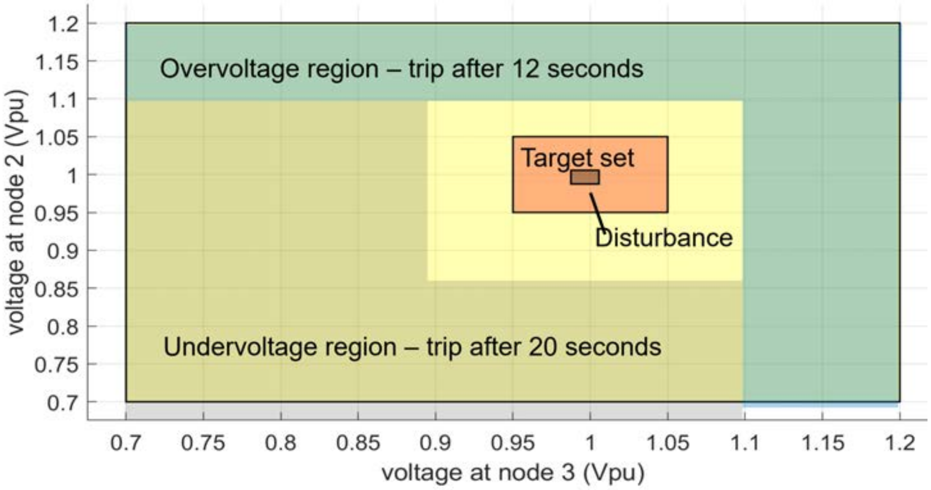

Figure 4.4: Plot of safe target set V_f, bounds of second-wise disturbance $\boldsymbol{w}[k]$, and Rule 21 trip regions. The DER control must drive node 2 and 3 voltages into the target set. If the voltage is in a trip region after 12 or 20 seconds, the DERs have failed and must trip.

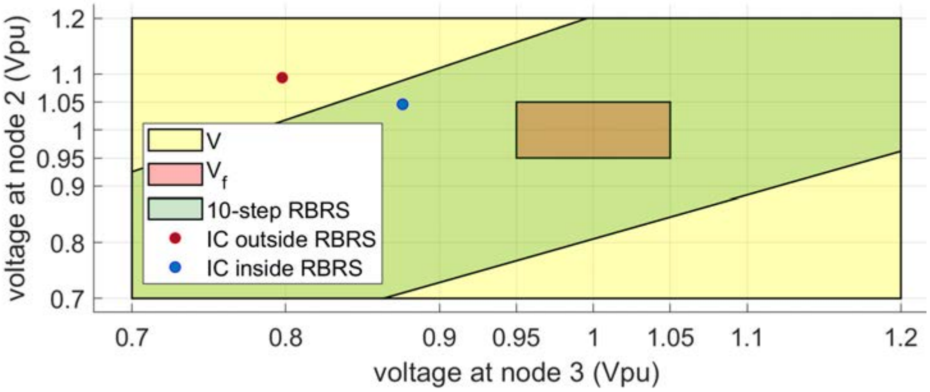

Figure 4.5: Ten-step robust backward reachable set (RBRS) computed using base parameters (Table 4.2) on the 4NF. An initial condition (IC) inside the RBRS (green) is guaranteed to stay within set V (yellow) for all time steps, and is guaranteed to be within safe set V_f (red) within 10 time steps.

We compare our system's control performance to California's Rule 21 [79], which has shorter time limits than that of the national IEEE 1547 standard. Note that in Fig. 4.4 E_f, which the RBRS guarantees the voltages enter within 10 seconds, is well inside the Rule 21 tripping regions, ensuring that the voltage will recover before the inverters are required to trip.

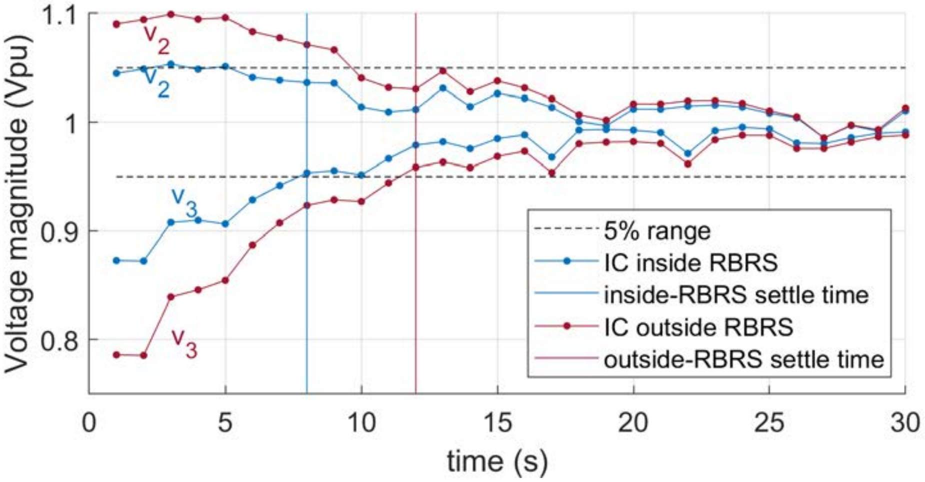

Figure 4.6: Simulation of DER system (4.9) on the 4NF with initial conditions marked in Fig. 4.5. For v_2 and v_3, the phase (among A,B,C) furthest from one per unit is plotted. The initial condition in the RBRS (blue) arrives in the 5% ANSI range within the 10-second time limit, while the initial condition outside the RBRS (red) does not.

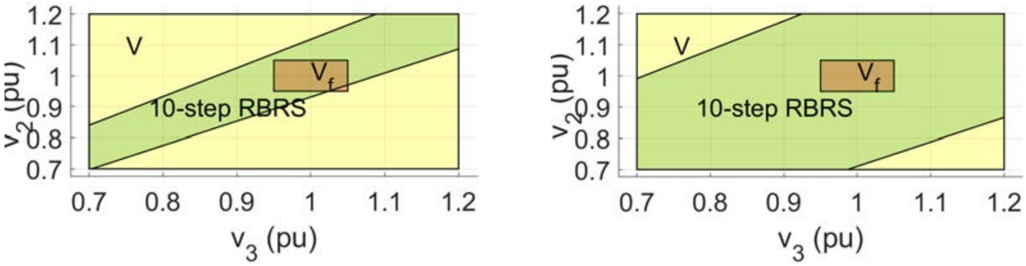

Figure 4.7: Ten-step robust backward reachable set (RBRS) computed using modified parameters on the 4NF. ***Left:*** RBRS when increase base case w bounds by 30%. ***Right:*** RBRS when decrease base case w bounds by 30%.

We validate the RBRS computed with the linear single phase system model (4.9) by simulating the system in Opal-RT's ePHASORSIM, which solves nonlinear three-phase power flow. We turn off inverter capacity limits to focus on the control response settle times. $\mathcal{K}_{10}$ in Fig. 4.5 indicates initial voltages where the trajectory will reach the target set within 10 seconds. We set the system's net loads such that the initial voltage is inside the RBRS as marked in Fig. 4.5, then observe in Fig. 4.6 convergence to the target set after 8 seconds. In contrast, when we set the initial voltage outside the RBRS as marked in Fig. 4.5, in Fig. 4.6 we observe convergence after 12 seconds. This difference demonstrates the power of the 10-step RBRS guarantee.

Next we modify the base case parameters from Table 4.2 to observe the effect on the RBRS shape. We increase the magnitude of w_{lb} and w_{ub} by 30%, which results in the new RBRS in the left panel of Fig. 4.7. The RBRS has narrowed because the control actions cannot match the fluctuation that now lie in a larger $\mathcal{W}$. We observe RBRS of a similar shape to the left panel in Fig. 4.7 for the case of decreasing the controller gains by 30%, and for the case of decreasing r_{01} and x_{01} by 20%. Conversely, when we decrease the magnitude of w_{lb} and w_{ub} by 30%, we have the RBRS in the right panel of Fig. 4.7, which is wider than the base case. We observe RBRS of a similar shape to the right panel in Fig. 4.7 for the case of increasing the controller gains by 30%, and for the case of increasing r_{01} and x_{01} by 20%.

4.3.2 Larger Networks

Next we validate the reachability analysis on larger unbalanced feeders with the same simulation process. For the IEEE 123-node feeder (123NF) [72], we design incremental volt-var controller gains for inverters at 15 random nodes that satisfies the condition (4.10). Then we compute the RBRS and in the left panel of Fig. 4.8 project the set onto node 49 and 52, two inverter locations in the middle of the feeder. We observe that locations at the end of the feeder have narrow projected reachable sets, while locations at the top of the feeder

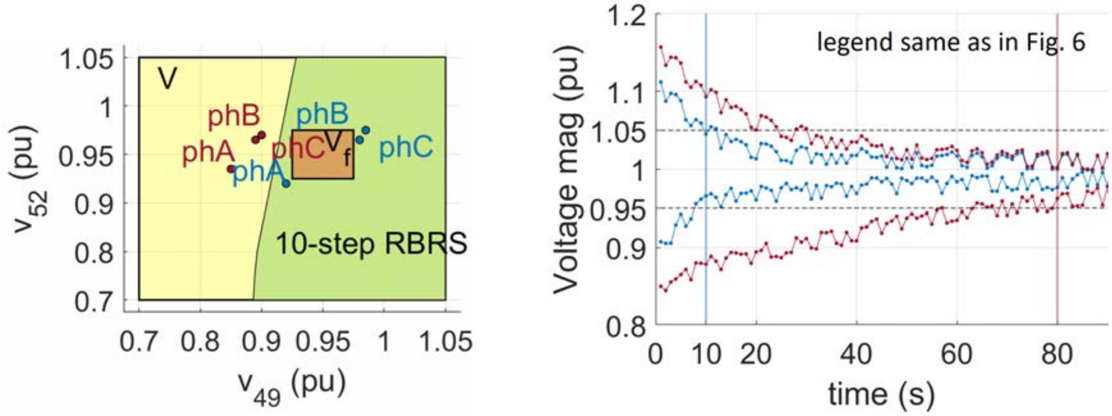

Figure 4.8: Ten-step robust backward reachable set, and simulation of two initial condition instances on the three-phase unbalanced 123NF. ***Left:*** Plot of RBRS with a three-phase initial condition outside the RBRS (red), and three-phase initial condition inside the RBRS (blue). ***Right:*** Simulation of DER control starting from the IC in the left panel. When the IC is outside the RBRS, the voltage doe not reach the safe set within 10 time steps.

have wider ones. This observation is consistent with the stability line length relationships found in [51]. We then simulate voltages at all incremental volt-var controllers locations, and plot the voltages furthest above and below 1Vpu in the right panel of Fig. 4.8. As expected, when the initial voltage is outside the RBRS, the system does not reach the 5% ANSI range in 10 seconds, in fact it takes 80 seconds in this case. The large difference in settling time (10s vs. 80s) may be due to coupling interactions between the 15 inverters and their controlled phases.

The RBRS computation times for the different feeder sizes are in Table 4.3. The MATLAB MPT toolbox functions execute slowly for large systems, but we note that Python, a faster implementation language, does not have an equivalent polytopic geometry toolbox.

Table 4.3: Computation times for computing the 7-step, 10-step, and 14-step RBRS $\mathcal{K}_N$ on circuits of different sizes.

N	**4NF**	**IEEE 13NF**	**IEEE 123NF**
7	0.2 min	4.5 min	63 min
10	1.3 min	7.7 min	81 min
14	2 min	26 min	149 min

4.4 Conclusion

In this work we considered the abnormal voltage excursion scenario in which DERs have a given time limit to stay connected and respond. We captured fluctuations in the voltage during this period, including voltage regulation equipment actions, with a multimodal gaussian distribution model. We then used this disturbance model to perform a reachability analysis which determines the largest range of abnormal conditions that our DER control is guaranteed to overcome. The benefit of this analysis is that the resulting reachable set captures the worst case response to the voltage fluctuations, while in contrast it could it may take many simulations to observe the same result. The system parameters were varied to understand their effect on the shape of the backwards reachable sets, and the set guarantees were validated by simulating on unbalanced feeders of different sizes.

Chapter 5

Hybrid System Stability of Load-Tap Changers and Inverters

This chapter is based on the paper 'Parameter Conditions to Prevent Voltage Oscillations Caused by LTC-Inverter Hunting on Power Distribution Grids' [89], written in collaboration with Federico Celi, Fabio Pasqualetti, and Alexandra von Meier.

In this chapter, rather than capture the actions of legacy voltage regulation equipment as external disturbances as done in Chapter 4, we directly model these device actions in concert with inverter-based DERs. Our model, composed of two LTCs and two inverter devices, is shown to create voltage oscillations even with reasonable choices of control parameters. The model is a switched affine hybrid system, allowing us to analyze the system's oscillatory behavior, both during normal operation and following a cyber-physical attack. Through the analysis we determine the specific region of the voltage state space where oscillations are possible and derive conditions on the control parameters to guarantee against the oscillations. Finally, we project the derived parameter conditions onto two-dimensional spaces to demonstrate important relationships between device operating parameters.

5.1 Introduction

The traditional voltage regulation problem is to design load-tap changer (LTC), voltage regulator, and capacitor bank control parameters such that, over a minutes-to-day duration, the distribution grid voltage is kept within 5% of the nominal voltage (ANSI C84.1 standard) to avoid interrupting or damaging customer equipment. The addition of naively controlled DERs such as solar PV makes this voltage regulation problem harder [90] and can cause LTCs to actuate much more frequently, reducing their lifespan. Depending on the control logic and design parameters, connecting smart inverters can either alleviate [91] these voltage fluctuations or be a source of adverse interactions [92].

One type of adverse interaction is *device hunting* which we define as one or more devices actuating in a repeated sequence that results in periodic voltage oscillations. Hunting among LTCs has been observed by utilities since the 1980s [93,94] and has been modeled as a hybrid system in the literature [94]. Inverter-based DERs may be able to solve these problems if their control parameters are set appropriately. However, current inverter standards [6] require inverter control parameters to be adjustable by a remote entity's communication network, which introduces a potential vulnerability to cyberattacks [95]. Bad parameters sent to inverters on a circuit, whether deliberately or by mistake, can trigger adverse interactions [96]. This motivates our investigation into how a poor choice of device parameters can lead to hunting, as simulated in Fig. 5.1.

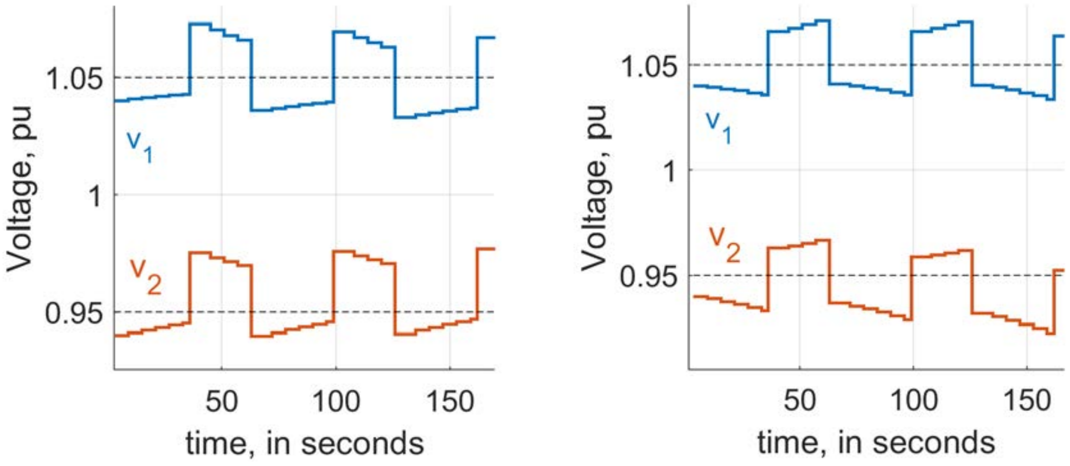

Figure 5.1: Simulation of two LTCs and two inverters that create voltage oscillations with a period of 70 seconds. Circuit is in Fig. 5.2 and parameters are the defaults listed in Table 5.1. ***Left:*** Device hunting when $g = 0.5$. ***Right:*** Device hunting when $g = -0.5$

There are two common approaches when selecting distribution-grid device parameters for voltage control: an approach based on rules of thumb followed by simulation, and an optimization-based approach. For basic operation of LTCs and parameter rules of thumb we refer to the text [22, Chapter 9.3], and to papers [54, 90]. One limitation of this approach is the assumed timescale separation between the LTC and inverters, which may not hold when LTCs delays are shortened to handle increased voltage variability [97]. Moreover, the simulations in these papers are not sufficient to guarantee against the possibility of sustained voltage oscillations.

Meanwhile, optimization methods focus on addressing the non-convexity of the mixed-integer optimal power flow problem resulting from including both continuous (smart inverter) and discrete (LTC and voltage regulator) dynamics [23, 24]. However, the optimal parameter solution determines tap positions and power dispatch rather than the device parameters in the control law. As such, the optimal solution does not provide significant insights into the symbolic relationship between control parameters and adverse interactions.

Our goal of deriving symbolic parameter conditions for hybrid systems stability is a challenging task and remains relatively unexplored in control systems literature. The design of switching strategies for stabilization commonly assumes one can switch modes at any time, rather than switching according to parameterized conditions [98,99]. Linear parameter variation (LPV) literature commonly assumes the parameters to be time-varying, but here our parameters are time-independent and we want to solve for them symbolically [100]. Therefore, our methodology leverages our familiarity with the specific system's model dynamics.

In this chapter, we analyze how parameters of LTCs and inverters prevent or contribute to voltage oscillations created by device hunting. The results yield two distinct benefits: (i) the parameter conditions can provide intuition for improving the rules of thumb used to operate these devices in industry and (ii) the conditions can be directly checked on each device without simulations, enabling real-time checks on incoming parameter updates by remote entities.

The rest of this chapter organized as follows. In Sec. 5.1, we introduce the LTC-DER coordination problem. In Sec. 5.2, the system equations are presented and the parameter condition problem is solved for two subsystems. In Sec. 5.3, the parameter condition problem is solved for the full system. In Sec. 5.4 the conditions on the full system conditions are illustrated. In Sec. 5.5 we present conclusions and future work. We include proofs of the main theorem and lemmas in-line, and refer readers to Appendix 7.3 for the minor proofs.

5.2 System Dynamics and Subsystem Analysis

5.2.1 Notation

Let $\mathbb{R}^n$ be the n-dimensional vector of real numbers and $\mathbb{R}^{n\times n}$ the matrix of real numbers. We use bold-faced letters for vectors and matrices, with the exception that $\mathbf{j} = \sqrt{-1}$ indicates the imaginary part of complex numbers. For a vector $\boldsymbol{x} \in \mathbb{R}^n$, let $\boldsymbol{x}[k]$ be its value at time index $k \in \mathbb{R}$, and $\boldsymbol{x}_i[k]$ be the value of the i-th element of $\boldsymbol{x}$ at time index k. Let $x^\top$ be the transpose of vector x. Let $||.||_i$ denote the ℓ_i vector norm for $i = 1, 2, \infty$. We define the *margin* $M(S, d)$ as the set of points x that are within distance d from a set S. We define a *partition* of a set S to be a collection of subsets S_i, $i = 1, ...k$ such that $\bigcup_{i=1,...,k} S_i = S$ and $S_i \cap S_j = \emptyset$ for all $i \neq j$. We use $\rightarrow$ and $\nrightarrow$ to indicate possible and impossible transitions between partitions, respectively. Let S' denote the complement of set S, and $S \setminus Q$ be the part of the set S that is not in Q.

5.2.2 Overview of Four-Device System

We model four devices operating on the radial circuit shown in Fig. 5.2. Suppose there are constant loads at all nodes shown. LTC1 and inverter1 regulate voltage v_1, while LTC2 (sometimes called a line voltage regulator) and inverter2 regulate voltage v_2. We define the

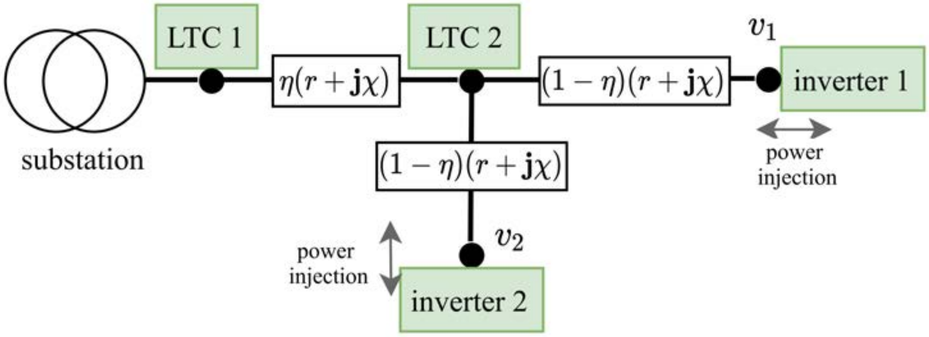

Figure 5.2: Radial distribution circuit with voltages of interest v_1 and v_2, as well as two LTC and two inverter devices.

difference between the two voltages of interest with

$$v^{\text{diff}} := v_1 - v_2 \in \mathbb{R}^1. \tag{5.1}$$

The LTCs estimate v_1 and v_2 voltages using line drop compensation, and the inverters measure these voltages with their internal sensors. All devices operate with fixed time delay logic; that is, they only respond when the voltage remains outside the deadband for a certain delay d. We denote the upper deadband boundary as $v^+ = v^{ref} + \varepsilon$, and lower deadband boundary as $v^- = v^{ref} - \varepsilon$, where $v^{ref} \in \mathbb{R}^1$ is the nominal voltage. Then we define the deadband

$$D := \{(v_1, v_2) : v^- \leq v_1 \leq v^+,\ v^- \leq v_2 \leq v^+\}. \tag{5.2}$$

Because there are no active dynamics when both voltages are in the deadband, the set D is invariant. We define vectors $\boldsymbol{v} = [v_1\ v_2]^\top \in \mathbb{R}^2$ and $\boldsymbol{v}^{ref} = [v^{ref}\ v^{ref}]^\top \in \mathbb{R}^2$, since it is common to assume the nominal voltage is the same for all circuit nodes. When $v_i > v^+$ for $i = 1, 2$ we say v_i has an *overvoltage*, and when $v_i < v^-$ we say v_i has an *undervoltage*. With the shorthand $v_i \in D$ or $v_i \notin D$, we refer to whether $v^- < v_i < v^+$ is satisfied or not.

Next, we define normal operating $W := (H \cap P)$ where

$$H := \{(v_1, v_2) : (v_1 > v^- \text{ and } v_2 > v^-) \text{ or } (v_1 < v^+ \text{ and } v_2 < v^+)\} \tag{5.3}$$

$$P := \{(v_1, v_2) : \left\|\boldsymbol{v}[k] - \boldsymbol{v}^{ref}\right\|_\infty < 3\varepsilon\}. \tag{5.4}$$

The hourglass-shaped set H disallows one voltage from being above v^+ when the other is below v^-. P bounds the distance each voltage can be away from v^{ref}.

Assumption 7. *(normal operation) A given system Σ operates in normal operating states W defined by* (5.3) *and* (5.4)*.*

We consider states outside W to be abnormal operating conditions that should be addressed with the grid's protection system rather than the system dynamics analyzed in this work. We are interested in the system behavior while $v \in W$, especially if the initial condition (IC) starts in W and eventually leaves W.

The goal is to coordinate the device actions so that v_1 and v_2 land inside the deadband without device hunting. Table 5.1 summarizes the notation for the states, fixed variables, and parameters we are interested in designing to guarantee against hunting. The table also assumes relationships from basic operation of power systems that are drawn from [22, Chapter 9.3] and [13]. In the table, all fixed variables and parameters except for g are taken to be positive and real valued because of their physical meaning.

Table 5.1: Notation for major variables in Chapter 5. The type of variable, description with units, default value, and the basic relationship between variables are included.

Symbol	**Type**	**Description**	**Default**	**Relationship**
v^{ref}	fixed	voltage ref. (p.u.)	1.0	–
ε	fixed	half of deadband width	0.1	–
v^-, v^+	fixed	deadband boundary	0.95, 1.05	$v^- = v^{ref} - \varepsilon$, $v^+ = v^{ref} + \varepsilon$
χ	fixed	line reactance (p.u.)	0.1	–
η	fixed	impedance damping factor	0.9	$0 < \eta < 1$
v_{10}	state	node 2 initial voltage (p.u.)	1.04	–
v_{20}	state	node 3 initial voltage (p.u.)	0.94	–
d_{inv}	parameter	inverter 1 and 2 delay (s)	4	$d_{inv} < d_{L1}$
d_{L1}	parameter	LTC1 delay (s)	30	–
d_{L2}	parameter	LTC2 delay (s)	40	$d_{L1} < d_{L2}$, $d_{L2} < 2d_{L1}$
$\bar{v}_L$	parameter	tap voltage (p.u.)	0.03	$\bar{v}_L < 2\varepsilon$
g	parameter	inverter 1 and 2 control gain	–	–

5.2.3 Conditions for Two-LTC System

Let the Σ_1 be the subsystem where LTC1 and LTC2 operate on the circuit in Fig. 5.2 normally (see Assumption 7). Both devices have the same deadband width 2ε that is centered on the same voltage reference v^{ref}. When the voltage is outside the deadband for d_{L1} (d_{L2}) seconds, LTC1 (LTC2) taps, which updates both voltages according to $\boldsymbol{v}[k+1] = \boldsymbol{v}[k] \pm [\bar{v}_L \; \bar{v}_L]^\top$ where $\boldsymbol{v} = [v_1 \; v_2]^\top \in \mathbb{R}^2$. Because all tap actions shift both voltages by $\bar{v}_L$ amount, tapping manifests as discrete jumps on the (v_1, v_2) space with slope of ±1 between the initial and after-tap voltage.

Lemma 4. *If $\bar{v}_L > 2\varepsilon$, system Σ_1 will have marginally stable oscillations for all time when any $v_1[0] \in M(D, c)$ or $v_2[0] \in M(D, c)$ where $c = \bar{v}_L - 2\varepsilon > 0$.*

Distribution engineers know not to set $\bar{v}_L > 2\varepsilon$ when choosing LTC settings, so next we focus on how oscillations could occur when $\bar{v}_L \leq 2\varepsilon$.

We partition W into four regions D, W_g, W_b, W_o, based on the possible trajectories from starting the system in each region. We define W_o such that from there we only transition to the deadband or oscillate. For example, v_1 should satisfy $v_1 - \bar{v}_L < v^+$. Therefore we define the boundary of W_o in terms of the v_i^* that satisfies $v_i^* - \bar{v}_L = v^+$ for $i = 1, 2$. This gives the regions

$$\begin{aligned} W_o = \{(v_1, v_2) \in W : (&v_1 \in M(D, v_1^* - v^+) \text{ and } v_2 \in D), \\ &\text{or } (v_2 \in M(D, v_2^* - v^+) \text{ and } v_1 \in D)\}, \end{aligned} \tag{5.5a}$$

$$\begin{aligned} W_b = \{(v_1, v_2) \in W : (&v_1, v_2 > v^+ \text{ and } v_1 + v_2 \leq v^+ \\ &+ \bar{v}_L), \text{ or } (v_1, v_2 < v^- \text{ and } v_1 + v_2 \geq v^- - \bar{v}_L)\}, \end{aligned} \tag{5.5b}$$

and W_g is what remains of W. That is, $W_g = W \setminus (D \cup W_o \cup W_g)$.

Fig. 5.3 shows these regions in the state space as well as the possible transitions between regions W_g, W_o, W_b, D, and W'. For W_g possibilities, LTC jumps having a slope of ±1 implies that the only way $W_g \to W'$ is by $W_g \to H' \subset W'$. Because W_g is $\bar{v}_L$ away from D, $W_g \nrightarrow D$. For W_b possibilities, LTC jumps having a slope of ±1 implies that W_b cannot transition to W' nor W_g. For W_o possibilities, LTC jumps having a slope of ±1 implies that the only way $W_o \to W'$ is by $W_o \to H' \subset W'$. By the same logic, W_o cannot transition to W_b nor W_g. Finally, from the geometry of Fig. 5.3, observe that if $v^{\text{diff}}[0] < 2\varepsilon$, $W_o \nrightarrow W'$.

Lemma 5. *If $\bar{v}_L \leq 2\varepsilon$, $\boldsymbol{v}[T] \in W_o$, and $v^{diff} < 2\varepsilon - \bar{v}_L$, system Σ_1 will have marginally stable oscillations starting at time T.*

A simulation of marginally stable oscillations due to Lemma 5 hunting is in Fig. 5.4.

5.2.4 Conditions for Two-Inverter System

Let the Σ_2 be the subsystem where the two inverters operate on the circuit in Fig. 5.2 normally (see Assumption 7). For now we omit the deadband in the control logic. We employ a discrete integrator (called incremental volt-var control in [1, 12, 13, 44]) for computing inverter reactive power set-points $\boldsymbol{q}^{inv}$ with

$$\boldsymbol{q}^{inv}[k+1] = \boldsymbol{q}^{inv}[k] - \boldsymbol{G}(\boldsymbol{v}[k] - \boldsymbol{v}^{ref}), \tag{5.6}$$

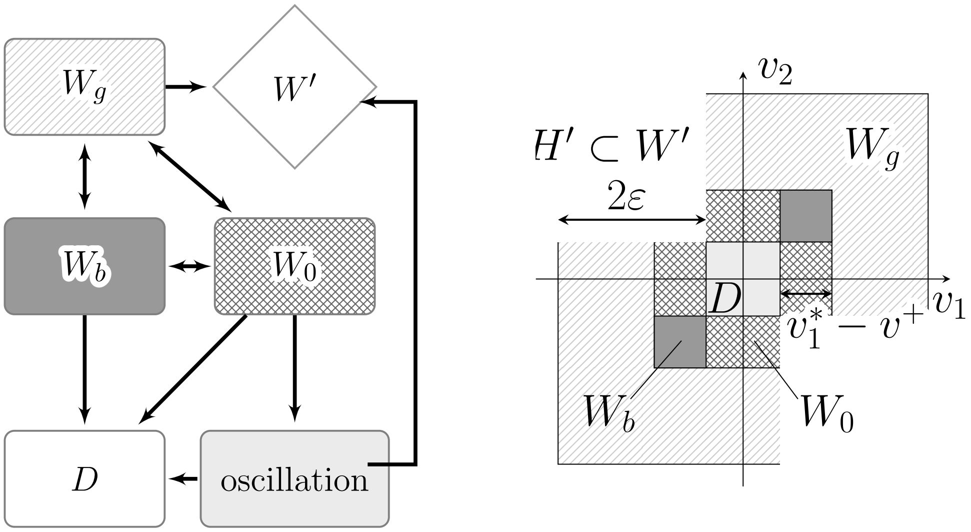

Figure 5.3: State space behavior of the two-LTC system Σ_1 when $\bar{v}_L < 2\varepsilon$. ***Left:*** State transition diagram, indicating the possible behavior of trajectories. ***Right:*** State space partitioned into regions based on trajectory behavior.

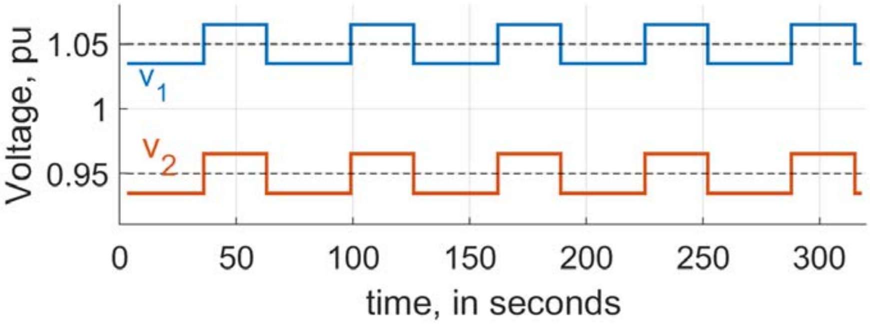

Figure 5.4: Simulation of the two-LTC system Σ_1 when Lemma 5 holds. Parameters are the defaults listed in Table 5.1. Marginally stable oscillations are observed.

For any radial circuit with n inverters at different nodes, $v \in \mathbb{R}^n$, $\boldsymbol{q}^{inv} \in \mathbb{R}^n$, and $\boldsymbol{G}$ is a diagonal matrix with controller gains along the diagonal. Note that we map the voltage magnitude tracking error to the *change* in inverter power output at all nodes so that the power set-point increments while the tracking errors persist. $\boldsymbol{G}$ being diagonal enforces that each inverter is injecting power to regulate the voltage at its own node.

We assume that each inverter inject power that is equal to the computed power set-points. The algebraic power flow equations that map inverter power injections to voltages can be represented by

$$\boldsymbol{v}[k+1] = \boldsymbol{v}[k] + \boldsymbol{X}(\boldsymbol{q}^{inv}[k+1] - \boldsymbol{q}^{inv}[k]) \tag{5.7}$$

from [1, equation 8]. Matrix element X_{ij} is the common-node impedance reactance between node i and node j on the network (see section 2.1.5 for background on X). Next, we substitute (5.6) into (5.7), giving

$$\boldsymbol{v}[k+1] = \boldsymbol{v}[k] - \boldsymbol{X}\boldsymbol{G}(\boldsymbol{v}[k] - \boldsymbol{v}^{ref}). \tag{5.8}$$

Finally, we subtract $\boldsymbol{v}^{ref}$ from both sides and define $e[k] \coloneqq \boldsymbol{v}[k] - \boldsymbol{v}^{ref}$, giving [1, equation 12]:

$$\boldsymbol{e}[k+1] = (\boldsymbol{I} - \boldsymbol{X}\boldsymbol{G})\boldsymbol{e}[k]. \tag{5.9}$$

Author [1] proves in their Theorem 3.1 that for the system (5.9), $v \to \boldsymbol{v}^{ref}$ iff

$$0 \prec \boldsymbol{G} \prec 2\boldsymbol{X}^{-1}.. \tag{5.10}$$

For intuition, condition (5.10) applied to the one-dimensional case (one inverter acting on a single phase circuit) establishes that the integrator gain g should satisfy $0 < g < 2/\chi$. This condition implies that under normal operation, g should be positive but not too large to have the voltages converge. We are also interested in the possibility of $g < 0$, where the inverters push the voltage away from $\boldsymbol{v}^{ref}$, because that case is more dangerous.

Lemma 6. *If $\boldsymbol{G} \prec 0$, system Σ_2 given by* (5.9) *has $v \to \pm\infty$.*

When the deadband is introduced, inverters only operate according to (5.6) when their voltage is outside the deadband. Because $\boldsymbol{v}^{ref}$ is centered in the deadband, Lemma 6 holds in the same way as the no-deadband case, and the convergence condition (5.10) yields $\boldsymbol{v} \to D$ instead of $\boldsymbol{v} \to \boldsymbol{v}^{ref}$.

Power injections have the greatest effect on voltages at injection node and less effect on voltages electrically far away from the injection point. For our system Σ_2, $\boldsymbol{G} = diag([g\ g])$ and $q = [q_1\ q_2]$. The dissipative nature of power grids due to line impedances causes the diagonal terms of $\boldsymbol{X}$ to be larger than the off-diagonal terms. From the circuit in Fig. 5.2, system Σ_2 has

$$\boldsymbol{X} = \begin{bmatrix} \chi & \eta\chi \\ \eta\chi & \chi \end{bmatrix}, \tag{5.11}$$

where the damping factor η satisfies $0 < \eta < 1$. In general, if inverters have different reactances in the line path to the substation, $\eta_1 = \boldsymbol{X}_{21}/\boldsymbol{X}_{11}$ and $\eta_2 = \boldsymbol{X}_{12}/\boldsymbol{X}_{22}$. Because in this work we only use η for its property of $0 < \eta < 1$, using $\eta = \eta_1 = \eta_2$ does not change the results.

5.3 Full System Analysis

5.3.1 Modeling as a Hybrid System

Next we model all devices in Fig. 5.2 operating normally (see Assumption 7) as a discrete hybrid automaton, which is the interconnection of a finite state machine with a switched affine system. This system, Σ^3, has state vector $x = \begin{bmatrix} z_1 & z_2 & z_3 & v_1 & v_2 \end{bmatrix}^\top$, where z_1, z_2, z_3 are the internal timers for LTC1, LTC2, and inverter1 and 2, respectively. The two inverters use the same timer z_3 because they have the same delay of d_{inv}. Let T_s be the timestep of the discrete model. Each mode has a label with the format $m^\star 0$ where $\star = 1, 2, ...8$, and has affine dynamics of the form $x[k+1] = Ax[k] + c$ where $A \in \mathbb{R}^{5\times 5}$ and $c \in \mathbb{R}^5$. To define the switching conditions, we define a function f for whether a voltage is inside the deadband:

$$f_i \coloneqq max(v_i - v^+, 0) - max(v^- - v_i, 0) \text{ for } i = 1, 2. \tag{5.12}$$

For $i = 1, 2$, if v_i is an overvoltage then $f_i > 0$. If it is an undervoltage then $f_i < 0$, and if inside D then $f_i = 0$. Inverter1 (LTC1) responds when $f_1 \neq 0$ for d_{inv} (d_{L1}) seconds, and Inverter2 (LTC2) responds when $f_2 \neq 0$ for d_{inv} (d_{L2}) seconds.

Now we introduce the hybrid model, where we make the design parameters highlighted in light gray.

m10: tap LTC1 up

Switch condition: $z_1 > d_{L1}$ and $(f_1 + f_2 < 0)$

Dynamics:

$$\begin{bmatrix} z_1 \\ z_2 \\ z_3 \\ v_1 \\ v_2 \end{bmatrix}_{k+1} = \begin{bmatrix} 0 & 0 & 0 & 0 & 0 \\ 0 & 1 & 0 & 0 & 0 \\ 0 & 0 & 1 & 0 & 0 \\ 0 & 0 & 0 & 1 & 0 \\ 0 & 0 & 0 & 0 & 1 \end{bmatrix} \begin{bmatrix} z_1 \\ z_2 \\ z_3 \\ v_1 \\ v_2 \end{bmatrix}_k + \begin{bmatrix} T_s \\ T_s \\ T_s \\ \bar{v}_L \\ \bar{v}_L \end{bmatrix}$$

---

m20 (tap LTC1 down) is the same as m10 except the condition has $(f_1 + f_2) > 0$ and the affine term is $[T_s \ T_s \ T_s \ -\bar{v}_L \ -\bar{v}_L]^\top$.

---

m30: tap LTC2 up

Switch condition: $z_2 > d_{L2}$ and $(f_1 + f_2 < 0)$

Dynamics:

$$\begin{bmatrix} z_1 \\ z_2 \\ z_3 \\ v_1 \\ v_2 \end{bmatrix}_{k+1} = \begin{bmatrix} 1 & 0 & 0 & 0 & 0 \\ 0 & 0 & 0 & 0 & 0 \\ 0 & 0 & 1 & 0 & 0 \\ 0 & 0 & 0 & 1 & 0 \\ 0 & 0 & 0 & 0 & 1 \end{bmatrix} \begin{bmatrix} z_1 \\ z_2 \\ z_3 \\ v_1 \\ v_2 \end{bmatrix}_k + \begin{bmatrix} T_s \\ T_s \\ T_s \\ \bar{v}_L \\ \bar{v}_L \end{bmatrix}$$

---

m40 (tap LTC2 down) is the same as m30 except the condition has $(f_1 + f_2) > 0$ and the affine term is $[T_s \ T_s \ T_s \ -\bar{v}_L \ -\bar{v}_L]^\top$.

---

m50: inverter(s) respond to voltage issues

Switch condition: $z_3 > d_{inv}$ and $(f_1 \neq 0 \text{ or } f_2 \neq 0)$

Dynamics:

$$\begin{bmatrix} z_1 \\ z_2 \\ z_3 \\ v_1 \\ v_2 \end{bmatrix}_{k+1} = \begin{bmatrix} 1 & 0 & 0 & 0 & 0 \\ 0 & 1 & 0 & 0 & 0 \\ 0 & 0 & 0 & 0 & 0 \\ 0 & 0 & 0 & 1-\chi g & -\eta\chi g \\ 0 & 0 & 0 & -\eta\chi g & 1-\chi g \end{bmatrix} \begin{bmatrix} z_1 \\ z_2 \\ z_3 \\ v_1 \\ v_2 \end{bmatrix}_{k} +$$

$$\begin{bmatrix} T_s & T_s & T_s & \chi g v^{ref} + \eta\chi g v^{ref} & \eta\chi g v^{ref} + \chi g v^{ref} \end{bmatrix}^\top$$

---

m60: reset LTC2 and inverter timers
Switch condition: $[m = m10$ and $(f_1 > 0$ or $f_2 > 0)]$ or $[m = m20$ and $(f_1 < 0$ or $f_2 < 0)]$

Dynamics: $z_2[k+1] = T_s,\ z_3[k+1] = T_s, \quad \boldsymbol{v}[k+1] = \boldsymbol{v}[k]$

---

m70: reset LTC1 and inverter timers
Switch condition: $[m = m30$ and $(f_1 > 0$ or $f_2 > 0)]$ or $[m = m40$ and $(f_1 < 0$ or $f_2 < 0)]$

Dynamics: $z_1[k+1] = T_s,\ z_3[k+1] = T_s, \quad \boldsymbol{v}[k+1] = \boldsymbol{v}[k]$

---

m80: increment timers

Switch condition: no other mode conditions hold

Dynamics: $z_i[k+1] = z_i[k] + T_s\ \forall i = 1, 2, 3,\ \boldsymbol{v}[k+1] = \boldsymbol{v}[k]$

Remark 3. *By the relationship $d_{inv} < d_{L1} < 2d_{L2}$ from Table 5.1, the inverters respond to voltage issues before LTC1. This relationship is a less conservative version of $d_{inv} \ll d_{L1}$, which is often made for power systems [90]. Therefore, an LTC will never tap twice before an inverter acts.*

Summary of Switched Affine Form

We have formulated a discrete hybrid automaton for the system of two LTCs and two inverters. The LTC and inverter actions are modeled with discrete dynamics in each mode, while each mode transitions to a different set of dynamics, resulting in a piecewise continuous state trajectory across mode changes. The eight modes of the 4-device hybrid system are

m10 : $x_{k+1} = A_1 x_k + c_1$ LTC1 tap up due to under-voltage
m20 : $x_{k+1} = A_2 x_k + c_2$ LTC1 tap down due to over-voltage
m30 : $x_{k+1} = A_3 x_k + c_1$ LTC2 tap up due to under-voltage
m40 : $x_{k+1} = A_4 x_k + c_2$ LTC2 tap down due to over-voltage
m50 : $x_{k+1} = A_5 x_k + c_3$ inverter(s) respond to voltage issues
m60 : $x_{k+1} = A_6 x_k + c_4$ reset LTC2 and inverter timers
m70 : $x_{k+1} = A_6 x_k + c_5$ reset LTC1 and inverter timers
m80 : $x_{k+1} = A_7 x_k + c_6$ increment timers

5.3.2 Behavior when $g > 0$

For positive values of the inverter gain g, our control action renders the voltage dynamics stable, as shown next.

Theorem 4. *(Stability when $g > 0$) If system Σ_3 has $0 < g < \frac{2}{\chi}$, there exists $T > 0$ such that $\boldsymbol{v}[k] \in D$ for all $k \geq T$.*

Proof. In order to show the voltage vector v converges to the deadband region D, we seek one or multiple Lyapunov functions Y that characterize the system's energy. We consider the following candidate common lyapunov function for all modes m10 through m80:

$$Y(\boldsymbol{v}) = ||\boldsymbol{v}^{ref} - \boldsymbol{v}||_1 \tag{5.13}$$

If the initial condition satisfies $Y \leq \varepsilon$, then $v \in D$ and the proof is complete the system is totally stationary in D. Thus we focus on initial conditions where $v \in W \setminus D$ and $Y > \varepsilon$.

From [101, Theorem 3.2], if a hybrid system satisfies (i) $Y(\boldsymbol{v}^{ref}) = 0$, (ii) $Y(\boldsymbol{v}) > 0$ for $\boldsymbol{v} \neq \boldsymbol{v}^{ref}$, (iii) $\boldsymbol{v}$ is non-increasing across mode changes, and (iv) there exists some τ where $Y(\boldsymbol{v}[k+\tau]) \leq Y(\boldsymbol{v}[k])$, then $\boldsymbol{v} = \boldsymbol{v}^{ref}$ is an equilibrium point that is stable in the sense of Lyapunov (SISL). From inspection, Y (5.13) satisfies (i) and (ii). Because in section 5.3 the system was formulated as a switched affine hybrid system, (iii) is satisfied. Next, we must show that the energy is non-increasing in each mode, i.e. there exists a τ such that $Y(\boldsymbol{v}[k+\tau]) \leq Y(\boldsymbol{v}[k])$ for $\forall\ \boldsymbol{v}[k] \in W \setminus D$.

For mode m60 to m80, $\boldsymbol{v}[k+1] = \boldsymbol{v}[k]$. For m10-m40, where an LTC takes action, we observe that $Y(\boldsymbol{v}[k+\tau]) = Y(\boldsymbol{v}[k])$ when $\bar{v}_L < 2\varepsilon$. For intuition, the chosen L1 norm for Y (5.13) is a diamond shape when projected onto the 2D voltage state space, so when an LTC taps, the system jumps with slope ±1, thereby maintaining constant energy. For mode 50, the dynamics of $\boldsymbol{v}[k]$ from section 5.3 can be rewritten as

$$Y(\boldsymbol{v}[k+1]) = \begin{bmatrix} 1-\chi & -\eta\chi g \\ -\eta\chi & 1-\chi g \end{bmatrix} Y(\boldsymbol{v}[k]).$$

Observe that if the parameter condition $0 < g < \min\{\frac{1}{x_{11}}, \frac{1}{x_{22}}\}$ holds, for $Y(\boldsymbol{v}[k+1]) < Y(\boldsymbol{v}[k])$. The reduction of energy in m50 is due to the damped effect that inverter actions have on voltages electrically distant from them, which is captured with $\eta < 1$ from Table 5.1. Because the system loses energy in m50 and all other modes have constant energy, condition (iv) is satisfied. Therefore, the system is SISL.

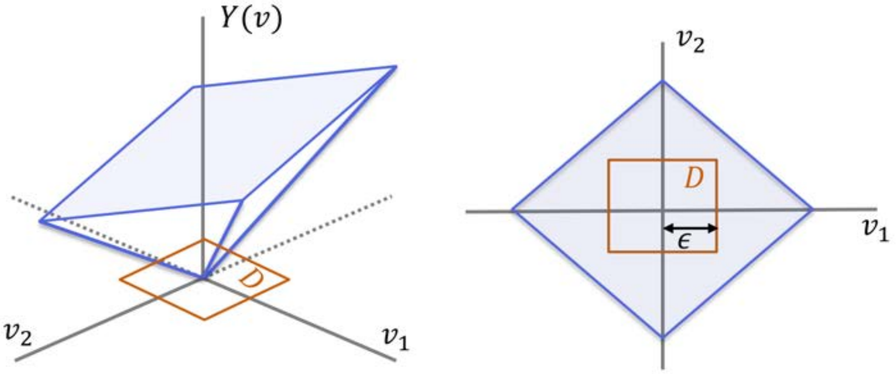

Figure 5.5: Diagram of voltage state space with Lyapunov function values on the third axis. An example Lyapunov function level set $\{\boldsymbol{v} \in \mathbb{R}^2 : Y(\boldsymbol{v}) = \gamma, \gamma > \epsilon\}$ is in blue, and the voltage deadband is in orange. ***Left:*** Isometric view. ***Right:*** Top view.

Next, we need to prove the stronger guarantee of asymptotic stability, where the system converges to set D containing the the equilibrium point $\boldsymbol{v}^{ref}$. A diagram of this argument is shown in Fig. 5.5. Due to the choice of the L1 norm in (5.13), the projection of the system's energy levels onto the 2D voltage space are concentric diamonds centered at the equilibrium $\boldsymbol{v}^{ref}$. Since at least one timer state z_i for $i = 1, 2, 3$ increments in every mode, the LTCs and inverter action modes will be visited for all time where $\boldsymbol{v} \notin D$. Then with Remark 3, the design choice of $d_{inv} < d_{L1} < 2d_{L2}$ ensures that the system always visits m50 at least once after visiting one of the LTC modes. Every time the inverters act in m50, the system loses energy, causing the the system energy level set become smaller concentric diamonds. Therefore, there exists a $k > T$ where the projection of the level set onto the voltage space is inscribed in D, at which point $Y[k] \leq \varepsilon$ and $\boldsymbol{v}[k] \in D$.

$\square$

The consequence of Theorem 4 is that for realistic values of the network with $g > 0$, the system exhibits damped oscillations which eventually reach the deadband. Thus, we focus the remainder of this paper on the more dangerous scenario where $g < 0$ renders any oscillations unstable.

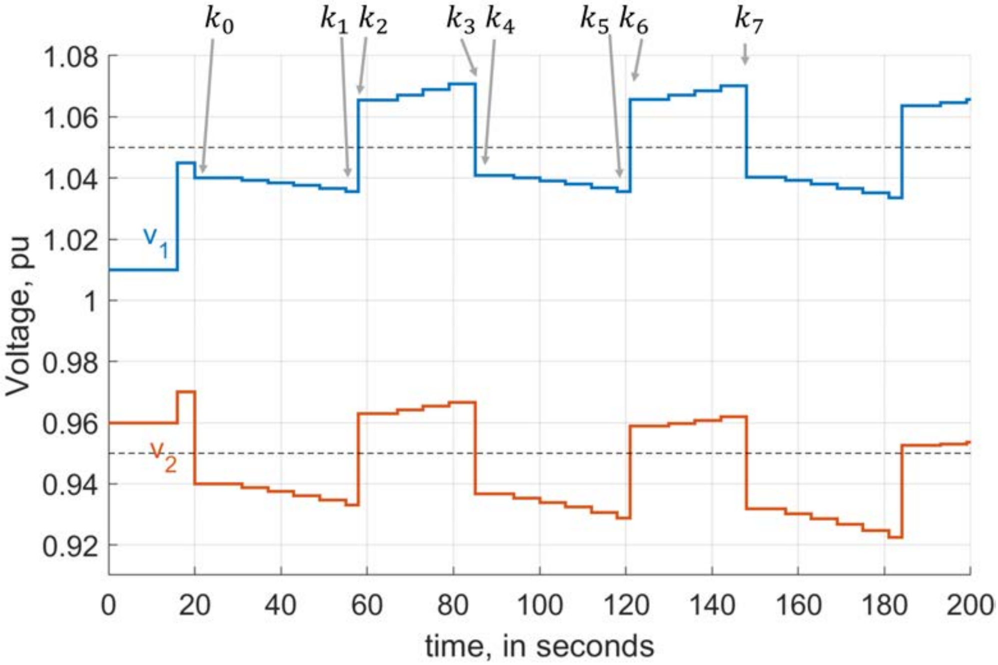

Figure 5.6: Simulation of the four-device system Σ_3 when $g < 0$. The simulation parameters are the defaults in Table 5.1. System start time is at k_0, after a disturbance occurs and parameter g is changed from positive to negative.

5.3.3 Trajectory Walkthrough for $g < 0$

Here, we describe a scenario on system Σ_3 that can result in the beginning of unstable oscillations. Suppose an adversary gains access to and installs malware in the communication system that remotely sends parameters to the inverters. The malware logic could, for example, send a negated inverter controller gain g when any of the inverter voltages suddenly change substantially ($|v_i[k+1] - v_i[k]| > 0.6\varepsilon$), and the voltage lands far from v^{ref} ($|v_i[k+1] - v^{ref}| > 0.6\varepsilon$). Such an attack is dangerous because the trigger by external voltage event(s) conceals the time when the cyber *breach* occurred, which could be much earlier than the parameter negation.

Follow along with Fig. 5.6. Suppose shortly before time k_0 some external event(s), such as a fault or effect from the transmission grid, causes the voltages to shift abruptly. Suppose the voltage shifts increase v^{diff}, make v_2 an undervoltage, and triggers the negation of the inverter parameter g. See [102] for power flow examples of this voltage shift on realistic circuits. We are interested in what happens after the system Σ_3 start time of k_0. From k_0 to k_1: at k_0 we have $f_2 < 0$ while $f_1 = 0$, so inverter2 actuates several times, each time causing v_2 to get further from the deadband. For k_1 to k_2: the LTC2 delay is complete so LTC2 taps, fixing the v_2 undervoltage but making v_1 an overvoltage. For k_2 to k_3: the inverter1 actuates several times, each time causing v_1 to get further from the deadband. For k_3 to

k_4: the LTC1 delay is complete so LTC1 taps, fixing the v_1 overvoltage but making v_2 an undervoltage again. At k_4 we have $f_2 < 0$ while $f_1 = 0$ which was the case for k_0, so we have completed one quasi-periodic oscillation. In future sections we show how these oscillations continue.

5.3.4 Single Inverter Action Preliminaries

In this section we present some properties of inverter actions between LTC taps to prepare for later proofs.

Suppose inverter i is acting during a time interval $[k \ ... \ k+N]$. Define the change in $v_j \in \mathbb{R}^1$ due to the inverter's action as $\Delta v_j^{inv}(\boldsymbol{X}_{ij}, k+N, k, v_i[k]) \coloneqq v_j[k+N] - v_j[k] \in \mathbb{R}^1$. Δv_j^{inv} can be thought of as the projection of inverter's actuation onto the v_j axis of the (v_i, v_j) space. Occasionally we omit some of the four parameters from Δv^{inv} when they are not relevant.

Assumption 8. *(Bounds on LTC and inverter action)*
$\bar{v}_L + \Delta v_i^{inv}(\boldsymbol{X}_{ii}, k+N, k, v_i[k]) < 2\varepsilon$ *for* $v_i[k] \in W$*, and* $\forall k, N$.

This assumption implies that $\bar{v}_L < 2\varepsilon$ and $\Delta v_i^{inv}(\boldsymbol{X}_{ii}, k+N, k, v_i[k]) < 2\varepsilon$ for $v_i[k] \in W$, and $\forall k, N$. The Assumption is reasonable because $\bar{v}_L$ is typically significantly less than ε, and Δv^{inv} imparting a voltage change of close to 2ε would require unreasonably large combinations of circuit impedance and inverter capacity.

Recall the voltage update equation (5.8) $\boldsymbol{v}[k+1] = \boldsymbol{v}[k] - \boldsymbol{XG}(\boldsymbol{v}[k] - \boldsymbol{v}^{ref})$. The inverter acts $N_1 \coloneqq \text{floor}(d_{L1}/d_{inv})$ times if after the interval $[k \ ... \ k+N_1]$ the LTC1 taps, or $N_2 \coloneqq \text{floor}(d_{L2}/d_{inv})$ times if after $[k \ ... \ k+N_2]$ LTC2 taps. The i^{th} row of (5.8) implies that node i's voltage is

$$v[k+1] = v[k] + \chi(v[k] - v^{ref}) \ \in \mathbb{R}^1, \tag{5.14}$$

and each other voltage on the network is given by

$$v[k+1] = v[k] + \eta\chi(v[k] - v^{ref}) \ \in \mathbb{R}^1 \tag{5.15}$$

from substituting (5.11) into (5.8). Now consider the accumulation of (5.8) for $N = N_1$ or $N = N_2$ timesteps:

$$\boldsymbol{v}[N+k] = (I - \boldsymbol{XG})^N \boldsymbol{v}[k] + \sum_{r=0}^{N-1} (1 - \boldsymbol{XG})^r (\boldsymbol{XGv}^{ref}). \tag{5.16}$$

The j^{th} row of (5.16) gives an expression for Δv_j^{inv} in terms of the parameters v^{ref}, g, χ,and N:

$$\Delta v_j^{inv}(\boldsymbol{X}_{ij}, k+N, k, v_i[k], g) = v_j[N+k] - v_j[k] \tag{5.17}$$

$$= ((1-\chi g)^N - 1)v[k] + \sum_{r=0}^{N-1} (1-\chi g)^r (\boldsymbol{X}_{ij} g v^{ref}). \tag{5.18}$$

Remark 4. *(Remarks about Δv_i^{inv} $\forall$ $i = 1, 2$)*

1. *Because* $\Delta v_i^{inv} < 2\varepsilon$ *from Assumption 8,* $\Delta v_i^{inv}(\boldsymbol{X}_{ii}, k+1, k)$ *has the same sign for* $k = 0...N$*.*
2. *If* $g > 0$*,* $sign\{\Delta v_i^{inv}(v_i[k])\} = -sign\{v_i[k] - v^{ref}\}$*.*
3. *If* $g < 0$*,* $sign\{\Delta v_i^{inv}(v_i[k])\} = sign\{v_i[k] - v^{ref}\}$*.*

The first item establishes that each inverter actuates in the same direction between LTC taps. The second (third) items establish that when $g > 0$ ($g < 0$), the inverters push the voltage toward (away) from the deadband.

Lemma 7. *(Δv^{inv} is a homogeneous function) The coupling effect of a single inverter actuating at node i on the voltage at node j is damped by a factor of η. That is,* $\Delta v_j^{inv}(\boldsymbol{X}_{ij}, k+N, k, v_i[k]) = \eta \Delta v_i^{inv}(\boldsymbol{X}_{ii}, k+N, k, v_i[k])$*.*

5.3.5 Partitioning W in State Space when $g < 0$

In this section we will partition W into D, W_g, W_b, W_o, based on the possible trajectories from starting the system in each region. We use a similar process to Section 5.2.3. The W_b region will be when both voltages are above or below the deadband. In that case, both inverters act between LTC taps, and from Assumption 8 oscillations cannot occur. Then W_o will be where only one inverter acts between taps, and is close enough to D for oscillations to occur. An oscillation would begin with an inverter pushing the voltages further from the deadband (Remark 4 #3) until an LTC tap towards the deadband and overshoots it. Therefore, the boundary of W_o comes from the states v where after inverter action(s) and an LTC tap the state is within the deadband edge:

$$v_1 + r_1 - \bar{v}_L < v^+ \tag{5.19a}$$
$$v_2 + r_2 - \bar{v}_L < v^+ \tag{5.19b}$$
$$v_1 + r_1 + \bar{v}_L > v^- \tag{5.19c}$$
$$v_2 + r_2 + \bar{v}_L > v^-. \tag{5.19d}$$

Function r is the inverters' change in v before an LTC taps:

$$r_1 \coloneqq \Delta v_1^{inv}(\chi, N_1, v_1) + \Delta v_1^{inv}(\boldsymbol{X}_{12}, N_1, v_2) \tag{5.20a}$$
$$r_2 \coloneqq \Delta v_2^{inv}(\boldsymbol{X}_{12}, N_1, v_1) + \Delta v_2^{inv}(\chi, N_1, v_2). \tag{5.20b}$$

Note that r depends on both v_1 and v_2, but when only one inverter acts, one term in each of (5.20a) and (5.20b) zeros out, causing eqs. (5.19a) to (5.19d) to depend on only v_1 *or* v_2.

We can now define the state space regions as

$$\begin{aligned}
W_o =&\{(v_1, v_2) \in W : \\
&(v_1 \in M(D, v_1^* - v^+) \text{ and } v_2 \in D), \qquad (5.21a)\\
&\text{or } (v_2 \in M(D, v_2^* - v^+) \text{ and } v_1 \in D)\},\\
W_b =&\{(v_1, v_2) \in W : \\
&(v_1, v_2 > v^+, v_2 \leq v_1, (5.19a) \text{ holds}),\\
&\text{or } (v_1, v_2 > v^+, v_2 > v_1, (5.19b) \text{ holds}), \qquad (5.21b)\\
&\text{or } (v_1, v_2 < v^-, v_2 > v_1 (5.19c) \text{ holds}),\\
&\text{or } (v_1, v_2 < v^-, v_2 \leq v_1, (5.19d) \text{ holds})\},
\end{aligned}$$

and W_g is what remains of W. That is, $W_g = W \setminus (D \cup W_o \cup W_g$. The v_1^* and v_2^* in (5.21a) are the v_1 and v_2 when (5.19a) and (5.19b) are set to be equalities. The W_o region definition is the same as that of the 2-LTC system Σ_1 (5.5), with the distinction that equations (5.19) have the additional r term.

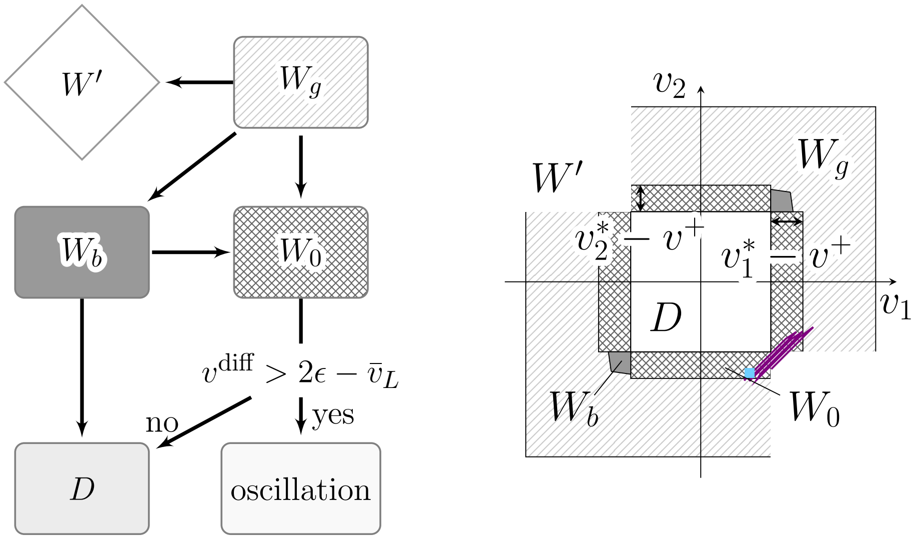

Figure 5.7: State space behavior of the four-device system Σ_3 when $g < 0$. ***Left:*** State transition diagram, indicating the possible behavior of trajectories. ***Right:*** State space partitioned into regions based on trajectory behavior. Example trajectory of device hunting is plotted, where the blue square marks the initial condition.

Fig. 5.7 shows these state space regions as well as the possible transitions between regions. The trajectory of Fig. 5.6 is plotted on Fig. 5.7 with a blue square marker for the IC. Observe that the trajectory oscillates until eventually leaving W. In addition to the possible transitions for system Σ_1 in Fig. 5.3, this system has: $W_b \to W_g$, $W_o \to W_b$, and $W_o \to W_b$ since the inverter pushes voltages away from D.

When the IC is in W_g or W_b, there may exist a $k_0 > 0$ where the full state vector $x[k_0] = [0, 0, 0, v_1[0], v_2[0]]^\top$. Because Σ_3 is time-invariant, the Fig. 5.7 regions apply to any $x[k_0]$ where $x[k_0] = x[0]$. For example, the system IC could be in W_g then later have $x[k_0] \in W_o$, after which point the behavior would be the same as if the system started in W_o.

5.3.6 Conditions for Oscillations to Begin when $g < 0$

In this section we consider trajectories where $\boldsymbol{v}[k_0] \in W_o$. As illustrated in Fig. 5.7, W_o is comprised of four disjoint regions. If hunting occurs in the lower region of W_o ($f_1 = 0$ while $f_2 < 0$), the hybrid system mode sequence (MS) that creates one period of oscillation is $\alpha_1 := \{m50, m10, m60, m50, m40, m70\}$ after omitting the increment mode ($m80$) for brevity. Similarly, let α_2, α_3, and α_4 be the oscillation sequences when the IC is in the upper, left, and right-hand regions of W_o, respectively.

Lemma 8. *(Basis step for oscillations) Consider system Σ_3 with $g < 0$. When $f_1 = 0$ while $f_2 < 0$, necessary and sufficient conditions for completing one oscillation period starting at time k_0 are*

$$v_1[k_0] + \eta\Delta v_2^{inv}(\chi, k_0 + N_2, k_0, v_2[k_0]) > v^- \tag{5.22a}$$

$$v[T_1] > v^- \tag{5.22b}$$

$$v[T_1] + \eta\Delta v_1^{inv}(\chi, k_0 + N_1, k_0, v[T_1]) < v^+ \tag{5.22c}$$

$$v[T_2] + \Delta v^{inv}(\chi, k_0 + N_1, k_0, v[T_2]) - \bar{v}_L < v^+ \tag{5.22d}$$

where $v[T_1] = v_2[k_0] + \Delta v_2^{inv}(\chi, k_0 + N_2, k_0, v_2[k_0]) + \bar{v}_L$, and $v[T_2] = v_1[k_0] + \eta\Delta v_2^{inv}(\chi, k_0 + N_2, k_0, v_2[k_0]) + \bar{v}_L$.

Proof. Follow along with Fig. 5.6. We will express sequence α_1 in terms of the system voltage trajectories. For the IC, $v_2[k_0]$ is an undervoltage and $v_1[k_0]$ in the deadband. Inverter2 responds to the v_2 undervoltage, but due to $g < 0$ it decreases both voltages. To prevent inverter2 from pushing both voltages below the deadband, we require that

$$v_1[k_0] + \Delta v_1^{inv}(\boldsymbol{X}_{12}, k_0 + N_2, k_0, v_2[k_0]) > v^-.$$

Next, with the persisting v_2 undervoltage, LTC2 taps which increases both voltages. To create overshoot so that v_1 has an overvoltage, we require that

$$v_2[k_0] + \Delta v_2^{inv}(\boldsymbol{X}_{22}, k_0 + N_2, k_0, v_2[k_0]) + \bar{v}_L > v^-.$$

Inverter1 responds to the v_1 overvoltage, but due to $g < 0$ it increases both voltages. To prevent inverter1 from pushing both voltages above the deadband, we require that

$$v[T_1] + \Delta v_2^{inv}(\boldsymbol{X}_{12}, k_0 + N_1, k_0, v_1[T_2]) < v^+.$$

With the persisting v_1 overvoltage, LTC1 taps which decreases both voltages. To create overshoot so that v_2 becomes an undervoltage, we require that

$$v[T_2] + \Delta v_1^{inv}(\boldsymbol{X}_{11}, k_0 + N_1, k_0, v_1[T_2]) - \bar{v}_L < v^+.$$

Finally, we substitute equation (5.11) into all above equations and apply Lemma 7 to the first and fourth equation, giving the conditions in the lemma statement. □

5.3.7 Showing Oscillations Continue when $g < 0$

Next we show that once the MS α_1 occurs, the next MS will be α_1 while $v \in W_o$. The same process can be applied to the other MS α_2, α_3, and α_4.

Define $m[k_i]$ as the mode that system Σ_3 is in at time k_i. Across each α_1 MS, v^{diff} increases. We will prove that in the next section, but note that as a result the voltage that is outside D gets further from $\boldsymbol{v}^{ref}$ across each α_1 MS. Next, consider the following condition:

$$v_1^{inv}(k_5, k_4, v_1[k_4]) + \Delta v_1^{inv}(k_3, k_2, v_1[k_2]) > 0 \tag{5.23}$$

Lemma 9. *(Induction step for oscillations) Consider system Σ_3 with $g < 0$. Assuming condition* (5.23) *and Assumption 7 holds, if the system completes MS α_1, the MS α_1 will repeat.*

Proof. Use Fig. 5.6 to follow along. $m[k_4]$: at k_0 inverter2 actuates and $m[k_0] = m50$ so $v_2[k_0] \notin D$. Because v_2 gets further from $\boldsymbol{v}^{ref}$, $v_2[k_4] < v_2[k_0]$, so $v_2[k_4] \notin D$ too. From Assumption 7, $v_1[k_4]$ cannot be outside D, so $v_1[k_4] \in D$. Thus inverter2 actuates at k_4 and $m[k_4] = m50$.

$m[k_5]$: Because $g < 0$, inv2 actuating ($m[k_4] = m50$) will keep $v_2 \notin D$. If the inverter's coupling effect on v_1 is strong enough, even though $v_1[k_4] \in D$, v_1 could go below the deadband by the time of k_5. By Assumption 8, the inverter actions summed with an LTC tap are not large enough for this. Thus at k_5, v_1 is still inside D and v_2 is still outside D. So at k_5 LTC2 taps up and $m[k_5] = m30$.

$m[k_6]$: The LTC2 tap may not overshoot the deadband at k_6. If (5.23) does not hold, then $v_1[k_6] \in D$, by Assumption 7, $v_2[k_6] \in D$ too, and the system stays in the deadband. If (5.23) does hold, inverter1 actuates and $m[k_4] = m50$. $m[k_7]$: Assumption 8 disallows v_2 from going above D (like how in $m[k_5]$ it disallows v_1 from going below D). Thus at k_7, v_2 is still inside D and v_1 is still outside D. So at k_7 LCT1 taps down and $m[k_7] = m20$. □

Lemma 10. *(Oscillations grow) If system Σ_3 with $g < 0$ has oscillations, v^{diff} increases after each oscillation period.*

Let s_1 be the set of $(v_1[k_0], v_2[k_0])$ where basis conditions (5.22) hold. The sets of conditions that correspond to sequences α_2,α_3, and α_4 are derived with the same process as the Lemma 8 proof, and we call their corresponding sets s_2, s_3, and s_4. Then we define

$$S := (\bigcup_{i=1,\dots,4} s_i) \in W_o \tag{5.24}$$

which is the only voltage region where oscillations can begin. Note that with the Δv^{inv} parametrized form (5.18), S can be represented by purely the variables listed in Table 5.1.

Theorem 5. *(Stability when $g < 0$) Define T_1 as the first instant where $v[T_1] \in D$, and define T_2 as the first instant where $v[T_2] \in W'$. When $g < 0$, $\boldsymbol{v}[k_0] \in S$ is necessary but not sufficient for system Σ_3 to exhibit growing oscillations starting at time k_0. These oscillations terminate either at time T_1 or T_2.*

Proof. Lemma 8 (basis step) establishes that (5.22) are necessary for on period of oscillations to occur. By Lemma 9 (induction step), the system continues to oscillate after the first oscillation period. Lemma 10 establishes that the oscillations grow, so the system will eventually land in D or outside W. □

Theorem 5 implies that when $g < 0$, the only way for Σ_3 to exhibit oscillations is when $\boldsymbol{v}[k_0] \in S$, where S is defined in (5.24). To use this theorem, engineers would choose control parameters such that $S = \emptyset$. Further, if each device has a copy of all control parameters, they can reject incoming parameter updates when $S \neq \emptyset$.

5.4 Case Studies

In this section, we validate the stability conditions derived above through numerical experiments with realistic parameter settings. We project the derived parameter conditions onto two-dimensional spaces to demonstrate important relationships between device operating parameters. Then we discuss initial ideas for extending the mathematical formulations to circuits with more than four devices.

5.4.1 Plots in the Parameter Space

In this section we use MATLAB's MPT toolbox to plot set S (5.24) in the (v_1, v_2) space and examine its implications on the ratio of the device control delays. Recall that S is the only voltage region where oscillations can begin, and includes the projection of basis conditions (5.22) onto the (v_1, v_2) space.

In Fig. 5.8 we plot S on the (v_1, v_2) space, and validate that S in the right panel of Fig. 5.8 is indeed a subset of W_o from (5.21a), as both sets have width of 0.0095 pu. Observe that some corners of W_o are not included in S because trajectories that start there leave W before completing an oscillation period. We also observe that in the right panel of Fig. 5.8 where oscillations can grow, the area of S is smaller compared to when oscillations are damped in the left panel of Fig. 5.8. It is relieving that the regions where dangerous oscillations could occur are narrow.

Next we examine the appropriate timescale separation between the inverters and LTC1 for system Σ_3 when $g < 0$. Because $N_1 = \text{floor}(d_{L1}/d_{inv})$ and N_1 enters Δv^{inv} as the exponent

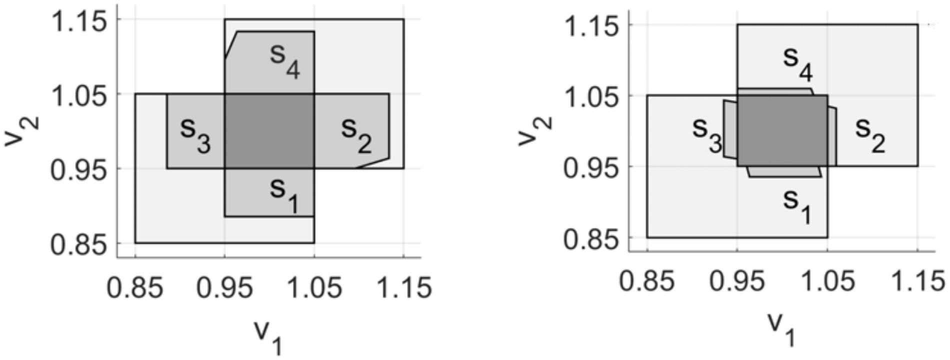

Figure 5.8: Plot of set W (light gray), set S (medium gray), and set D (dark gray) in the (v_1, v_2) space using default parameters in Table 5.1. ***Left:*** State space regions when $g = 0.5$. ***Right:*** State space regions when $g = -0.3$.

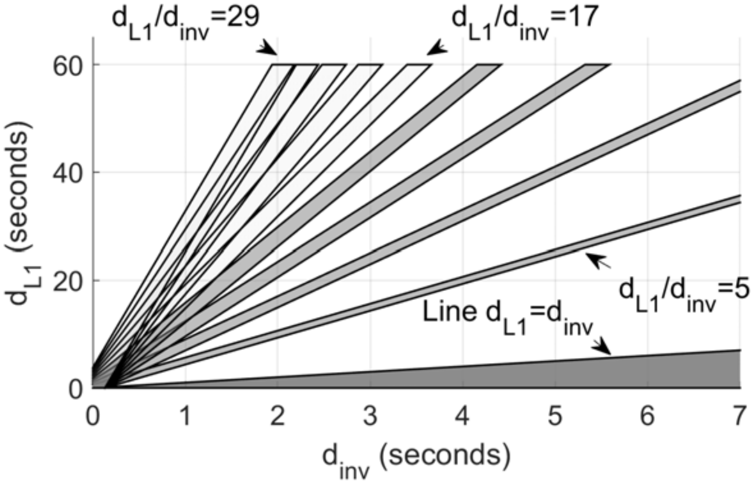

Figure 5.9: Plot of system Σ^3 when $g < 0$ in the (d_{L1}, d_{inv}) space, where the remaining parameters are in 5.1. Each line represents delay ratio d_{L1}/d_{inv}. Hunting is impossible $(S = \emptyset)$ for ratios marked in light gray, and possible $(S \neq \emptyset)$for ratios marked in dark gray.

(see (5.18)), Each fixed N_1 represents the slope of a line through the origin on the (d_{L1}, d_{inv}) space. As such, varying d_{L1} and d_{inv} such that N_1 is fixed will not change the S region on $(v1, v2)$. Therefore, rather than iterate over the (d_{L1}, d_{inv}) in a meshgrid, we compare the area of set S for lines corresponding to different N_1 values.

We set all variables except $v_1[k_0]$ and $v_2[k_0]$ to the defaults in Table 5.1. Instead of $d_{L1} = 30$ and $d_{L2} = 40$, which have a ratio of $\frac{4}{3}$, we set $N_2 = \frac{4}{3}N_1$ since $\frac{N_2}{N_1} = \frac{d_{L2}}{d_{L1}}$. We vary N_1 from 5 to 29. For each N_1 value, if $S = \emptyset$, then hunting oscillations are impossible for

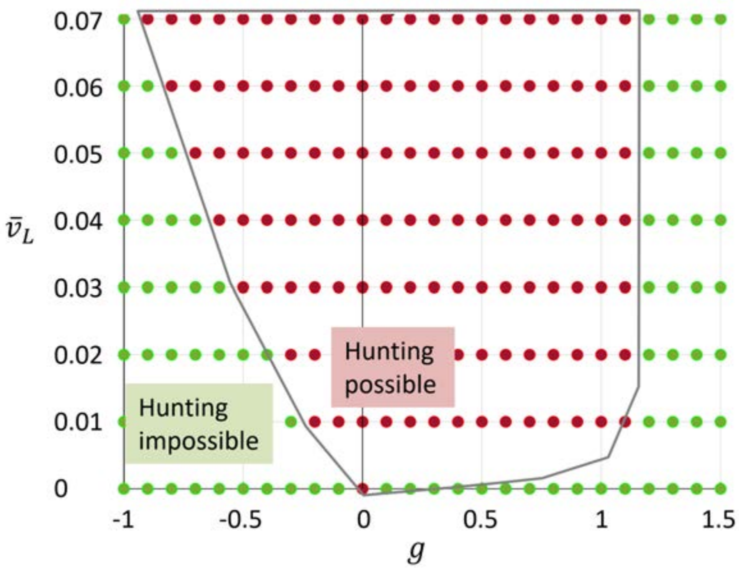

Figure 5.10: Plot of whether the system Σ^3 is guaranteed against hunting or not the $(g, \bar{v}_L)$ space, where the remaining parameters are in 5.1. Hunting is impossible ($S = \emptyset$) when the magnitude of g is large enough compared to $\bar{v}_L$.

all $\boldsymbol{v}[k_0] \in W$, and we mark the line with slope N_1 as light gray in Fig. 5.9. Conversely, if $S \neq \emptyset$ then the N_1 line is dark gray. The line $d_{inv} = d_{L1}$ is also marked to only allow the $d_{inv} < d_{L1}$ from Table 5.1. We observe that $N_1 = 17 = \text{floor}(d_{L1}/d_{inv})$ is the borderline case where hunting is impossible. For example, if the inverters have a 3-second delay, the substation LTC needs at least a 51-second delay to prevent hunting for all IC in W.

Finally, we focus on the relationship between inverter parameter g and the LTC parameter $\bar{v}_L$. These parameters are important to analyze because they may be capable of being adjusted more often than the delay parameters. We set all variables except g and $\bar{v}_L$ to the defaults in Table 5.1, and sample reasonable parameter ranges of $\bar{v}_L \in (0, 0.07)$ and $g \in (-1, 1.5)$. We observe that hunting is possible ($S \neq \emptyset$) when $\bar{v}_L$ is large compared to the magnitude of g, which is expected since the oscillatory behavior originates from LTC actions (see Fig 5.4). Additionally, for sufficiently positive g (around $g > 1.2$), the system is guaranteed to not exhibit hunting for any $\bar{v}_L$. The hunting boundary in the figure is exponential in nature because the change in voltage due to inverter actions is an exponential function of g (see (5.18)), and the LTC tap voltage $\bar{v}_L$ imparts a direct change in voltage in the same or opposing direction.

5.4.2 Grids with More than Four Devices

Radial distribution grids are typically tree graph networks whose root is the substation (see Chapter 2 section 2.1.2). Each node has one or more *branch(es)*, where each branch is a tree graph network connected to that node's edge(s). Suppose that there is at most one LTC and at most two actively controlled inverters on each branch b of the root node, as shown in Fig. 5.11. Then the combination of each branch with the root node comprises a system of the substation LTC, the LTC on the branch, and two inverters on the branch. We can characterize each system as Σ_3 and setup conditions to prevent oscillations separately using the methodology of section 5.3. The conditions across all branches must be jointly satisfied, but because the substation LTC is common to all subsystems, as b grows the number of parameter variables grows by $3b + 1$ instead of $4b$.

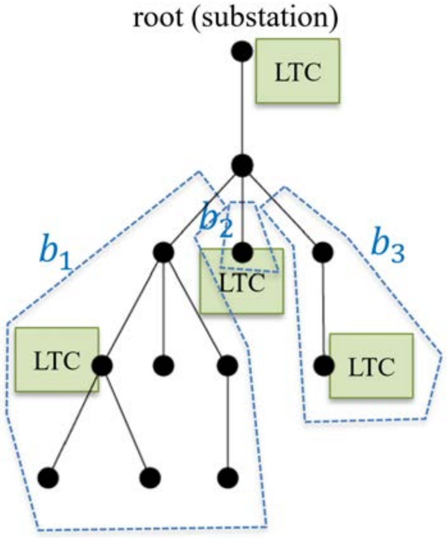

Figure 5.11: Example radial distribution grid, indicating the three branches associated with the root node of the graph.

5.5 Conclusion

We have presented a novel hybrid system model for LTCs with inverters on radial distribution circuits. Leveraging the system dynamics, we have derived conditions on the control parameters to guarantee against voltage oscillations created by device hunting. The conditions inform the design of appropriate parameters, such as the minimal timescale separation of control delays between LTCs and inverters. The conditions also provide the foundation for implementing onboard certificates that guard against malicious firmware updates of control parameters.

Chapter 6

Principles and Future Work

In the final chapter of this thesis, we summarize key concepts presented in this thesis and present further research directions. Then we describe key principles synthesized from the work and describe a vision for device controls in industry. Many of the ideas about industry have been inspired by conversations with distribution operators at real utilities.

6.1 Future Work:

6.1.1 Externally Defined Communication Networks

Distribution grids can benefit greatly from coordination among DERs, but currently have limited communication and computational capabilities. For a given set of DERs, there are a variety of reasons why each DER may not have access to measurements from all other DERs through communication channels. For example, there can be restrictions from geographic distance, privacy concerns, and differing ownership. We saw in Chapter 3 how a set of feedback controllers could be designed to accommodate any given communication limitations or requirements. Specifically, the analysis tools do not make any assumptions about where the DERs are sited relative to the voltage sensors, nor about what set of measurements each DER can access. As a result, the derived stability regions generalize across possible communication networks. However, since the system stability is characterized by a given impedance model, given locations of DERs and sensors, and given communication requirements, changes to any of these items affect the system stability. For example, we proved that the addition of any DER-sensor pair increases the system stability, while the removal of a pair decreases system stability (Chapter 3 Proposition 1). As a result, the gains of all controllers need to be updated whenever the system changes, including cases of DER malfunctioning and disconnection.

Naturally, future work would have each DER adaptively update its controller gains. That way, when the grid network topology changes, DER communication is lost, or DERs disconnect, the system maintains stability automatically without needing to be re-designed.

Adaptive control is a well-studied area of control theory literature where each device updates a control policy as a function of the mismatch between estimated measurements from an internal model and measurements from the real system. Several works have applied adaptive control to distribution grid voltage mitigation [53,103], but it would remain important for the control design to accommodate any externally defined communication network. In addition to allowing DER to incorporate measurements from any subset of sensors, a communication-agnostic control approach could be designed to handle other communication irregularities, including measurement delay and measurement loss.

6.1.2 Ranges of Operating Parameters

Over the last few decades, a large number of DERs have been deployed behind-the-meter DERs, such as solar PV. These devices are operated with a total focus on reducing the customer's net energy bill. Unfortunately this customer-centric operation can adversely impact the power quality of the distribution grid, for example by increasing voltage volatility and creating reverse power flow. Naturally then, it's important to incorporate objectives by both customers and grid operators into computing DER power set-points. One way to do this, as we saw in Chapter 3, is to compute ranges of stable operating parameters for each DER. The range captures the objective of grid operators to regulate voltages and power flows, while giving customers the freedom to adjust the DER's responsiveness to grid issues to improve their own economic outcomes. In a future where customers will be compensated not only for pure power output, but also for modulation of power to improve grid reliability, the weight of these preferences will often fluctuate. Future work would focus on algorithms to perform real-time parameter adjustment within the given range to maximize economic outcomes. The adjustment would include the latest literature on BTM optimization of batteries, and expand on the example given in section 3.5.1. Also we would seek polytopic geometry methods to widen the parameter ranges, for example by identifying the parameters that cause degeneracy of the stability polytope or form a *critical cluster* (as seen in [61]).

6.1.3 Reachability during Ride-Through Events

Region of Attraction

In Chapter 4, we were interested in abnormal voltage situations where following a large-signal disturbance the voltage recovers slowly. We assumed that the system operating point directly after the large-signal disturbance occurs is in a stable region associated with the equilibrium point of one per unit, to focus on a system comprised of the controller dynamics and the small-signal fluctuations from devices not under our control. If modeled with total fidelity, real distribution grids would be represented as highly nonlinear time-varying dynamical systems with multiple equilibria. As such, the large-signal disturbance could push the voltage into an oscillatory operating region, as demonstrated in [104] where motor loads are modeled with nonlinear dynamics. In future work we would determine the region of attraction around the

1pu equilibrium to characterize the boundary that guarantees against the system entering an oscillatory state. Then we would have operating states where the reachability analysis of Chapter 4 provides fast-recovery guarantees, and operating states where the system has dangerous oscillations. One could then focus on the dangerous case of oscillatory behavior around other equilibria and draw inspiration from the analysis of oscillations in Chapter 5 that investigates whether DERs could reduce the oscillations or return the system to the safe 1pu region of attraction.

Designing for Reachability

In Chapter 4, we have an autonomous system, where the control law (4.5) is chosen and applied to create a close loop system. The reachability analysis determines the full set of initial conditions whose trajectories can arrive at the safe set using the given control law. A natural extension is to design a control law rather than assess a selected one. That is instead of computing a series of invariant sets,

$$\mathcal{O} = \{x \subset \mathcal{X} \Rightarrow x(t) \in \mathcal{O} \ \forall t \in \mathbb{N}^+\} \tag{6.1}$$

we could compute control invariant sets.

$$\mathcal{C} = \{x \subset \mathcal{X} \Rightarrow \exists u(t) \in \mathcal{U} \mid f(x(t), u(t)) \in \mathcal{C} \ \forall t \in \mathbb{N}^+\} \tag{6.2}$$

Control invariant sets are computed for systems subject to external inputs. They determine the set of initial states for which there exists a controller that results in the system meeting all constraints on the input and state. Because all control invariant sets are invariant sets, the computed control invariant sets would be larger, and can help one design the control policy at each step of the trajectory calculation.

6.1.4 Stability of Systems with Load-Tap Changers and Inverters

In Chapter 5, we demonstrated how a distribution circuit model, composed of two LTCs and two inverter devices, can create voltage oscillations even with reasonable choices of control parameters. Though hunting among LTCs has been observed by utilities since the 1980s [93, 94] and was modeled as a hybrid system in the 2007 paper [94], the investigation and prevention of hunting between LTCs and inverters is a novel problem. As a result, many future directions extend the small-scale system of devices comprised of relatively simple dynamical equations examined in Chapter 5. For example, in Chapter 5 the grid's loads were assumed to be static constant power loads, which did not impact the system's dynamics matrix. In reality, the transient behavior of dynamic loads might be slow enough to interact with LTC and inverter dynamics, especially during abnormal voltage circumstances where motor loads stall and can cause oscillating voltages on their own [104]. Another avenue for exploration is to explore parameter relationships that guarantee against oscillations for grids with *many* devices. In Chapter 5 we describe the initial formulation for how one could decompose an arbitrarily-sized distribution network into a group of sub-systems coupled by the substation LTC (see Figure 5.11). From there, it would be important to compare how the parameter relationships become more conservative for larger grid systems. For example, with appropriate parameter default values we found the ratio of timescale separation between LTCs and inverters to be at least 17 (see Figure 5.9). With many devices that required timescale separation is likely to grow. Finally, in the case where undamped oscillations occurred, we described how the triggering event for the oscillations could be a cyberattack scenario where an abrupt change in voltages is followed by the negation of the inverter controller parameter. We did preliminary experimental work to identify examples of power injections that result in these kinds of voltage shifts, but in future work we would supplement these results with a derivation of a set of 'dangerous' power injections. That way, there would be better context for the kinds of real grid disturbances — such as faults, cloud cover, and disconnection of load — that enable the dangerous oscillation case.

6.2 Principles and Recommendations:

6.2.1 Principles for Good Device Controls

There are many approaches to designing and operating devices, such as DERs and voltage regulation equipment, on distribution grids. Rather than advocating for specific approaches, in this section we identify a few important principles that should inform the selection and implementation of an approach. Device control strategies should:

i. provide an immediate response to disturbances or model error

ii. provide guarantees against dangerous behavior

iii. not require extensive computation and communication

iv. provide transparency into decision making

For (i), a disturbance is any change in the state of a system as a result of an external trigger. On distribution grids disturbances can include faults, sudden changes in load or solar PV, and voltage regulation equipment. Yet disturbances are likely to become more pronounced as more active devices operated by different entities are installed on distribution grids. As a result, real-time responsiveness of device controls is critical to preserving safe operation of the grid at all times. Throughout this thesis, we demonstrated how feedback control laws — control logic where an action is taken as a direct function of measurements — provide this kind of immediate response to disturbances. Certain implementations of distributed optimal power flow (OPF) may also enable DERs to respond appropriately to disturbances [13,56,59]. Specifically, in feedback-based distributed optimization, the process of solving the optimization problem via steepest descent iterations is directly executed as feedback, ensuring that the system is driven in the right direction instead of stalling each time an optimization problem is being solved .

For (ii), it is important to use proofs and closed-form analytical expressions to guarantee against dangerous behavior. Reliable and safe electricity is seen by many as a basic need, and sometimes a basic right. Therefore, one of the most important priorities in grid operation is to preserve the safety of the grid. In electric grid research, it can be more valuable to prove a dangerous scenario cannot occur than to simulate many possibilities and check for the presence of any dangerous scenarios. In this thesis, we adopted stability and reachability analysis techniques to guarantee against control behavior that is unstable (Chapter 3), prohibitively slow (Chapter 4), and oscillatory (Chapter 5) that is validated with (but does not require) system simulation. The techniques expressed system behavior without the need for direct simulation. Optimization-based approaches can directly prescribe safe grid operation with optimization solutions, but as optimization problems require significant computation time, there continues to be a danger of the grid becoming unsafe between optimization iterations.

Item (iii) is explained in the next section, section 6.2.3.

For (iv), a single control framework can operate over 800,000 micro-inverter devices at once [105]. That much consolidated influence on the power grid reminds us that any adopted control approach needs to have transparency into the *how* and *why* of the decision-making. In an obvious sense, this idea promotes item (ii) where we can better guarantee against and respond to dangerous behavior. Additionally, this transparency promotes the adoption of control approaches by industry and helps diagnose problematic behavior when unforeseen conditions change. Some optimization formulations focus too much on how to formulate and solve the optimization problem, without demonstrating the methodology or providing details on why the solution is reasonable. For example, several works such as [25,26] compute optimal DER or sensor placement using mixed-integer optimization formulations, but do not show and discuss the actual placement results themselves. That kind of discussion is important for understanding trends and building intuition about what factors make a good placement. Having this transparency was a core reason we investigated DER and sensor placement from a dynamical systems perspective in Chapter 3.3.2. Optimization approaches could also achieve this transparency using optimization sensitivity analysis, which computes how variations of particular optimization parameters affect the optimal solution.

6.2.2 Theoretical Validity of Stability Guarantees

The previous section described the importance of using dynamical system models to prove theoretical guarantees against dangerous behavior. However, these guarantees are only as valid as the models they are derived from. Because the power grid is highly complex, models of grid phenomena are never 100% valid with respect to the real world (i.e. all models are somewhat wrong). Simplifications are often made to tractably and clearly solve problems, which introduces error between the system model and the real physical phenomena. Therefore, scrutinizing sources of modeling error and quantifying model fidelity is critical to supplementing dynamical system analyses.

One major source of model error in solving power systems problems includes linearizing dynamical equations so that certain analyses (such as the eigenvalue analysis in Chapter 3) can be performed. For example, in this thesis, the non-linearity for representing DER saturation was not modeled when designing the DER control so that eigenvalue analysis could be performed on the linear model. Optimization formulations also typically include linearization so that solving the problem can be tractable and so that the solution is trustworthy (local optima may not be global optima). Model error can also come from assumed uniformity of device models. Specifically, in this thesis we model all DERs as power injectors, but DERs have further constraints and preferences that vary by DER type. Optimization problems, notably, do have more flexibility in accommodating variations in equation structures that are associated with different resource models. Finally, model error can come from assuming a timescale separation between types of physical phenomena so that certain grid devices or loads are omitted from the model.

Now that we have established several common sources of modeling error in power systems, it is important to quantify the error, and assess the validity of proven guarantees given the modeling error. In Chapter 3 we used the spectral radius of the dynamics matrix to quantify how relatively how close a candidate controller design is to instability. These relative stability metrics enable grid operators to choose the controller design that is the most robust to modeling error among the candidates, which may also coincide with the best voltage regulation performance. Admittedly, because those stability metrics are relative, they do not indicate whether the true model error encountered can be overcome by the chosen controller. Some analyses do incorporate a model of the uncertainty to convey how well the control design performs with the model error. For example, in Chapter 4 we performed a reachability analysis to guarantee that the designed DER control overcomes a second-wise uncertainty model. The uncertainty model captured 95% of voltage uncertainty observed from real μPMU data. An uncertainty model can also be incorporated into the controller design itself, which is a core concept in stochastic and robust control. As a greater variety of devices begin to act on the same timescale in distribution grids, robust and stochastic approaches may become an important aspect of future work. We note that these complex, model-dependent approaches should be reserved for applications where the uncertainty is so significant and difficult to represent that uncertainty metrics and analyses are insufficient for achieving good control performance.

6.2.3 Aligning Research with Real Grid Problems and Capabilities

The electric power industry is in a time of great flux. There is an explosion of available data, but it is accessible by different entities and typically needs extensive processing and interpolation. Many active devices are being installed and operated, but there continues to be limited coordination between devices and awareness of their real-time status. As a result, theoretical methods in control theory, optimization theory, graph theory, and machine learning can fail when met with the limitations of real grids, especially distribution grids. For example, currently (year 2022) virtual power plant companies encounter significant solar PV and load forecasting errors, which may cause control algorithms that hinge on net load predictions to fail or be highly sub-optimal. Real grid limitations vary by region and are rapidly evolving, so it is critically important for researchers to frequently ask about such limitations to industry players, including grid operators (utilities), DER management system (DERMS) companies, aggregator (sometimes called virtual power plant) companies, and grid data analysis companies. For each, researchers should understand their basic business model, what assets they own and operate, what models they have access to, and what data they have access to. We note that though utilities have similar organizational structures — having distribution operations, distribution planning, transmission, and billing departments — they vary greatly by their adoption of modern grid devices, grid network model fidelity, and interest in customer autonomy. Therefore, it is important to talk to many different utilities to develop approaches that address common challenges while generalizing across variations in needs and capabilities.

Once researchers calibrate their approaches with industry needs and capab ilities, they should package their algorithms and analyses into standalone tools that can be downloaded and run independently (for example through Github repositories such as [106]). Moreover, the tools should have detailed visual components that demonstrate the inner progression of the analyses or illustrate relationships between important design factors (promotes principle (iv)). By having these visual properties, the tools may be more easily adopted by grid operators. Tools can also be more compelling if they mimic existing tools that are already in use. For example, our stability analysis tool in 3 mimicked the aesthetics of hosting capacity maps. See the related thesis [107] for a detailed exploration of visual data analysis tools for grid operators.

6.2.4 Vision for DER Controls on Distribution Grids in Industry

Given the approaches implemented and principles learned in this thesis, we have recommendations for different industry players as it pertains to control on distribution grids.

First, we have recommendations for policy makers and utilities. While power electronics, computation, and data analysis technologies have advanced significantly in the last few decades, market mechanisms and regulatory policies for distribution grid operation have lagged behind. We recommend that policy makers create new markets dedicated to competition between DERs that reward them for alleviating distribution and transmission level issues. To accompany this market, ISOs and utilities should work together to create a distribution service marketplace, where utilities and/or aggregators coordinate device actions to efficiently deliver power and increase distribution grid reliability and resiliency. Many utilities have deferred the responsibility of owning and monitoring DERs to aggregators and customers, but the utility's objective of maintaining safe grid operation may be at odds with the customer's objective of producing DER power that reduces their energy bill. Therefore, utilities should own and operate their own DERs, with the help of DERMS companies, that directly service their priorities, much like legacy voltage regulation equipment already do. If utilities do not have the time, expertise, or institutional buy-in to purchase their own DERs, utility commissions should incentivize or mandate them to do so.

Secondly, we have recommendations for DER aggregator companies. These companies work with utilities and customers to install DERs at customer sites. They offer customers a lower electricity bill and historically were paid by utilities to perform demand response, where aggregators shed customers' loads during a grid event. For example, a grid event could be during the one or two hour time of daily peak load. The challenge with this business model is the control is coarse and delegated to utilities and customers. To leverage the proliferation of other DERs (solar, batteries, EVs, water heaters), aggregators should *take back their control*. That is, when deploying DER integration programs, they should set up contract agreements and implement control logic to modulate customer DER power outputs that optimize device operation across the day. This control setup will be rewarded when the DSO markets become established. In the meantime, aggregators should collect grid models and data to analyze grid impacts, so that when utilities can be compensated for reliability services in DSO markets, DER aggregators are ready to help provide those services.

Finally, we present a vision for the future of distribution grid operation, where a distribution service marketplace is governed by a distribution system operator (DSO). Background about the concept of DSOs can be found in [108].

During normal operation, the grid operator's goal is to efficiently operate the power grid and prevent the grid from having a grid event. Each DER should generally output whatever power that is available from the resource, with some modulation of the output in response to to small deviations in voltage or frequency. DERs should have some amount of communication with each other so that they can share power and contribute to power quality objectives together. The DER control algorithm could be a distributed OPF formulation if communication between all neighboring DERs is realizable, otherwise it could be a set of feedback controllers (see Chapter 3). We note that during normal operation, DER control would not require direct commands or measurements from utilities. Specifically, investing in real-time communication between every DER and the utility substation may not be worthwhile. Gathering performance data and compensating DERs for their services is not time critical, so can be handled over the internet without direct communication links. The result is that DERs *autonomously* respond to voltage and power flow issues, saving money for customers, and defer the cost of infrastructure upgrades for utilities. Regions where there are not many active devices, and severe barriers to setting up communication may be particularly suitable to have DERs operate only in normal mode.

When normal operation is insufficient in addressing grid imbalance, voltage, or other issues, we envision a different process for grid services that is captured by Fig 6.1, which has been adapted from a chart presented by Camus Energy [109]. During a grid event, such as during adverse weather conditions or when the transmission system is highly constrained, the goal of the grid operator is to prevent damage to equipment and actively mitigate the grid event so that the grid returns to normal operation. The DSO is the central decision maker, which is typically a utility but could also be a third-party coordinator. The DSO monitors

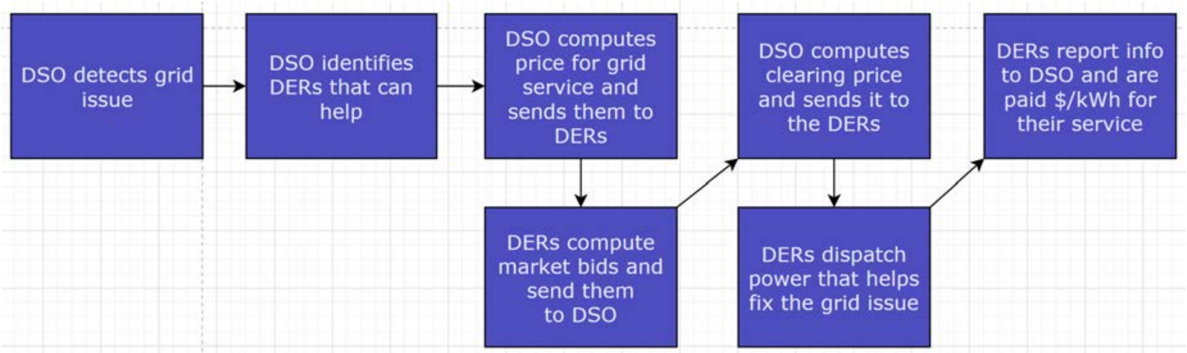

Figure 6.1: Flowchart of the suggested response by the DSO and DERs during a transmission or distribution grid event.

real-time measurements and forecasted demand and generation to detect a significant and persistent grid issue, such as an overloaded transformer, frequency drop, or voltage spike. When the issue is detected, the DSO computer identifies DERs that can be controlled (owned by utilities or customers), which need two way communication with the DSO. The DSO identifies what grid service is needed, and sends a price for power (real and/or reactive) to each DER. Depending on the pricing computation, the price can be location-dependent (as in D-LMP setups [110]) since power provided at different grid locations may have different capabilities to mitigate the grid issue. Each DER uses their given price to compute a bid for producing or consuming a certain amount of power, which is sent back to the DSO. The DSO runs an auction and sends the clearing price and accepted bids back to each DER. Finally, the DERs dispatch power according to accepted bids, which helps mitigate the grid issue. We note that the aforementioned process, from detecting a grid issue to DERs responding, needs to be done quickly, perhaps within a few seconds if the issue is severe (see Chapter 4). As a result, streamlining this real-time process is a top priority for many aggregators today. We predict that as aggregators and DERMS companies develop further, DER coordination between customers and aggregators will evolve into a system that achieves the carbon reduction goals, grid reliability goals, and energy savings goals sought by its participants.

Bibliography

[1] R. El Helou, D. Kalathil, and L. Xie, “Communication-free Voltage Regulation in Distribution Networks with Deep PV Penetration,” in *2020 Hawaii International Conference on System Sciences*, Jan. 2020.

[2] PingThings, *PMU data archives from a distribution grid with community solar.* Available: `https://ni4ai.org/datasets/2/`, Accessed 20 Jul. 2021.

[3] F. Milano, F. Dörfler, G. Hug, D. J. Hill, and G. Verbič, “Foundations and Challenges of Low-Inertia Systems (Invited Paper),” in *2018 Power Systems Computation Conference*, pp. 1–25, June 2018.

[4] Australian Energy Market Operator Limited, *Technical Integration of Distributed Energy Resources: Improving DER capabilities to benefit consumers and the power system. A report and consultation paper (2019).* Available: `https://www.aemo.com.au/-/media/Files/Electricity/NEM/DER/2019/Technical-Integration/Technical-Integration-of-DER-Report.pdf`, Accessed 13 Aug. 2022.

[5] S. Karagiannopoulos, P. Aristidou, A. Ulbig, S. Koch, and G. Hug, “Optimal planning of distribution grids considering active power curtailment and reactive power control,” in *2016 IEEE Power and Energy Society General Meeting*, pp. 1–5, July 2016.

[6] “IEEE Standard for Interconnection and Interoperability of Distributed Energy Resources with Associated Electric Power Systems Interfaces,” *IEEE Std 1547-2018 (Revision of IEEE Std 1547-2003)*, pp. 1–138, Apr. 2018.

[7] M. Taibbi, *Gridlocked by the power grid: Why Hawaii’s solar energy industry is at a crossroads*, 2015. Available: `https://www.pbs.org/newshour/show/gridlocked-power-grid-hawaiis-solar-energy-industry-crossroads`, Accessed 13 Aug. 2022.

[8] R. Seguin, J. Woyak, D. Costyk, J. Hambrick, and B. Mather, “High-Penetration PV Integration Handbook for Distribution Engineers,” 2016.

[9] K. Turitsyn, P. Šulc, S. Backhaus, and M. Chertkov, “Distributed control of reactive power flow in a radial distribution circuit with high photovoltaic penetration,” in *IEEE PES General Meeting*, pp. 1–6, 2010.

[10] X. Liang and J. Hofman, “Trip Curves and Ride-Through Evaluation for Power Electronic Devices in Power System Dynamic Studies,” *IEEE Transactions on Industry Applications*, vol. 52, pp. 1290–1296, Mar. 2016.

[11] M. T. A. Kusko, *Power Quality in Electrical Systems.* Available: http://www.powerqualityworld.com/2011/04/ansi-c84-1-voltage-ratings-60-hertz.html, Accessed 13 Aug. 2022.

[12] X. Zhou, M. Farivar, Z. Liu, L. Chen, and S. H. Low, “Reverse and Forward Engineering of Local Voltage Control in Distribution Networks,” *IEEE Transactions on Automatic Control*, vol. 66, pp. 1116–1128, Mar. 2021.

[13] N. Li, G. Qu, and M. Dahleh, “Real-time decentralized voltage control in distribution networks,” in *2014 52nd Annual Allerton Conference on Communication, Control, and Computing (Allerton)*, pp. 582–588, Sept. 2014.

[14] S. M. N. R. Abadi, A. Attarha, P. Scott, and S. Thiébaux, “Affinely Adjustable Robust Volt/Var Control for Distribution Systems With High PV Penetration,” *IEEE Transactions on Power Systems*, vol. 36, pp. 3238–3247, July 2021.

[15] Y. P. Agalgaonkar, B. C. Pal, and R. A. Jabr, “Distribution voltage control considering the impact of pv generation on tap changers and autonomous regulators,” *IEEE Transactions on Power Systems*, vol. 29, no. 1, pp. 182–192, 2014.

[16] B. A. Robbins, C. N. Hadjicostis, and A. D. Domínguez-García, “A Two-Stage Distributed Architecture for Voltage Control in Power Distribution Systems,” *IEEE Transactions on Power Systems*, vol. 28, pp. 1470–1482, May 2013.

[17] A. von Meier, E. L. Ratnam, K. Brady, K. Moffat, and J. Swartz, “Phasor-Based Control for Scalable Integration of Variable Energy Resources,” *Energies*, vol. 13, p. 190, Jan. 2020.

[18] W. De Carvalho, E. L. Ratnam, L. Blackhall, and A. Von Meier, “Optimization-based operation of distribution grids with residential battery storage: Assessing utility and customer benefits,” *IEEE Transactions on Power Systems*, pp. 1–1, 2022.

[19] S. Hashemi and J. Østergaard, “Efficient Control of Energy Storage for Increasing the PV Hosting Capacity of LV Grids,” *IEEE Transactions on Smart Grid*, vol. 9, pp. 2295–2303, May 2018.

[20] K. Baker, A. Bernstein, E. Dall’Anese, and C. Zhao, “Network-Cognizant Voltage Droop Control for Distribution Grids,” *IEEE Transactions on Power Systems*, vol. 33, pp. 2098–2108, Mar. 2018.

[21] M. E. Baran and I. M. El-Markabi, “A multiagent-based dispatching scheme for distributed generators for voltage support on distribution feeders,” *IEEE Transactions on Power Systems*, vol. 22, no. 1, pp. 52–59, 2007.

[22] T. Gönen, *Electric Power Distribution System Engineering*. USA: CRC Press, 3rd ed., 2014.

[23] K. Christakou, M. Paolone, and A. Abur, “Voltage control in active distribution networks under uncertainty in the system model: A robust optimization approach,” *IEEE Transactions on Smart Grid*, no. 6, 2018.

[24] B. A. Robbins, H. Zhu, and A. D. Domínguez-García, “Optimal Tap Setting of Voltage Regulation Transformers in Unbalanced Distribution Systems,” *IEEE Transactions on Power Systems*, vol. 31, Jan. 2016.

[25] R. S. Al Abri, E. F. El-Saadany, and Y. M. Atwa, “Optimal Placement and Sizing Method to Improve the Voltage Stability Margin in a Distribution System Using Distributed Generation,” *IEEE Transactions on Power Systems*, vol. 28, pp. 326–334, Feb. 2013.

[26] H. Nazaripouya, Y. Wang, P. Chu, H. R. Pota, and R. Gadh, “Optimal sizing and placement of battery energy storage in distribution system based on solar size for voltage regulation,” in *IEEE Power and Energy Society General Meeting*, pp. 1–5, July 2015.

[27] M. Baran and F. Wu, “Network reconfiguration in distribution systems for loss reduction and load balancing,” *IEEE Transactions on Power Delivery*, vol. 4, no. 2, pp. 1401–1407, 1989.

[28] M. Farivar, L. Chen, and S. Low, “Equilibrium and dynamics of local voltage control in distribution systems,” in *52nd IEEE Conference on Decision and Control*, pp. 4329–4334, Dec. 2013.

[29] M. D. Sankur, R. Dobbe, A. v. Meier, E. M. Stewart, and D. B. Arnold, “Optimal voltage phasor regulation for switching actions in unbalanced distribution systems,” in *2020 IEEE Power and Energy Society General Meeting*, pp. 1–5, 2020.

[30] R. Dobbe, D. Arnold, S. Liu, D. Callaway, and C. Tomlin, “Real-Time Distribution Grid State Estimation with Limited Sensors and Load Forecasting,” in *2016 ACM/IEEE 7th International Conference on Cyber-Physical Systems*, pp. 1–10, Apr. 2016.

[31] P. Kundur, *Power System Stability and Control*. New York, NY, USA: McGraw-Hill, 3rd ed., 1994.

[32] H. Xu, A. D. Domínguez-García, V. V. Veeravalli, and P. W. Sauer, “Data-Driven Voltage Regulation in Radial Power Distribution Systems,” *IEEE Transactions on Power Systems*, vol. 35, pp. 2133–2143, May 2020.

[33] H. Xu, A. D. Domínguez-García, V. V. Veeravalli, and P. W. Sauer, “Data-driven voltage regulation in radial power distribution systems,” *IEEE Transactions on Power Systems*, vol. 35, no. 3, pp. 2133–2143, 2020.

[34] J. Zhang, Z. Chen, C. He, Z. Jiang, and L. Guan, “Data-driven-based optimization for power system var-voltage sequential control,” *IEEE Transactions on Industrial Informatics*, vol. 15, no. 4, pp. 2136–2145, 2019.

[35] J. Swartz, E. Ratnam, T. Roberts, and A. von Meier, “Local phasor-based control of DER inverters for voltage regulation on distribution feeders,” in *press, IEEE Green Technologies Conference*, Apr. 2020.

[36] D. Wang, K. Meng, X. Gao, J. Qiu, L. L. Lai, and Z. Y. Dong, “Coordinated Dispatch of Virtual Energy Storage Systems in LV Grids for Voltage Regulation,” *IEEE Transactions on Industrial Informatics*, vol. 14, pp. 2452–2462, June 2018.

[37] S. Pahwa, D. Weerasinghe, C. Scoglio, and R. Miller, “A complex networks approach for sizing and siting of distributed generators in the distribution system,” in *2013 North American Power Symposium*, pp. 1–5, Sept. 2013.

[38] A. Eggli, S. Karagiannopoulos, S. Bolognani, and G. Hug, “Stability Analysis and Design of Local Control Schemes in Active Distribution Grids,” *IEEE Transactions on Power Systems*, vol. 36, pp. 1900–1909, May 2021.

[39] J. Seuss, M. J. Reno, R. J. Broderick, and S. Grijalva, “Improving distribution network pv hosting capacity via smart inverter reactive power support,” in *IEEE Power and Energy Society General Meeting*, pp. 1–5, Jul. 2015.

[40] J. Rocabert, A. Luna, F. Blaabjerg, and P. Rodríguez, “Control of power converters in ac microgrids,” *IEEE Transactions on Power Electronics*, vol. 27, no. 11, pp. 4734–4749, 2012.

[41] N. Pogaku, M. Prodanovic, and T. C. Green, “Modeling, analysis and testing of autonomous operation of an inverter-based microgrid,” *IEEE Transactions on Power Electronics*, vol. 22, no. 2, pp. 613–625, 2007.

[42] S. D’Arco, J. A. Suul, and O. B. Fosso, “Small-signal modelling and parametric sensitivity of a virtual synchronous machine,” in *2014 Power Systems Computation Conference*, pp. 1–9, 2014.

[43] U. Markovic, O. Stanojev, P. Aristidou, E. Vrettos, D. Callaway, and G. Hug, "Understanding small-signal stability of low-inertia systems," *IEEE Transactions on Power Systems*, vol. 36, no. 5, pp. 3997–4017, 2021.

[44] B. Zhang, A. D. Domínguez-García, and D. Tse, "A local control approach to voltage regulation in distribution networks," in *2013 North American Power Symposium (NAPS)*, pp. 1–6, Sept. 2013.

[45] A. Singhal, V. Ajjarapu, J. Fuller, and J. Hansen, "Real-time local volt/var control under external disturbances with high PV penetration," *IEEE Transactions on Smart Grid*, vol. 10, pp. 3849–3859, Jul. 2019.

[46] P. Jahangiri and D. C. Aliprantis, "Distributed Volt/VAr Control by PV Inverters," *IEEE Transactions on Power Systems*, vol. 28, pp. 3429–3439, Aug. 2013.

[47] *PMUs and synchrophasor data flows in North America*. Available: `https://www.naspi.org/node/387`, Accessed 31 Dec. 2020.

[48] S. Bu, L. G. Meegahapola, D. P. Wadduwage, and A. M. Foley, "Stability and Dynamics of Active Distribution Networks with D-PMU Technology: A Review," *IEEE Transactions on Power Systems*, pp. 1–1, 2022.

[49] A. von Meier, E. Stewart, A. McEachern, M. Andersen, and L. Mehrmanesh, "Precision micro-synchrophasors for distribution systems: A summary of applications," *IEEE Transactions on Smart Grid*, vol. 8, pp. 2926–2936, Nov. 2017.

[50] J. Swartz, B. Wais, E. Ratnam, and A. von Meier, "Visual Tool for Assessing Stability of DER Configurations on Three-Phase Radial Networks," in *2021 IEEE PowerTech*, pp. 1–6, June 2021.

[51] J. Swartz and A. von Meier, "The Impact of Three-phase Impedances on the Stability of DER Systems," in *2021 North American Power Symposium*, Nov. 2021.

[52] J. Swartz, E. Ratnam, A. Bhardwaj, and A. von Meier, "Gershgorin Disc-based Voltage Stability Regions for DER Siting and Control in Distribution Grids," *submitted to IEEE Transactions on Power Systems*, Dec. 2022. arXiv:2212.06275.

[53] A. Singhal, V. Ajjarapu, J. Fuller, and J. Hansen, "Real-time local volt/var control under external disturbances with high PV penetration," *IEEE Transactions on Smart Grid*, vol. 10, pp. 3849–3859, July 2019.

[54] L. Wang, F. Bai, R. Yan, and T. K. Saha, "Real-Time Coordinated Voltage Control of PV Inverters and Energy Storage for Weak Networks With High PV Penetration," *IEEE Transactions on Power Systems*, May 2018.

[55] G. Cavraro and R. Carli, "Local and Distributed Voltage Control Algorithms in Distribution Networks," *IEEE Transactions on Power Systems*, vol. 33, pp. 1420–1430, Mar. 2018.

[56] S. Bolognani, R. Carli, G. Cavraro, and S. Zampieri, "On the Need for Communication for Voltage Regulation of Power Distribution Grids," *IEEE Transactions on Control of Network Systems*, vol. 6, pp. 1111–1123, Sept. 2019.

[57] Z. Yang, Y. Li, and J. Xiang, "Coordination Control Strategy for Power Management of Active Distribution Networks," *IEEE Transactions on Smart Grid*, vol. 10, pp. 5524–5535, Sept. 2019.

[58] S. Nowak, Y. C. Chen, and L. Wang, "Distributed Measurement-Based Optimal DER Dispatch With Estimated Sensitivity Models," *IEEE Transactions on Smart Grid*, vol. 13, pp. 2197–2208, May 2022.

[59] H. Zhu and H. J. Liu, "Fast Local Voltage Control Under Limited Reactive Power: Optimality and Stability Analysis," *IEEE Transactions on Power Systems*, vol. 31, pp. 3794–3803, Sept. 2016.

[60] S. M. N. R. Abadi, A. Attarha, P. Scott, and S. Thiébaux, "Affinely Adjustable Robust Volt/Var Control for Distribution Systems With High PV Penetration," *IEEE Transactions on Power Systems*, vol. 36, pp. 3238–3247, July 2021.

[61] A. Gorbunov, J. C.-H. Peng, J. W. Bialek, and P. Vorobev, "Identification of Stability Regions in Inverter-Based Microgrids," *IEEE Transactions on Power Systems*, pp. 1–1, 2021.

[62] R. A. Horn and C. R. Johnson, *Matrix Analysis.* USA: Cambridge University Press, 2nd ed., 2012.

[63] C.-T. Chen, *Linear System Theory and Design.* USA: Oxford University Press, Inc., 3rd ed., 1998.

[64] J.-L. Wu, "Design of Optimal Static Output Feedback Controllers for Linear Control Systems Subject to General Structural Constraints," *IEEE Transactions on Automatic Control*, vol. 67, pp. 474–480, Jan. 2022.

[65] F. Lin, M. Fardad, and M. R. Jovanovic, "Augmented Lagrangian Approach to Design of Structured Optimal State Feedback Gains," *IEEE Transactions on Automatic Control*, vol. 56, pp. 2923–2929, Dec. 2011.

[66] H. Chen, W. Zhang, J. Lian, and A. J. Conejo, "Robust distributed volt/var control of distribution systems," in *2017 IEEE 56th Annual Conference on Decision and Control (CDC)*, pp. 6321–6326, Dec. 2017.

[67] Z. Cheng, J. Ma, X. Li, M. Tomizuka, and T. H. Lee, “Second-Order Non-Convex Optimization for Constrained Fixed-Structure Static Output Feedback Controller Synthesis,” *IEEE Transactions on Automatic Control*, pp. 1–1, 2022.

[68] V. Katewa and F. Pasqualetti, “Minimum-gain Pole Placement with Sparse Static Feedback,” *IEEE Transactions on Automatic Control*, pp. 1–1, 2020.

[69] J. Ma, S. Chen, N. Kamaldin, C. S. Teo, A. Tay, A. Al Mamun, and K. K. Tan, “Integrated mechatronic design in the flexure-linked dual-drive gantry by constrained linear–quadratic optimization,” *IEEE Transactions on Industrial Electronics*, vol. 65, no. 3, pp. 2408–2418, 2018.

[70] S. Boyd and L. Vandenberghe, *Convex Optimization.* Cambridge University Press, 2004.

[71] *IEEE Distribution Test Feeders.* Available: http://sites.ieee.org/pes-testfeeders/resources/, Accessed 7 Nov. 2020.

[72] *IEEE Distribution Test Feeders.* Available: `http://sites.ieee.org/pes-testfeeders/resources/`, Accessed 12 Aug. 2021.

[73] S. Riaz and P. Mancarella, “Modelling and Characterisation of Flexibility From Distributed Energy Resources,” *IEEE Transactions on Power Systems*, vol. 37, no. 1, pp. 38–50, 2022.

[74] Y. Wang, X. Ai, Z. Tan, L. Yan, and S. Liu, “Interactive dispatch modes and bidding strategy of multiple virtual power plants based on demand response and game theory,” *IEEE Transactions on Smart Grid*, vol. 7, no. 1, pp. 510–519, 2016.

[75] K. Yoon, D. Choi, S. H. Lee, and J.-W. Park, “Optimal placement algorithm of multiple dgs based on model-free lyapunov exponent estimation,” *IEEE Access*, vol. 8, pp. 135416–135425, 2020.

[76] K. Vasudevan, C. S. R. Atla, and K. Balaraman, “Improved state estimation by optimal placement of measurement devices in distribution system with ders,” in *2015 International Conference on Power and Advanced Control Engineering (ICPACE)*, pp. 253–257, 2015.

[77] J. Seuss, M. J. Reno, R. J. Broderick, and S. Grijalva, “Improving distribution network PV hosting capacity via smart inverter reactive power support,” in *2015 IEEE Power Energy Society General Meeting*, pp. 1–5, July 2015.

[78] J. Swartz and A. von Meier, “Reachability analysis for controlling ders to mitigate disturbances in distribution grids,” in *2022 IEEE Innovative Smart Grid Technologies Conference*, pp. 1–5, 2022.

[79] C. P. U. Commission, *Electric Rule No. 21 - Generating Facility Interconnections.* Available: `https://www.cpuc.ca.gov/Rule21/`, Accessed 12 Aug. 2021.

[80] M. Farivar, X. Zho, and L. Chen, "Local voltage control in distribution systems: An incremental control algorithm," in *2015 IEEE International Conference on Smart Grid Communications*, Nov. 2015.

[81] Y. Xu, Z. Y. Dong, R. Zhang, and D. J. Hill, "Multi-timescale coordinated voltage/var control of high renewable-penetrated distribution systems," *IEEE Transactions on Power Systems*, 2017.

[82] P. Gupta, K. Rahimi, R. Broadwater, and M. Dilek, "Importance of detailed modeling of loads/pv systems connected to secondary of distribution transformers," in *2017 North American Power Symposium*, 2017.

[83] A. Shahsavari, M. Farajollahi, E. M. Stewart, E. Cortez, and H. Mohsenian-Rad, "Situational awareness in distribution grid using micro-pmu data: A machine learning approach," *IEEE Transactions on Smart Grid*, vol. 10, no. 6, pp. 6167–6177, 2019.

[84] J. Ma, Y. V. Makarov, R. Diao, P. V. Etingov, J. E. Dagle, and E. De Tuglie, "The characteristic ellipsoid methodology and its application in power systems," *IEEE Transactions on Power Systems*, vol. 27, no. 4, pp. 2206–2214, 2012.

[85] S. Rakovic, E. Kerrigan, D. Mayne, and J. Lygeros, "Reachability analysis of discrete-time systems with disturbances," *IEEE Transactions on Automatic Control*, vol. 51, no. 4, pp. 546–561, 2006.

[86] R. J. Bravo, R. Yinger, S. Robles, and J. H. Eto, "FIDVR in distribution circuits," in *2013 IEEE Power Energy Society General Meeting*, 2013.

[87] R. Yan and T. K. Saha, "Investigation of Voltage Stability for Residential Customers Due to High Photovoltaic Penetrations," *IEEE Transactions on Power Systems*, vol. 27, pp. 651–662, May 2012.

[88] F. Borrelli, A. Bemporad, and M. Morari, *Predictive Control for Linear and Hybrid Systems.* USA: Cambridge University Press, 1st ed., 2017.

[89] J. Swartz, F. Celi, F. Pasqualetti, and A. Von Meier, "Parameter conditions to prevent voltage oscillations caused by ltc-inverter hunting on power distribution grids," in *2022 European Control Conference (ECC)*, pp. 1118–1125, 2022.

[90] M. Ahmed, R. Bhattarai, S. J. Hossain, S. Abdelrazek, and S. Kamalasadan, "Coordinated Voltage Control Strategy for Voltage Regulators and Voltage Source Converters Integrated Distribution System," *IEEE Transactions on Industry Applications*, July 2019.

[91] M. Chamana and B. H. Chowdhury, "Impact of Smart Inverter Control with PV Systems on Voltage Regulators in Active Distribution Networks," in *IEEE International Symposium on High-capacity Optical Networks and Emerging/Enabling Technologies*, Dec. 2014.

[92] M. Kraiczy, T. Stetz, and M. Braun, "Parallel Operation of Transformers With on Load Tap Changer and Photovoltaic Systems With Reactive Power Control," *IEEE Transactions on Smart Grid*, Nov. 2018.

[93] C. Smith, M. Redfern, and S. Potts, "Improvement in the Performance of On-load Tap Changer Transformers Operating in Series," in *2003 IEEE Power Engineering Society General Meeting*, July 2003.

[94] V. Donde and I. A. Hiskens, "Analysis of Tap-Induced Oscillations Observed in an Electrical Distribution System," *IEEE Transactions on Power Systems*, Nov. 2007.

[95] S. Sahoo, T. Dragičević, and F. Blaabjerg, "Cyber Security in Control of Grid-Tied Power Electronic Converters–Challenges and Vulnerabilities," *IEEE Journal of Emerging and Selected Topics in Power Electronics*, 2019.

[96] C. Roberts, S.-T. Ngo, A. Milesi, A. Scaglione, S. Peisert, and D. Arnold, "Deep Reinforcement Learning for Mitigating Cyber-Physical DER Voltage Unbalance Attacks," in *2021 American Control Conference*, May 2021.

[97] S. Mahdavi and A. Dimitrovski, "Integrated coordination of voltage regulators with distributed cooperative inverter control in systems with high penetration of dgs," in *2020 IEEE Texas Power and Energy Conference (TPEC)*, 2020.

[98] D. Mignone, G. Ferrari-Trecate, and M. Morari, "Stability and stabilization of piecewise affine and hybrid systems: an LMI approach," in *Proceedings of the 39th IEEE Conference on Decision and Control*, Dec. 2000.

[99] H. Lin and P. J. Antsaklis, "Stability and Stabilizability of Switched Linear Systems: A Survey of Recent Results," *IEEE Transactions on Automatic Control*, Feb. 2009.

[100] S. Lim and K. Chan, "Analysis of Hybrid Linear Parameter-varying Systems," in *Proceedings of the 2003 American Control Conference, 2003.*, June 2003.

[101] R. Decarlo, M. Branicky, S. Pettersson, and B. Lennartson, "Perspectives and results on the stability and stabilizability of hybrid systems," *Proceedings of the IEEE*, vol. 88, pp. 1069–1082, July 2000.

[102] B. Sachdev and J. Swartz, "Hunting simulator." `https://github.com/birkaransachdev/hunting-sims`, Accessed 10 Oct. 2022, Nov. 2021.

[103] S. A. U. Islam, E. L. Ratnam, A. Goel, and D. S. Bernstein, "Phasor-based adaptive control of a test-feeder distribution network: Application of retrospective cost adaptive control to the ieee 13-node test feeder," *IEEE Control Systems Magazine*, vol. 39, no. 4, pp. 56–74, 2019.

[104] R. Yan and T. K. Saha, "Investigation of voltage stability for residential customers due to high photovoltaic penetrations," *IEEE Transactions on Power Systems*, vol. 27, no. 2, pp. 651–662, 2012.

[105] I. Spectrum, *800,000 Microinverters Remotely Retrofitted on Oahu—in One Day*, Feb. 2015. Available: `https://spectrum.ieee.org/in-one-day-800000-microinverters-remotely-retrofitted-on-oahu`, Accessed 15 Aug. 2022.

[106] J. Swartz and B. Wais, "Visual tool for assessing stability of der configurations on three-phase radial networks." `https://github.com/jaimiosyncrasy/heatMap`, Accessed 10 Oct. 2022, May 2022.

[107] M. Bariya, *Applications of Time Synchronized Measurements in the Electric Grid*. PhD thesis, EECS Department, University of California, Berkeley, Aug 2021. Available: `http://www2.eecs.berkeley.edu/Pubs/TechRpts/2021/EECS-2021-196.html`, Accessed 21 August. 2022.

[108] *Rethinking California Distribution System Operations and Grid Services Markets for a High-DER future*. Available: `https://www.utilitydive.com/news/california-distribution-system-operations-distributed-energy-resources-DER-grid-services-markets/624376/`, Accessed 13 Oct. 2022.

[109] Camus Energy, *Webinar: DER Modeling and Distribution System Operations*, Apr. 2022. Available: `https://www.youtube.com/watch?v=HPbZ7UQvxR0`, Accessed 21 August. 2022.

[110] E. Ma, A. Lodder, S. Guo, S. Mortazavian, Y. Zhang, Z. Jamaludin, P. B. Madabhushi, D. Dias Oliveira, and W. Muneer, "Three-Phase Distribution Locational Marginal Pricing for Competitive Electricity Markets with Distributed Generators and Flexible Loads," in *2022 IEEE Power & Energy Society Innovative Smart Grid Technologies Conference (ISGT)*, pp. 1–5, Apr. 2022.

Chapter 7

Appendix

7.1 Proofs of all Lemmas and Theorems from Chapter 3

Proof of Lemma 1: From [63, Chapter 6.2], the controllable subspace is the range of the controllability matrix

$$\boldsymbol{W}_c = \begin{bmatrix} \boldsymbol{B} & | & \boldsymbol{AB} & | & ... & | & \boldsymbol{A}^{n-1}\boldsymbol{B} \end{bmatrix} \tag{7.1}$$

For our system, since $A = I$, $\boldsymbol{W}_c = [\boldsymbol{B} \mid ... \mid \boldsymbol{B}]$. By the construction of $\boldsymbol{B} \in \mathbb{R}^{2n\times d}$ (3.23c), $\Gamma_{2n}(\mathcal{D}) \in \mathbb{R}^{2n\times d}$ spans the range of $\boldsymbol{W}_c$. Then, since $A = I$, $\boldsymbol{W}_o = [\boldsymbol{C}^\top \mid ... \mid \boldsymbol{C}^\top]$. By the construction of $\boldsymbol{C} = \boldsymbol{T}^s$ (3.23c), $\boldsymbol{T}^s \in \mathbb{R}^{s\times 2n}$ spans the range of $\boldsymbol{W}_o$.

Proof of Lemma 2: By construction of $\boldsymbol{T}$, $\boldsymbol{TG} = (\boldsymbol{T}^s)^\top$, so $\bar{\boldsymbol{C}} = \boldsymbol{CTG} = \boldsymbol{T}^s(\boldsymbol{T}^s)^\top = I_s$ As a result, the reduced state vector output-readout map is $\boldsymbol{y} = \bar{\boldsymbol{C}}\bar{\boldsymbol{e}} = I_s\bar{\boldsymbol{e}}$. Because the output vector is the same for the original and reduced system, setting $\boldsymbol{y} = \boldsymbol{Ce} = \boldsymbol{T}^s\boldsymbol{e}$ equal to $\boldsymbol{y} = \bar{\boldsymbol{C}}\bar{\boldsymbol{e}} = \bar{\boldsymbol{e}}$ yields $\bar{\boldsymbol{e}} = \boldsymbol{T}^s\boldsymbol{e}$.

Proof of Lemma 3: First, we will show $\bar{\boldsymbol{B}}\boldsymbol{F}\bar{\boldsymbol{C}} = \boldsymbol{G}^\top\boldsymbol{T}^{-1}(\boldsymbol{BFC})\boldsymbol{TG}$. Substituting $\tilde{\boldsymbol{C}} = \boldsymbol{CT}$ into $\bar{\boldsymbol{C}} = \tilde{\boldsymbol{C}}\boldsymbol{G}$ gives $\bar{\boldsymbol{C}} = \boldsymbol{CTG}$. Substituting $\tilde{\boldsymbol{B}} = \boldsymbol{T}^{-1}\boldsymbol{B}$ into $\bar{\boldsymbol{B}} = \boldsymbol{G}^\top\tilde{\boldsymbol{B}}$ gives $\bar{\boldsymbol{B}} = \boldsymbol{G}^\top\boldsymbol{T}^{-1}\boldsymbol{B}$. Together, we have $\bar{\boldsymbol{B}}\boldsymbol{F}\bar{\boldsymbol{C}} = \boldsymbol{G}^\top\boldsymbol{T}^{-1}(\boldsymbol{BFC})\boldsymbol{TG}$.

Next, we show $\bar{\boldsymbol{F}} = \boldsymbol{F}\bar{\boldsymbol{C}}$. Substituting $\boldsymbol{y} = \bar{\boldsymbol{C}}\bar{\boldsymbol{e}}$ (3.28) into into $\boldsymbol{y}$ of $\boldsymbol{u} = -\boldsymbol{Fy}$ (3.24) gives $\boldsymbol{u} = -\boldsymbol{F}\bar{\boldsymbol{C}}\bar{\boldsymbol{e}}$. Then combining $\boldsymbol{u} = \bar{\boldsymbol{F}}\bar{\boldsymbol{e}}$ (3.29) with this result gives $-\boldsymbol{F}\bar{\boldsymbol{C}}\bar{\boldsymbol{e}} = \bar{\boldsymbol{F}}\bar{\boldsymbol{e}}$. Therefore, $\bar{\boldsymbol{F}} = \boldsymbol{F}\bar{\boldsymbol{C}}$

Finally, $\bar{\boldsymbol{H}} = \bar{\boldsymbol{B}}\bar{\boldsymbol{F}} = \bar{\boldsymbol{B}}\boldsymbol{F}\bar{\boldsymbol{C}} = \boldsymbol{G}^\top\boldsymbol{T}^{-1}(\boldsymbol{BFC})\boldsymbol{TG} = \boldsymbol{G}^\top\boldsymbol{T}^{-1}\boldsymbol{HTG}$.

Proof of Corollary 1: First we establish that $\boldsymbol{H}_{i\bar{p}} = 0$ for $i = 1...2n \; \forall \; \bar{p} \in \bar{\mathcal{S}}$: Considering the construction of matrix $\boldsymbol{C}$ in (3.23c), $\boldsymbol{C}_{i\bar{p}} = 0$ for $i = 1...s \; \forall \; \bar{p} \in \bar{\mathcal{S}}$. Thus with $\boldsymbol{H} = \boldsymbol{BFC}$, $\boldsymbol{H}_{i\bar{p}} = 0$ for $i = 1...2n \; \forall \; \bar{p} \in \bar{\mathcal{S}}$

From Lemma 3, we know $\bar{\boldsymbol{H}} = \boldsymbol{G}^\top\boldsymbol{T}^{-1}\boldsymbol{HTG}$. Then define $\tilde{\boldsymbol{H}} = \boldsymbol{T}^{-1}\boldsymbol{HT}$. Considering $\boldsymbol{T}$, $\tilde{\boldsymbol{H}}$ is a permutation of the rows and columns of $\boldsymbol{H}$ with the zero-columns of $\boldsymbol{H}$ collected on the right. It follows that $\bar{\boldsymbol{H}} = \boldsymbol{G}^\top \tilde{\boldsymbol{H}} \boldsymbol{G}$. Considering $\boldsymbol{G}$, the upper left $s \times s$ block of $\tilde{\boldsymbol{H}}$ is $\bar{\boldsymbol{H}}$:

$$\tilde{\boldsymbol{H}} = \left[\begin{array}{c|c} \bar{\boldsymbol{H}} & 0 \\ \hline \tilde{\boldsymbol{H}}_{12} & 0 \end{array}\right] \tag{7.2}$$

where the bottom-right diagonal block is $0 \in \mathbb{R}^{(2n-s)\times(2n-s)}$. Because $\tilde{\boldsymbol{H}}$ is block triangular, its eigenvalues are equal to the union of the diagonal-block eigenvalues. Because $\boldsymbol{H}$ and $\tilde{\boldsymbol{H}}$ are similar matrices, the eigenvalues of $\boldsymbol{H}$ and $\tilde{\boldsymbol{H}}$ are the same. Thus the eigenvalues of $\boldsymbol{H}$ are $2n - s$ zeros, and eig($\bar{\boldsymbol{H}}$).

Proof of Theorem 2:

First, we call the set of all $\lambda \in \mathbb{C}$ that are eigenvalues of a matrix $\boldsymbol{A}$ the *spectrum* of $\boldsymbol{A}$ and denote it with $\Lambda(\boldsymbol{A})$.

(i) From [63, Chapter 5.3], a system is exponentially stable if the state trajectory decays to zero and the trajectory is upper bounded by an exponential function. A discrete linear time-invariant system $x[k+1] = \boldsymbol{M}x[k]$ is exponentially stable iff the eigenvalues of $\boldsymbol{M}$ have magnitudes less than one. Let the pair (μ,υ) be an eigenvalue of $\bar{\boldsymbol{H}}$ and $(1-\bar{\boldsymbol{H}})$, respectively. By the spectral mapping theorem, $\upsilon = 1-\mu$. Thus with the given that $\mu \in \mathcal{B}(1+0j,1)$, then $\upsilon \in \mathcal{B}(0+0j,1) \leftrightarrow |\upsilon| < 1 \; \forall \upsilon \in \Lambda(1-\bar{\boldsymbol{H}})$. Then the close-loop system $\bar{\boldsymbol{e}}[k+1] = (\boldsymbol{I}-\bar{\boldsymbol{H}})\bar{\boldsymbol{e}}[k]$ (3.30) is exponentially stable.

(ii) From [63, Chapter 5.3], A system is stable in the sense of Lyapunov if x_k is bounded for all time $k \geq k_0$. A discrete linear time-invariant system $x[k+1] = \boldsymbol{M}x[k]$ is stable in the sense of Lyapunov iff two conditions hold: the eigenvalues of $\boldsymbol{M}$ have magnitudes less than or equal to one, and those equal to one are simple roots of the minimal polynomial of $\boldsymbol{M}$. Let the pair (κ,ζ) be an eigenvalue of $\boldsymbol{H}$ and $(1-\boldsymbol{H})$, respectively. For showing the first condition: from Corollary 1, $\kappa = \mu \; \forall \mu \in \Lambda(\bar{\boldsymbol{H}})$, or $\kappa = 0$ with algebraic multiplicity of $2n-s$. By the spectral mapping theorem, $\zeta = \upsilon \; \forall \upsilon \in \Lambda(1-\bar{\boldsymbol{H}})$, or $\zeta = 1$ with algebraic multiplicity of $2n-s$. From (i), $|\upsilon| < 1 \; \forall \upsilon \in \Lambda(1-\bar{\boldsymbol{H}})$, so the first condition is satisfied. For showing the second condition: the multiplicity of a root in a minimal polynomial is the smallest k such that the nullity of a matrix $\boldsymbol{M}$ satisfies $Null(\boldsymbol{M}-\lambda I)^k = n$, where n is the multiplicity of the repeated eigenvalue λ. Since the eigenvalues of $(\boldsymbol{I}-\boldsymbol{H})$ that are equal to one have algebraic multiplicity of $2n-s$, we want to show that $Null(\boldsymbol{I}-\boldsymbol{H}-1\cdot\boldsymbol{I}) = 2n-s$, or equivalently that $Null(\boldsymbol{H}) = 2n-s$. By the construction of $\boldsymbol{C}$ in (3.23c), for all $i = 1...2n$, $\boldsymbol{H}_{ij} = 0$ and for $j \in \bar{\mathcal{S}}$ notice that the j^{th} standard basis vectors e_j for $j \in \bar{\mathcal{S}}$ satisfy $\boldsymbol{H}e_j = 0e_j$, so belong to the null space of $\boldsymbol{H}$. Finally, with s defined as $|\mathcal{S}|$, $Null(\boldsymbol{H}) = 2n-s$. So (ii) is satisfied.

(iii) From Lemma 2, $\bar{\boldsymbol{e}} = \boldsymbol{T}^s\boldsymbol{e}$. This implies that $\bar{\boldsymbol{e}}$ is comprised of $\{e_p \; \forall p \in \mathcal{S}\}$. From (i), $\bar{\boldsymbol{e}}$ converges to zero exponentially, so e_p does too $\forall p \in \mathcal{S}$.

Proof of Theorem 3: From Theorem 2, we need to show the eigenvalues of $\bar{\boldsymbol{H}}$ are inside $\mathcal{B}(1+0j,1)$. We consider one row for each Gershgorin disc. If each of these Gershgorin discs are contained in $\mathcal{B}(1+0j,1)$ then by Theorem 1 the union of the Gershgorin discs (and thus all the eigenvalues) are inside $\mathcal{B}(1+0j,1)$. Since all elements of $\bar{\boldsymbol{H}}$ are real-valued, all Gershgorin disc centers are real-valued, so varying $\bar{\boldsymbol{H}}$ elements only causes the Gershgorin discs grow, shrink, and slide horizontally with centers fixed along the real axis. Thus necessary conditions for stability would keep the edges of each of the s Gershgorin discs, ($\phi_i + \gamma_i$,0) and ($\phi_i - \gamma_i$,0) $\forall i = 1, ..., s$, inside the edges of $\mathcal{B}(1+0j,1)$, which are at (0,0) and (2,0).

Proof of Proposition 1: Consider modifications of Σ_1. When an DER-sensor pair is added, two indices are added to $\mathcal{S}$, causing s to increase by two and matrix $\bar{\boldsymbol{H}} \in \mathbb{R}^{s\times s}$ gains two more rows and columns. The addition of two more rows results in evaluating two more Gershgorin discs in Theorem 3 that need to be in $\mathcal{B}(1+0j,1)$. The addition of two more columns results in the original Gershgorin discs becoming larger. The DER-sensor addition does not modify the original set of diagonal elements of $\bar{\boldsymbol{H}}$, so the original Gershgorin disc centers are unchanged. Together, the union of two more Gershgorin discs with original Gershgorin discs that have larger radii but have the same center makes $\rho_1^{ub}(\bar{\boldsymbol{H}})$ larger, so stability is reduced. By Lemma 1, $m(\boldsymbol{H}) = m(\bar{\boldsymbol{H}})$ so system Σ_1 has a decreased stability margin $m(\boldsymbol{H})$.

Then the converse, where an DER-sensor pair is removed, involves $\mathcal{S}$ losing two indices, $\bar{\boldsymbol{H}}$ having two fewer Gershgorin discs, and the original Gershgorin disc radii becoming smaller. The result Σ_1 having an increased stability margin $m(\boldsymbol{H})$.

Proof of Proposition 2:

Power-voltage sensitivity is given directly by a circuits resistance and reactances (3.5). We assume that on a given radial distribution circuit, every line segment has some positive quantity of resistance and reactance. Therefore, as the electrical distance $|\boldsymbol{Z}_{ij}|$ of a co-located ($i = j$) actuator is increased by placing it deeper into the network, $\boldsymbol{X}_{ii}$ and $\boldsymbol{R}_{ii}$ increases. As such, each unit of real or reactive power injection will change the voltage magnitude and phase angle more. In general we want high sensitivity to make the DER power injections meaningful.

For stability, observe that as $\boldsymbol{R}_{ii} \to \infty$ and $\boldsymbol{X}_{ii} \to \infty$, the inequalities (3.42a) or (3.42b) will eventually be violated. Graphically, as $\boldsymbol{X}_{ii}$ and $\boldsymbol{R}_{ii}$ increases, from (3.38) and (3.39) the associated Gershgorin disc center will shift to the right, and from (3.40) and (3.41) the other Gershgorin disc radii will increase. Eventually, the disc associated with $\boldsymbol{X}_{ii}$ and $\boldsymbol{R}_{ii}$ will exit on the right side of $\mathcal{B}(1+0j,0)$, making the system unstable. Thus if in (3.42a) and (3.42b) we fix controller gains $\bar{\boldsymbol{F}}$ and $\boldsymbol{X}_{ij}$ and $\boldsymbol{R}_{ij}$ for $i \neq j$, we have a condition on $\boldsymbol{X}_{ii}$ and $\boldsymbol{R}_{ii}$ for the maximum depth of location i to ensure stability of the system.

Proof of Proposition 3: By Lemma 1, the stability of Σ^1 is determined by $\bar{\boldsymbol{H}}$, so we focus on $\bar{\boldsymbol{H}}$ instead of $\boldsymbol{H}$. From Theorem 1, every element of $\bar{\boldsymbol{H}}$ is part of a Gershgorin disc center or radii, so we can look at (3.38), (3.39), (3.40), and (3.41). In each of these equations, i iterates over $\mathcal{S}_1$. By definition of $\mathcal{S}_1$ in (3.1), the $x_{i\ell}$ and $r_{i\ell}$ terms only select the rows of $\boldsymbol{X}$ and $\boldsymbol{R}$ that are associated with sensor nodes. No other impedances impact $\bar{\boldsymbol{H}}$. Similarly, ℓ iterates over $\mathcal{D}_1$. By definition of $\mathcal{D}_1$ in (3.1), the $x_{i\ell}$ and $r_{i\ell}$ terms only select the columns of $\boldsymbol{X}$ and $\boldsymbol{R}$ that are associated with DER nodes.

Proof of Proposition 4: (efficiency): Note that by definition of Z,

$$\boldsymbol{R}_{ij} = \min(\boldsymbol{R}_{ii}, \boldsymbol{R}_{jj}) \tag{7.3}$$

$$\boldsymbol{X}_{ij} = \min(\boldsymbol{X}_{ii}, \boldsymbol{X}_{jj}) \tag{7.4}$$

For instance 1, because $i = j$, $\boldsymbol{Z}_{ij} = \boldsymbol{Z}_{jj}$, so controller efficiency η^1 defined in (3.43) will be 1. For instance 2, $|\boldsymbol{Z}_{ij}| < |\boldsymbol{Z}_{ii}|$, so by (7.4), $\boldsymbol{Z}_{ij} = \boldsymbol{Z}_{jj}$, so $\eta^2 = 1$. For instance 3, $\boldsymbol{Z}_{ij} = \boldsymbol{Z}_{ii}$, so by (7.4) $|\boldsymbol{Z}_{jj}| > |\boldsymbol{Z}_{ij}|$. Thus $\eta^3 < 1$. Therefore, $\eta^1 = \eta^2 > \eta^3$.

(stability): Recall $\bar{\boldsymbol{H}} = \bar{\boldsymbol{B}}\bar{\boldsymbol{F}}$ with dense $\bar{\boldsymbol{B}}$ and $\bar{\boldsymbol{F}}$ having some given sparsity structure. With Theorem 1 applied to $\bar{\boldsymbol{H}}$, $\boldsymbol{X}_{ij}$ and $\boldsymbol{R}_{ij}$ contribute only to the j^{th} Gershgorin disc center and the $p \neq j$ Gershgorin disc radii. So $\boldsymbol{X}_{ij}$ and $\boldsymbol{R}_{ij}$ appear only in $\bar{\boldsymbol{H}}_{pj}$ for all $p = 1...s$. For instance 2, $\boldsymbol{R}_{ij} < \boldsymbol{R}_{ii}$ and $\boldsymbol{X}_{ij} < \boldsymbol{X}_{ii}$, so compared to instance 1 the j^{th} and $j + n^{th}$ Gershgorin disc center is shifted left, and the $p \neq (j, j+n)$ Gershgorin discs have reduced radii. The Gershgorin disc shifting has an inconclusive effect in the stability margin, so $m(\bar{\boldsymbol{H}}^2)$ may be greater or less than $m(\bar{\boldsymbol{H}}^1)$. For instance 3, $\boldsymbol{Z}_{ij} = \boldsymbol{Z}_{ii}$, so the j^{th} and $(j+n)^{th}$ Gershgorin disc center is the same as in instance 1. Since $\boldsymbol{Z}_{ij} = \boldsymbol{Z}_{ii}$, by (3.43) $|\boldsymbol{Z}_{jj}| > |\boldsymbol{Z}_{ij}|$, so the $p \neq (j, j+n)$ Gershgorin discs will have increased radii. If there are no other Gershgorin discs besides $(j, j+n)$, the radii will be the same compared to instance 1. Therefore, $m(\bar{\boldsymbol{H}}^1) \geq m(\bar{\boldsymbol{H}}^3)$.

7.2 Computing an Optimal Box inside Stability Polytope $\mathcal{F}$ from Chapter 3.5

$$\begin{aligned} \min_{\boldsymbol{f}^0 \in \mathbb{R}^y, \boldsymbol{w} \in \mathbb{R}^y} \quad & -\sum_{i=1}^{y} log(w_i) + \mu(||\boldsymbol{f}^0||_2 + ||\boldsymbol{f}^0 + \boldsymbol{w}||_2) \\ \text{s.t.} \quad & \boldsymbol{A}^+(\boldsymbol{f}^0 + \boldsymbol{\alpha} \cdot \boldsymbol{w}) \leq \boldsymbol{b}^+ \text{ for each } \boldsymbol{\alpha} \in \Psi \\ & \boldsymbol{f}^0_j \leq \frac{4}{x_{11}} \ \forall\ j = 1...y \\ & \boldsymbol{w} \geq 0 \end{aligned} \tag{7.5}$$

where $\boldsymbol{f}^0$ is the lower left corner of the hyperrectangle, and $\boldsymbol{w}$ is the vector of hyperrectangle widths in each dimension. Set Ψ is comprised of all 2^y possible combinations of a binary vector in $\mathbb{R}^y$. The inequality constraint enforces that every vertex of the hyperrectangle is inside $\mathcal{F}$. The allowable controller gain range (f^{min}, f^{max}) of the i^{th} DER is given by the projection of the hyperrectangle along dimension i. The weight parameter μ trades off between maximizing the gain ranges represented by widths w_i, and the minimizing the actuation effort represented by the distance of the corners of the rectangle $\boldsymbol{f}^0$ and $\boldsymbol{f}^0 + \boldsymbol{w}$ to the origin. That is, a smaller μ will grow the hyperrectangle but drive it away from the origin. A larger μ will result in smaller gain ranges and overall smaller gain values.

7.3 Minor Proofs of Lemmas from Chapter 5

Lemma 4 If $\bar{v}_L > 2\varepsilon$, system Σ_1 will have marginally stable oscillations for all time when any $v_1[0] \in M(D, c)$ or $v_2[0] \in M(D, c)$ where $c = \bar{v}_L - 2\varepsilon > 0$

Proof. If $v_1[0] \in M(D, c)$, LTC1 taps, causing $\bar{v}_L$ to overshoot the deadband of width 2ε and land outside D. After a delay d_{L1}, LTC1 will tap in the opposite direction, landing at the system IC. Then these actions repeat, causing v_1 and v_2 to oscillate with constant amplitude for all time. When $v_2[0] \in M(D, c)$ we get the same oscillatory behavior. □

Lemma 5. If $\bar{v}_L \leq 2\varepsilon$, $v[T] \in W_o$, and $v^{\text{diff}} < 2\varepsilon - \bar{v}_L$, system Σ_1 will have marginally stable oscillations starting at time T

Proof. First consider an IC in W_o (i.e. $T = 0$) where $v_2[0]$ is an undervoltage. Overshooting the deadband with an LTC tap can be represented with

$$\begin{aligned} v_2[0] &< v^- \text{ start with undervoltage} \\ v_1[0] + \bar{v}_L &> v^+. \end{aligned}$$

Combining the above two equations gives $v^{\text{diff}} > 2\varepsilon - \bar{v}_L$. These conditions for $v_2[0]$ being an *overvoltage* would yield the same $v^{\text{diff}} > 2\varepsilon - \bar{v}_L$. Now consider where our IC is not in W_o but at time T we land in W_o. Because the system has no internal memory states, oscillations will begin after this nonzero T as if the zero-start time was at T. □

Lemma 6. If $\boldsymbol{G} \prec 0$, system Σ_2 given by (5.9) has $v \to \pm\infty$.

Proof. Let eig($\boldsymbol{M}$) be a function that returns the set of all eigenvalues of matrix $\boldsymbol{M}$. Define a matrix $\boldsymbol{Q} = -\boldsymbol{G}$. Because $\boldsymbol{G} \prec 0$ and is diagonal, $\boldsymbol{Q}$ is diagonal and positive definite. The proof of Theorem 3.1 in [1] shows that $eig(\boldsymbol{X}\boldsymbol{S}) = eig(\boldsymbol{S}^{\frac{1}{2},\top}\boldsymbol{X}\boldsymbol{S}^{\frac{1}{2}}) \in (0, 2)$ for symmetric $\boldsymbol{X}$ and diagonal positive definite $\boldsymbol{S}$. Thus $eig(\boldsymbol{X}\boldsymbol{Q}) = eig(\boldsymbol{Q}^{\frac{1}{2},\top}\boldsymbol{X}\boldsymbol{Q}^{\frac{1}{2}}) \in (0, 2)$. Then $eig(I - \boldsymbol{X}\boldsymbol{G}) = eig(I + \boldsymbol{X}\boldsymbol{Q}) = 1 + eig(\boldsymbol{X}\boldsymbol{Q})$. With $eig(\boldsymbol{X}\boldsymbol{Q}) \in (0, 2)$, $eig(I - \boldsymbol{X}\boldsymbol{G}) > 1$. Thus the spectral radius of $(I - \boldsymbol{X}\boldsymbol{G})$ is greater than 1, so $e \to \infty$, and $v \to \infty$ or $v \to -\infty$. □

Lemma 7. The coupling effect of a single inverter actuating at node i on the voltage at node j is damped by a factor of η. That is, $\Delta v_j^{inv}(\boldsymbol{X}_{ij}, k+N, k, v_i[k]) = \eta \Delta v_i^{inv}(\boldsymbol{X}_{ii}, k+N, k, v_i[k])$.

Proof. From the update equations (5.14) and (5.15),

$$\begin{aligned} \Delta v_i^{inv}(\boldsymbol{X}_{ii}, k+1, k, v_i[k]) &= -\chi(v_i[k] - v^{ref}) \\ \Delta v_j^{inv}(\boldsymbol{X}_{ij}, k+1, k, v_i[k]) &= -\eta\chi(v_i[k] - v^{ref}) \\ &= \eta \Delta v_i^{inv}(\boldsymbol{X}_{ii}, k+1, k, v_i[k]) \end{aligned}$$

By Remark 4, the voltage change at each timestep over $[0\ N]$ is additive in the same direction. If we consider a duration over two timesteps,

$$\begin{aligned}\Delta v_j^{inv}(\boldsymbol{X}_{ij}, k+2, k, v_i[k]) =& v[k+2] - v[k+1] + v[k+1] - v[k] && (7.6)\\ =& \Delta v_j^{inv}(\chi, k+2, k+1, v_i[k+1]) + \Delta v_j^{inv}(\chi, k+1, k, v_i[k]) && (7.7)\\ =& -\eta\chi(v_i[k+1] - v^{ref}) - \eta\chi(v_i[k] - v^{ref}) && (7.8)\\ =& \eta\Delta v_i^{inv}(\boldsymbol{X}_{ii}, k+2, k, v_i[k])\end{aligned}$$

□

Lemma 10. If system Σ_3 with $g < 0$ has oscillations, v^{diff} increases after each oscillation period

Proof. We consider the case that the IC is below the deadband. We express the voltages after the first sequence of modes and compare $v^{\text{diff}}[k_0]$ to $v^{\text{diff}}[k_4]$

$$\begin{aligned}v_1[k_4] &= v_1[k_0] + \eta\Delta v_2^{inv}(k_0 + N_2, k_0, v_2[k_0]) + \bar{v}_L\\ &\quad + \Delta v_1^{inv}(k_0 + N_1, k_0, c) - \bar{v}_L\\ v_2[k_4] &= v_2[k_0] + \Delta v_2^{inv}(k_0 + N_2, k_0, v_2[k_0]) + \bar{v}_L\\ &\quad + \eta\Delta v_1^{inv}(k_0 + N_1, k_0, c) - \bar{v}_L\end{aligned}$$

where $c := v_1[k_0] + \eta\Delta v_1^{inv}(k_0 + N_2, k_0, v_2[k_0]) - \bar{v}_L$. Subtracting the above two equations, we have

$$\begin{aligned}v^{\text{diff}}[k_4] =& v^{\text{diff}}[k_0] + \eta\Delta v_2^{inv}(k_0 + N_2, k_0, v_2[k_0]) + \Delta v_1^{inv}(k_0 + N_1, k_0, c)\\ &- \Delta v_2^{inv}(k_0 + N_2, k_0, v_2[k_0]) - \eta\Delta v_1^{inv}(k_0 + N_1, k_0, c) - \bar{v}_L\end{aligned}$$

which simplifies to

$$v^{\text{diff}}[k_4] - v^{\text{diff}}[k_0] = (\eta - 1)(\Delta v_2^{inv}(v_2[0], N_2) - \Delta v_1^{inv}(k_0 + N_1, k_0, c)) \tag{7.9}$$

The damping factor has $0 < \eta < 1$, so $(\eta - 1)$ is negative. $v_2[k_0]$ is below the deadband, so $\Delta v_2^{inv}(N_2, v_2[k_0]) < 0$, and $v_1[k_2]$ is above the deadband, so $\Delta v_1^{inv}(c, N_1)$ is positive. Together, (7.9) is always positive. Thus $v^{\text{diff}}[k_4] > v^{\text{diff}}[k_0]$.

If we repeat this process for the case of the IC being an overvoltage, we get the same final equation (7.9). □